Real-Time In-Situ Investigations of [6]Phenacene Organic-Inorganic Structures with Organic Molecular Beam Deposition

Dissertation

der Mathematisch-Naturwissenschaftlichen Fakultät
der Eberhard Karls Universität Tübingen
zur Erlangung des Grades eines
Doktors der Naturwissenschaften
(Dr. rer. nat.)

vorgelegt von
Matthias Zwadlo
aus Heydebreck/Polen

Tübingen
2023

Gedruckt mit Genehmigung der Mathematisch-Naturwissenschaftlichen Fakultät der Eberhard Karls Universität Tübingen.

Tag der mündlichen Qualifikation:	08.02.2024
Dekan:	Prof. Dr. Thilo Stehle
1. Berichterstatter:	Prof. Dr. Dr. h.c. Frank Schreiber
2. Berichterstatterin:	Jun.-Prof. Dr. Jannika Lauth

Abstract

Organic semiconductors (OSCs) that consist of fused benzene rings are promising candidates for high-performance electronic devices like organic light-emitting diodes (OLEDs), organic field-effect transistors (OFETs) and organic photovoltaics (OPV). Compared to their inorganic counterparts, OSCs have a different charge transfer mechanism that depends on the highest occupied molecular orbital (HOMO) and lowest unoccupied molecular orbital (LUMO). OSCs offer mechanical flexibility, stretchability as well as optical transparency and are low-cost alternatives for their inorganic counterpart that are suitable for mass production. A vast amount of different OSCs are available, which are under constant development and research. Especially the study of growth, structure and molecular packing is important due to its influence on the electronic properties of prepared devices. Devices made of OSCs consist of several layers where multiple materials are combined into a complex organic-inorganic interface or so-called hybrid system. Two parts of this interface were under investigation in this work. Alkali metal doped layers are used to manipulate the electronic properties of the original material and gold-organic interfaces that are used for electrical contacting. Both methods can lead to changes in the growth, structure and morphology of the original material and were therefore investigated in this thesis. This was achieved by utilizing preliminary work in the home laboratory as well as real-time in-situ measurements performed at state-of-the-art synchrotrons. Thin films were characterized by using various X-ray scattering methods combined with optical methods. The evaluation was done by examining the in-plane and out-of-plane structure during growth and calculating the unit cell structure, orientation and molecular packing. The molecule used for this study was [6]Phenacene deposited as a thin film by using organic molecular beam deposition (OMBD) under ultra-high vacuum (UHV) conditions. These results were also compared to other phenacenes. [6]Phenacene shows a Stranski-Krastanov growth behaviour which leads to wedding cake islands with a well-defined transition between the terraces. The unit cell parameters and molecular packing was calculated by assuming four molecules inside a unit cell. The molecular stacking is influenced by the parity of used molecules, which depends on the number of benzene rings of the used phenacene. Organic-inorganic interfaces of [6]Phenacene were investigated by using the alkali metals: potassium, rubidium and caesium. They were either deposited on top of a [6]Phenacene thin film or co-evaporated during growth leading to various changes in crys-

tallinity and intercalation into the thin film. Co-evaporation with caesium leads to a phase separation while potassium and rubidium atoms intercalate into the [6]Phenacene unit cell. This changes the [6]Phenacene unit cell structure and molecular packing and, therefore, also has an impact on the (opto)electronic properties of the prepared thin films. Further experiments with gold as a common contacting material were performed by depositing the metal on top of [6]Phenacene thin films. It was found that gold is mainly filling the space between the terraces of the wedding cake structure and, therefore, the [6]Phenacene crystal structure stays intact. The results of this thesis showed various changes in structure and morphology for organic-inorganic systems which can lead to a further understanding of growth processes in thin films. This is especially important for the further development of OSCs.

Zusammenfassung in deutscher Sprache

Organische Halbleiter bestehen aus verbundenen Benzolringen und sind vielversprechende Kandidaten für Hochleistungselektronik, beispielsweise organische Leuchtdioden, Feldeffekttransistoren und Fotovoltaik. Verglichen mit ihren anorganischen Gegenstücken haben organische Halbleiter einen anderen Mechanismus des Ladungstransfers, der vom höchsten besetzten molekularen Orbital (HOMO) und niedrigsten unbesetzten molekularen Orbital (LUMO) abhängt. Organische Halbleiter bieten mechanische Flexibilität, Dehnbarkeit, optische Transparenz und sind billige Alternativen zu anorganischen Halbleitern mit der Möglichkeit zur Massenproduktion. Eine große Menge an organischen Halbleitern ist verfügbar, welche nach wie vor Gegenstand konstanter Forschung und Entwicklung sind. Vor allem die Untersuchung von Wachstum, Struktur und der molekularen Packung sind aufgrund ihres Einflusses auf die elektronischen Eigenschaften von Geräten wichtig. Geräte aus organischen Halbleitern bestehen aus mehreren Schichten mit unterschiedlich kombinierten Materialien. Diese formen ein komplexes organisches-anorganisches System, welches auch hybrides System genannt wird. Zwei Teile dieses Systems wurden untersucht. Dünne Filme, die mit Alkalimetallen dotiert wurden, um die elektronischen Eigenschaften des Grundmaterials zu verändern, sowie Gold-organische Schichten, welche für elektrische Kontakte benutzt werden. Beide Methoden können benutzt werden, um Änderungen in Wachstum, Struktur und der Morphologie des Grundmaterials hervorzurufen und wurden deshalb in dieser Arbeit untersucht. Diese Ziele wurden mithilfe von Vorarbeit im Heimatlabor sowie Echtzeitmessungen, die in Synchrotrons der neusten Generation stattgefunden haben, bewerkstelligt. Dünne Filme wurden mittels verschiedener Methoden der Röntgenstreuung sowie optischen Methoden untersucht. Die Auswertung bestand aus der Untersuchung der in-plane und out-of-plane Struktur während des Wachstums, mit der die Einheitszelle, Orientierung und molekulare Packung berechnet werden konnten. Das benutzte Molekül dieser Arbeit war [6]Phenacen, welches als dünner Film mittels organischer Molekularstrahldeposition (OMBD) im Ultrahochvakuum (UHV) gewachsen wurde. Die Ergebnisse wurden auch mit anderen Phenacenen verglichen. [6]Phenacen zeigt ein Stranski-Krastanov Wachstumsverhalten, welches zu "wedding cake" ähnlichen Inseln mit einem wohldefinierten Übergang zwischen den Lagen führt. Die Einheitszelle, Orientierung und molekulare Packung wurde mithilfe von vier Molekülen in der Einheitszelle berechnet. Das molekulare Stapelverhalten zeigt eine Abhängigkeit zur

Parität der Anzahl der Benzolringe des verwendeten Phenacens. Organisch-anorganische Grenzflächen von [6]Phenacen wurden mittels der Alkalimetalle, Kalium, Rubidium und Cäsium untersucht. Sie wurden entweder oben auf einen [6]Phenacen Dünnschichtfilm oder gleichzeitig zusammen mit diesem aufgedampft, was zu unterschiedlichen Ergebnissen in Bezug auf Kristallinität und Eindringen in den Dünnschichtfilm führte. Gleichzeitige Aufdampfung mit Cäsium führt zu einer Phasenseparierung, während Kalium und Rubidium in die Einheitszelle von [6]Phenacen eindringen. Das führt zu Änderungen der [6]Phenacen Einheitszelle und Orientierung und hat damit auch eine Auswirkung auf die optischen Eigenschaften von präparierten dünnen Filmen. Weitere Versuche mit Gold als Kontaktiermaterial wurden durchgeführt, indem Gold oben auf dünne Filme von [6]Phenacen aufgedampft wurde. Im Prinzip füllt Gold den Raum zwischen den "wedding cakes", darum bleibt die [6]Phenacen-Kristallstruktur darunter intakt. Die Ergebnisse dieser Arbeit zeigten verschiedene Änderungen der Struktur und Morphologie von organisch-anorganischen Systemen, die zu einem weiteren Verständnis der Wachstumsprozesse in dünnen Filmen führen könnte. Dies ist wichtig für die weitere physikalische Betrachtung von Anwendungen aus organischen Halbleitern.

Contents

Part I.

Introduction and theory

1. Motivation

Modern technology depends on complex hybrid materials with non-trivial morphologies that offer a wide range of applications. Especially organic molecules that consist of fused benzene rings are an attractive alternative to their already established inorganic counterparts. They have gained much attention in the last decade due to their wide range of applications for optoelectronic devices. By offering highly desirable properties such as mechanical flexibility, stretchability [1–3], as well as optical transparency [2, 4], they offer a low-cost alternative for mass production [5–8]. Unfortunately, organic devices have lower efficiencies and lifetimes compared to their inorganic counterparts. The most popular devices are organic photovoltaic cells (OPV) that can be used for the generation of electricity [9–13] and organic light-emitting diodes (OLED) for light generation, starting from single diodes [14, 15], up to an array of diodes for displays [16–19]. Another important application are organic field-effect transistors (OFETs) [20–23] that can be used in multiple devices. An interesting application that is based on OFETS, are chemical detectors [24, 25]. Organic molecular thin films for devices can be spin-coated, dip-coated, inkjet printed or deposited with organic molecular beam deposition (OMBD). OMBD is a more expensive alternative that can grow organic thin films with purer and well-ordered structures in ultra-high vacuum (UHV). This method also offers better control over growth parameters like substrate temperature, thin film thickness and deposition rate that are important for the final thin film morphology [26–28]. However, organic devices not only consist of organic molecules. Similar to inorganic semiconductors, they consist of several layers where pure or mixtures of several organic [29] or inorganic [30] materials can be used, leading to a complex stack of organic-inorganic hybrid interfaces (Fig. 1.1). This hybrid interface can alter the morphology, and electronic properties or even exhibit new effects like superconductivity [31, 32] of the material.

A fundamental mechanism that is used to change the electronic properties of these materials is doping. Before it was used in organics, it was a very common method in their inorganic counterparts, which lead to the development of various inorganic semiconductor devices with different characteristics. By integrating small amounts of impurity atoms in a crystalline semiconductor, its structure is altered, leading to several defects. These defects lead to a shift in the Fermi level that is important for the band transport structure. The result is a change of the energy alignment relative to the metal contact or other differently

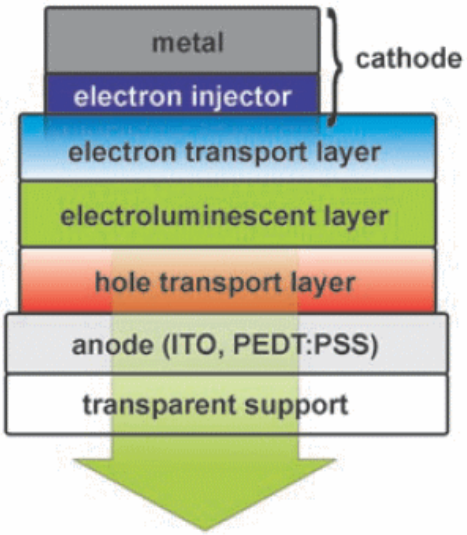

Figure 1.1.: Schematic representation of a multilayer OLED. Taken from Ref. [33].

doped organic semiconductors. However, the energy-intensive production of inorganic semiconductors makes them less favourable for low-cost and large-area applications. Therefore, doping of their organic counterparts has gained large popularity in the last decade. The doping of organic thin films uses similar materials compared to inorganics, but the theoretical description is rather different due to the different transport mechanisms of OCSs that exhibit hopping instead of band transport. In the end, the conductivity of a doped layer can be modified by using p- or n-type doping materials that are intercalated in an active layer. By combining this layer with other materials or different layer sequences, a higher degree of freedom is reached while controlling the position of the Fermi level [34, 35]. Also, other important effects have been reported like changes in the charge transfer exciton recombination by a p-type dopant. The infused dopant leads to reduced recombination and therefore the charge separation improves, which is important for organic photovoltaics [36]. Doping can also alter the structure of organics leading to the discovery of new polymorphs [37]. Several types of methods and approaches have been found to apply a dopant to a semiconducting material [38]. The use of oxidising gases [39], vapours of alkyl silanes [40] or even diffusion of highly reactive alkali metals like lithium into a material [41] was performed. Recently, the intercalation through the diffusion from the surface of the potassium that was deposited on top of pentacene thin film was observed [42], and further new doping methods are under investigation [43]. In terms of stability and reproducibility, it was found that co-evaporation of the organic molecules together with the dopant material offers the most favourable results [44]. The precise doping mechanisms are still under investigation by a large scientific community [45] and a greater understanding of it will help to design more efficient devices in the future.

Another important part of an OSC device is the contacting material, which is mainly realized by metals. The proper function of this contact between the metal and organic layer is important for high-performance devices. Especially binding and energy level alignment of organics on metals is under steady research due to the complex interplay between weak physisorption and strong chemisorption [46]. To apply a contacting material onto a thin film, several methods are available that range from direct evaporation, which is similar to OMBD, up to printing techniques [47]. It is important to consider that the electrical properties are strongly influenced by the structure of the prepared layer and the preparation conditions have a huge impact on the resulting interface [48]. Several publications found polymorphs or other noticeable changes in the structure of the organic material when deposited on common contacting materials like silver [49, 50] and gold [51–53]. The most interesting effects are structural changes that happen when the organic material is deposited onto a metal, rather than a silicon substrate. Organic molecules can change from a standing-up to a lying-down phase, which changes the structure completely [54]. But also, the direct interface between the metal and organic layer can change from an abrupt to a diffuse interface (see Fig. 1.2) when the deposition is reversed [55].

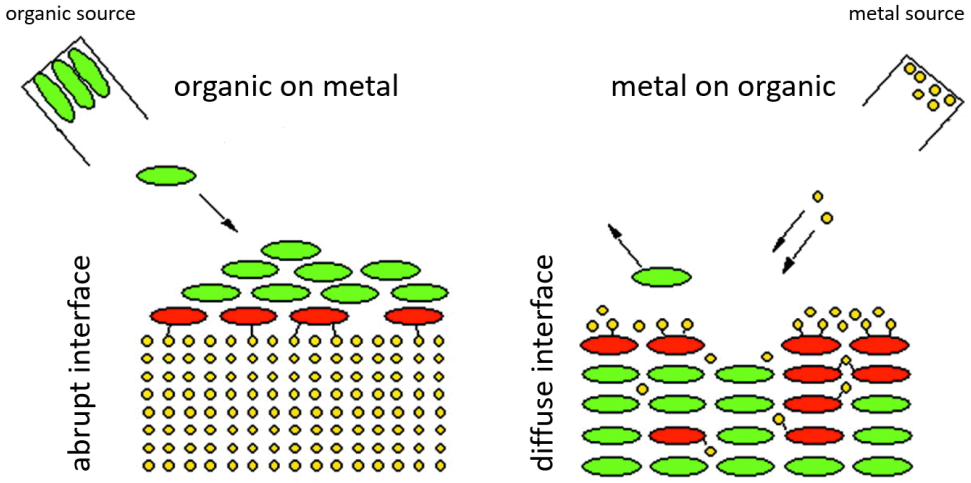

Figure 1.2.: Interface changes depending on deposition order. Organic-on-metal deposition leads to an abrupt interface while metal-on-organic deposition results in a diffuse interface. Taken and modified from Ref. [55].

This thesis aims to get a better understanding of the growth and morphology of organic-inorganic interfaces due to their influence on optical and electronic properties [56, 57]. Usually, data from various techniques and different samples are compared, but due to many possibilities regarding growth and temperature conditions it is very unlikely to produce identical samples. Also, measuring a film with different methods takes at least multiple days, therefore also post-growth effects have to be taken into account. Both effects inhibit a complete understanding of growth. To approach this problem, real-time in-situ methods

have to be used, where the film is ideally measured during the growth process [58, 59]. To obtain a high time resolution and image quality, synchrotron-based X-ray sources with a high photon flux as well as modern area detectors with a high resolution and frame rate were used.

The next chapter will describe the fundamental concepts and the growth of organic semiconductors. The third and fourth chapter describe the materials and experimental techniques that were used in this work. The results are discussed in chapter five to seven, which begins with pure organic thin films and then continues with two different inorganic materials that have been used for organic-inorganic experiments. The last chapters consist of a summary and outlook as well as several appendixes.

2. Fundamental concepts

The first part of this chapter will give a brief introduction to the fundamental concepts of organic semiconductors and thin film growth. These contents are inspired by the books of Sze [60], Klauk [61], Schwörer [62] and Jung [63] to which is referred for a deeper introduction. The second part will give a brief introduction to X-ray scattering and is inspired by the books of Tolan [64] as well as McMorrow and Als-Nielsen [65].

2.1. Semiconductor technology

Semiconductors are an important material for microelectronic devices. A short introduction to their working principle as well as their usage in devices will be provided in this section.

Electrons inside a periodic crystal lattice can be described by solving the Schrödinger equation for this case. The resulting waves are called Bloch waves and the existence of several energy bands in a crystal lattice can be found. This band theory can be used to describe the properties of metals, insulators and semiconductors. Figure 2.1 shows the energy diagram of these results.

The red dashed Fermi level is the highest possible energy of a particle in the ground state of the system (at $T = 0$ K) and can be used for the definition of metals, insulators and semiconductors. The highest occupied band is called the valence band while the lowest unoccupied band is called the conduction band. The distance between those bands is called the band gap. Metals have one energy band that is not completely filled. This leads to a continuous charge transfer into different energy states. Therefore, metals are conductors. Insulators and semiconductors have a huge band gap between the conduction and valence band, leading to a high specific resistance and therefore nearly zero conductivity. Semiconductors are materials that are insulators at very low temperatures. However, at room temperature, semiconductors can have a respectable conductivity due to thermal energy. This conductivity of intrinsic semiconductors can be further increased by the insertion of foreign atoms. This process is called doping and leads to an impurity state in the energy band gap either to an additional energy level near the valence band (n-type doping) or the conduction band (p-type doping). The result is a narrower band gap, reducing the required energy for transferring electrons into unoccupied states and therefore making charge trans-

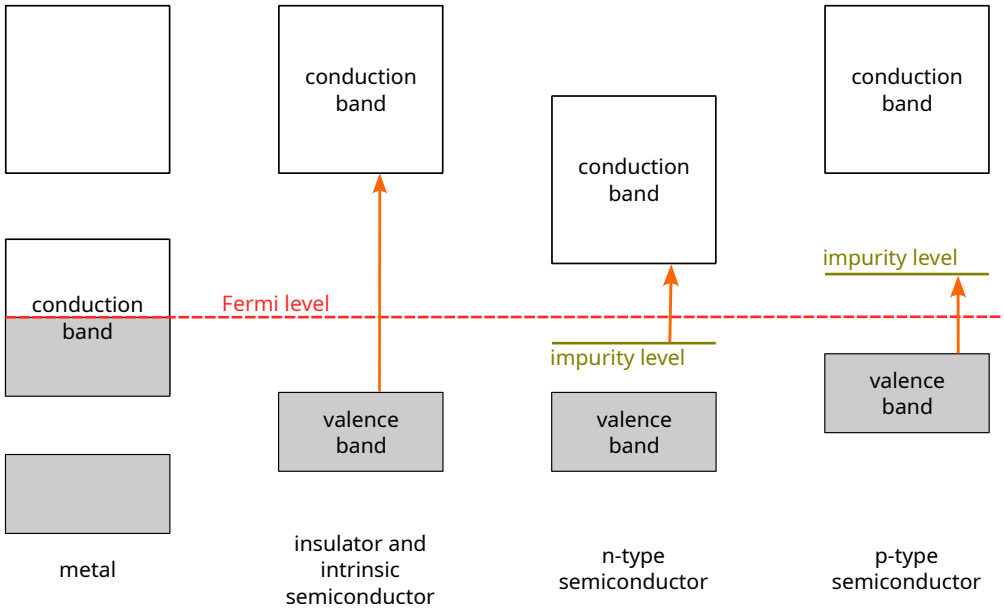

Figure 2.1.: Energy diagram overview of metals, isolators and semiconductors. Redrawn and modified from Ref. [61].

fer processes possible. This type of semiconductor is then called an extrinsic or p/n-doped semiconductor.

The properties of semiconductors have led them to be a dominant material in microelectronics. A fundamental mechanism is the pn-junction, which is used in diodes. By combining a p- and n-semiconductor with an abrupt transition, the electric behaviour leads either to passage or blocking of the current, depending on the current direction. If a positive voltage is applied on the positive part of the junction, flow through the diode is enabled. However, when a negative voltage is applied on the positive side, an exclusion zone is formed, leading to an inhibited current flow. An example of this behaviour is shown in Figure 2.2.

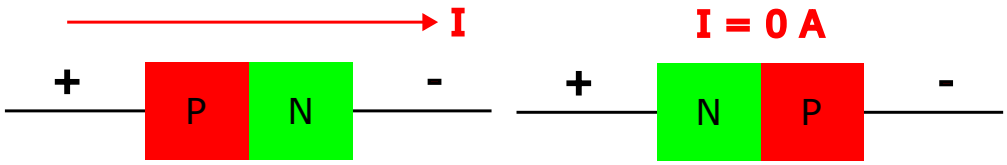

Figure 2.2.: Working principle of a diode (pn-junction). When a positive voltage is applied to the p-semiconductor, the electrical current can pass the device. Vice versa the current flow is blocked.

Further development of this technique are transistors and field-effect transistors that allow control of the current flow by another small control current. Semiconductor technology has also led to various photonic devices that can be roughly divided by the mechanism of converting photons into electric energy or vice versa. Electric energy can be converted into optical radiation, a mechanism that is exploited by light-emitting diodes (LEDs) or semicon-

ductor lasers. But also the conversion of electromagnetic radiation into electric energy can be utilized either for the detection of photons (photo-detection) or energy harvesting (solar cells).

2.2. Organic semiconductors

Organic semiconductors (OSCs) are materials that offer similar properties than their inorganic counterparts and can be used in devices like organic light-emitting diodes (OLEDs), organic solar cells or organic field-effect transistors (OFETs). However, there are huge differences regarding material and optical properties between those groups, that lead to a completely different mechanism of charge transfer. OSCs can be divided into polymers and small molecules, the latter of which were used in this work. Small molecules have a length of a few nanometers while polymers can have lengths of over 100 nanometers. Semiconducting organic molecules are constructed mainly from hydrogen (H) and carbon (C) but also small amounts of nitrogen (N), oxygen (O) and further atoms can be present. To describe the molecular and electronic structure of OSCs, the organic molecule Benzene (C_6H_6) is considered. Carbon has four valence electrons that are distributed in one 2s and three 2p orbitals which makes it possible to establish four bonds with neighbouring atoms. In this simplified scheme, it is energetically favourable to share electrons between the orbitals of neighbouring atoms and therefore a bond between the orbitals, the so-called covalent bond, is formed. In the exemplary case of Benzene, linear combinations of one 2s and two 2p orbitals are formed, creating a total of three hybrid orbitals (sp^2-hybridization). One carbon atom is connected to two neighbouring carbon atoms and one hydrogen atom through σ-bonds, forming a benzene ring. The fourth valence electron is delocalized through the upper and lower orbital ring plane forming a π-bond (see. Figure 2.3).

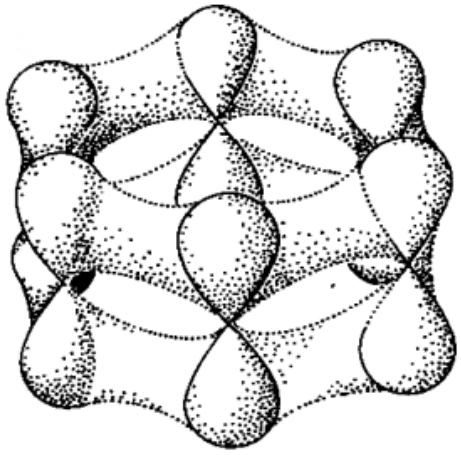

Figure 2.3.: π-bond of a benzene ring. Taken and modified from Ref. [62].

This leads to a structure with cyclic conjugated double bonds between the carbon atoms and is also called an aromatic molecule. σ-bonds are stronger than π-bonds which leads to an electronic structure that mainly uses the delocalization of π-electrons. The π orbital with the highest energy is called the highest occupied molecular orbital (HOMO) while the one with the lowest energy is called the lowest unoccupied molecular orbital (LUMO). The energy difference between those gives rise to a band gap similar to inorganic semiconductors. However, the band gap is usually bigger and the charge transfer process is quite different compared to the inorganic band structure behaviour shown in Figure 2.1. Usually, OSCs are insulators and can become conducting when injected with charge carriers. This can be done by doping with donor/acceptor molecules, high voltage or irradiation. OSCs show either a p-type (hole transporting) or n-type (electron transporting) behaviour depending on the used material. P-type/n-type organic materials are also called donors/acceptors. A HOMO which is close to the Fermi level of the contacting material can be injected with holes by using a negative voltage, which leads to electron transport from the OSC into the metal (p-type). Similar to this, when a LUMO is close to the Fermi level, it can be injected with electrons by using a positive voltage, leading to electron transport into the OSC (n-type). For a better understanding, this process is depicted in Figure 2.4.

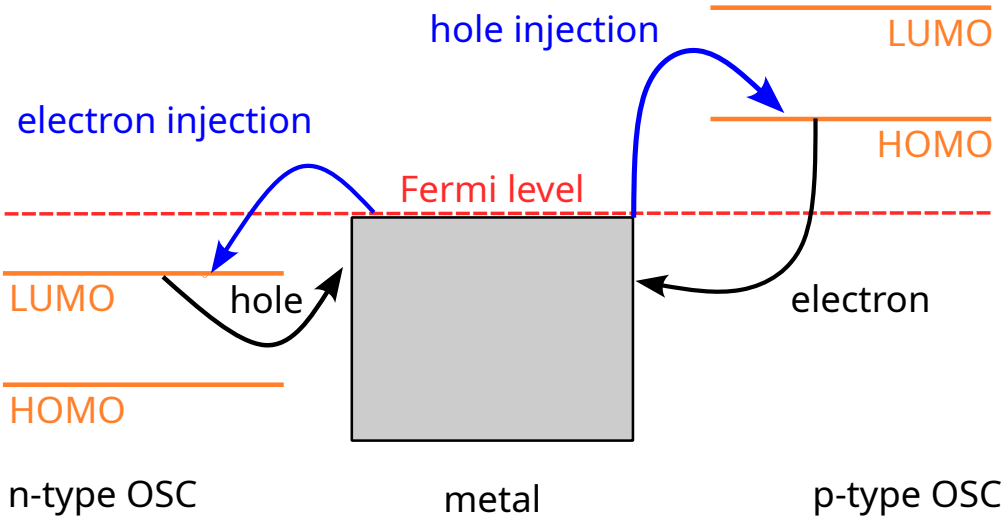

Figure 2.4.: Schematic of an organic semiconductor (OSC) close to a metal electrode. The semiconducting behaviour is defined by the HOMO/LUMO positions relative to the Fermi level of the metal: n-type OSCs are electron transporting while p-type OSCs are hole transporting.

2.3. Interaction forces

The interaction forces between molecules have a huge impact on the resulting thin film by modifying the growth behaviour and therefore its resulting structure and morphology. It is found that the interactions between organic/organic and organic/inorganic interfaces depend mainly on van-der-Waals forces [66]. Compared to other bonds, like the covalent bonds or ionic bonds, van-der-Waals forces are weak and short-ranged. Different types of van-der-Waals forces can be divided by the type of molecule. The London dispersion forces act between electrically neutral and non-polar molecules, Keesom-interactions happen between two dipoles and the Debye forces act between a dipole and a polarized molecule. In the case of organic molecules, the forces act mostly between non-polar molecules. Therefore by using the London dispersion force, the interaction energy for a pair of molecules can be written as

$$V_{\text{attract}}(r) = -\frac{A}{r^6}, \tag{2.1}$$

with the distance r and the Hamaker constant A, that includes compound dependent properties [67]. While the London dispersion force is responsible for an attraction between molecules, the counterpart is the Coulomb repulsion. The repulsive force originates in the Pauli principle, where additional electrons are excluded from fully occupied orbitals. This force is also short-ranged but has a much higher strength with decreasing distance. The superposition of both forces is generally handled by using the approximation

$$V = 0 \text{ for } r > r_0 \text{ and } V = \infty \text{ for } r \leq r_0, \tag{2.2}$$

which can be combined with Equation 2.1 to the sum of repulsion and attraction

$$V(r) = \frac{B}{r^{12}} - \frac{A}{r^6}. \tag{2.3}$$

This equation is called Lennard-Jones potential with another constant B and is visualised in Figure 2.5.

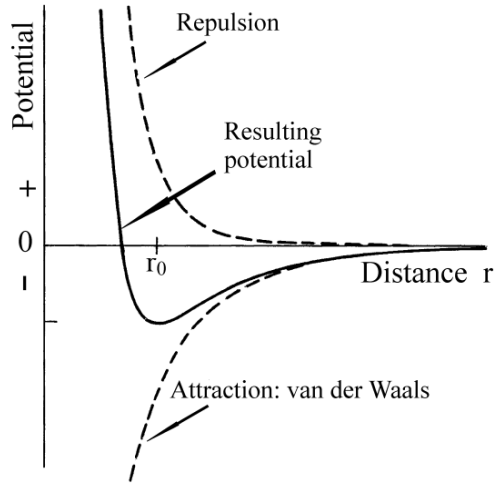

Figure 2.5.: Combination of repulsive and attractive forces. The equilibrium distance is at r_0. Taken from Ref. [62].

2.4. Growth of thin films

The growth of organic thin films is a process depending on several thermodynamic interactions happening when molecules are deposited onto a substrate. A deeper introduction can be found in the book from Pimpinelly [68] and in the articles of Venables [69] and Forrest [26].

By heating up molecules in an effusion cell, a flux F of molecules is created towards the substrate surface. Molecules which condensate on the surface can undergo several processes including surface diffusion, nucleation, interlayer transport or even re-evaporation off the surface [70]. Figure 2.6 shows an overview of the processes that are involved during thin film growth on the substrate surface.

The two major parameters that can influence the resulting crystal growth are the temperature of the effusion cell that alters the molecular flux as well as the substrate temperature which is important for the processes on the surface. Low flux and high substrate temperature, for example, can lead to better crystal quality because the molecules have more energy to get ordered on the substrate. Other parameters like binding energies and molecule sizes are also important factors to consider, due to the impact on other processes [27]. It also has to be mentioned that growth does not stop when the molecular flux is halted. Growth is a non-equilibrium process that includes surface diffusion, nucleation or interlayer transport that continues and can lead to drastic changes in the film structure. Therefore, it is important to apply in-situ methods, so post-growth changes can be directly observed [59].

In general, three different growth modes can be described by considering the surface free energies of the film γ_F and substrate γ_S as well as the interfacial free energy γ^* which describes the energy between the substrate and the film. For molecules that are strongly

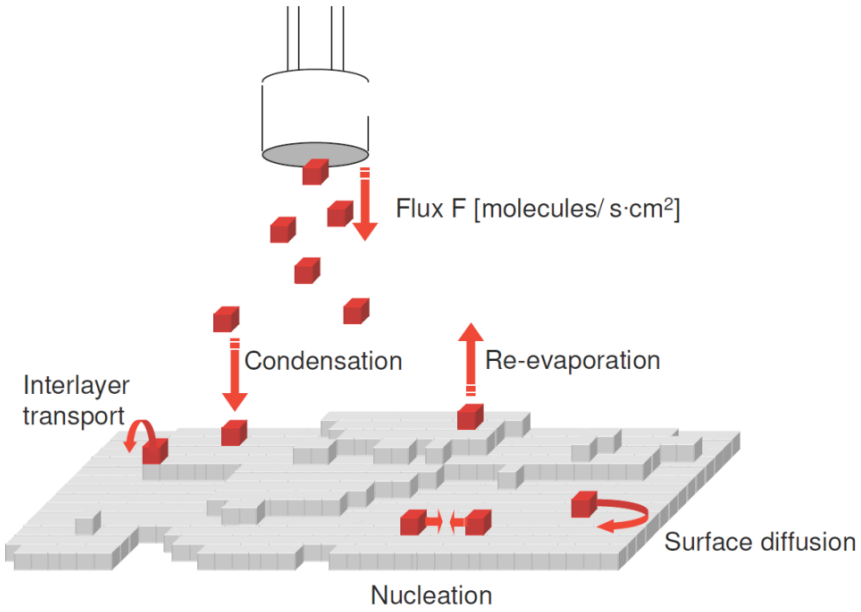

Figure 2.6.: Overview of processes involved during thin film growth. Taken and modified from Ref. [71].

bound to each other ($\gamma_F + \gamma^* > \gamma_S$) the molecules are nucleating directly into islands. This growth mode is called Vollmer-Weber (VW) or island growth. If the molecules are bound more strongly to the substrate ($\gamma_F + \gamma^* < \gamma_S$), layers are formed. After one layer is completed, another layer is formed on top. This growth mode is called Frank-van der Merwe or layer-by-layer growth. A third growth mode is dependent on a specific critical film thickness and the respective molecule. The deposition starts with layer-by-layer growth but after one or more monolayers the growth mode changes into island growth. This growth mode is called Stranski-Krastanov (SK) or layer-plus-island growth. A summary of all growth modes can be seen in Figure 2.7.

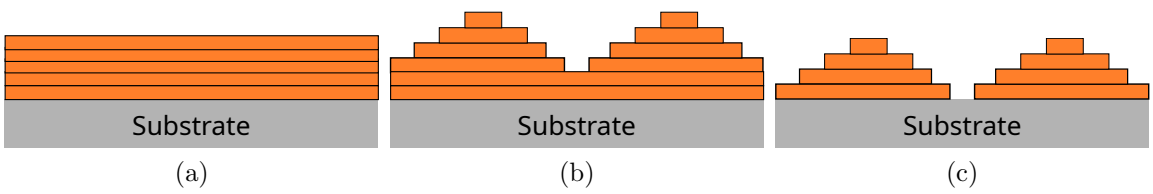

Figure 2.7.: Overview of characteristic crystal growth modes: a) layer-by-layer growth (Frank-van der Merwe), b) layer plus island growth (Stranski-Krastanov) and c) island growth (Vollmer-Weber).

2.5. Mixtures and heterostructures

In this thesis, small organic molecules were mixed with alkali metals and gold. Mixtures of organic-inorganic compounds can lead to further intermolecular interactions which can be different than in pure organic thin films, this chapter describes the organic-organic binary mixture to get an understanding of the basic mechanisms. By mixing two different kinds of organic molecules, one of the first questions that arise is if the materials are mixing or phase separating. A simple model to describe this process was developed by Kitaigorodsky, which uses two kinds of particles (A and B) and considers just the interaction between two direct neighbours [72]. By mixing two different particles with different concentrations (x_A and x_B), the free energy changes and can be written as

$$\Delta F_{\text{mix}} = k_B T[(x_A \ln(x_A) + x_B \ln(x_B)) + \chi x_A x_B], \tag{2.4}$$

with the Boltzmann constant k_B and the temperature T. The parameter χ describes the interparticle interaction and can be written as

$$\chi = \frac{Z}{k_B T}(W_{AA} + W_{BB} - 2W_{AB}). \tag{2.5}$$

Here Z is defined as the coordination number and W_{AA}, W_{BB} and W_{AB} are the interaction energies between particles A and B. By variating these energies, three scenarios can happen which result in a different mixing behaviour.
$\chi < 0.5$: The interparticle energy between two different particles (W_{AB}) is higher than between particles of the same species (W_{AA} and W_{BB}). In this situation, it is favourable for particle A to have particle B as a neighbour. Therefore this system favours intermixing which is shown in Figure 2.8a.
$\chi > 2$: The interparticle energy between two same particles (W_{AA} or W_{BB}) is higher than between different ones (W_{AB}). This makes the mixing of the two species unfavourable, leading to a phase separation which is shown in Figure 2.8b.
$\chi \approx 0$: When the interparticle energies of both compounds are similar to each other, neither scenario is preferred. The mixing is therefore determined by the entropy, leading to a statistical mixing which is shown in Figure 2.8c. This also occurs when the temperature is high enough, leading to a domination of the entropy in the system.

These mixtures are also called heterostructures, which can be further described by examining the interface between molecules A and B. Figure 2.9 shows an overview of all possibilities. A bulk heterojunction (BHJ) is formed by intermixing, leading to a homogeneously mixed material. If two molecules phase-separate, a planar heterojunction (PHJ) is formed, having a sharp edge between these two materials. A mixture of both scenarios is the graded interface, where both materials intermix in the contact zone and phase separate in the outer regions.

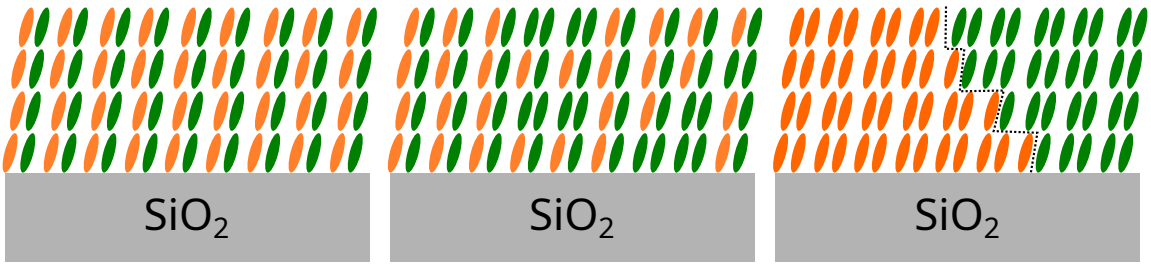

(a) (b) (c)

Figure 2.8.: Mixing of organic molecules leads to different scenarios depending on the interaction energies between the particles: a) intermixing, b) statistical mixing and c) phase separation.

(a) (b) (c)

Figure 2.9.: Overview of heterostructures: a) bulk heterojunction (BHJ), b) planar heterojunction (PHJ) and c) graded interface.

2.6. X-ray scattering

This section will give a short introduction to the theory of X-ray scattering. A more practical approach which covers the usage of X-ray methods is given in section 4.4. In general, the interaction of X-ray photons with matter is based on electron movement which is caused by the electrical component of an electromagnetic wave. This leads to the following processes:

- Classical scattering
- Photoelectric absorption
- Compton scattering

Classical scattering is an elastic process, where the energy of the scattered photon is the same as the incoming photon. This process is the main process that is exploited when the material structure is investigated with X-rays. However, also the inelastic processes that change the energy of the scattering wave have to be taken into account (Compton scattering and photoelectric absorption) due to the impact as a background in scattering experiments. The probability for a scattering process is called the differential scattering cross-section ($\frac{d\sigma}{d\Omega}$) given by

$$\frac{d\sigma}{d\Omega} = \frac{I_{\text{scattered}}}{\Phi \Delta\Omega}, \tag{2.6}$$

where $I_{\text{scattered}}$ refers to the number of photons per second measured by a detector, Φ is the incident photon flux and $\Delta\Omega$ describes the solid angle of the detector. By integrating all possible angles, the total scattering cross-section σ can be defined as

$$\sigma = \int_{4\pi} \left(\frac{d\sigma}{d\Omega} \right) d\Omega. \tag{2.7}$$

Due to scattering and absorption, the X-ray beam is attenuated when travelling through a material, hence the intensity decreases as

$$I = I_0 e^{-\mu x}. \tag{2.8}$$

This equation is also called Beers law and it describes the intensity reduction from I_0 to I after travelling through a material with thickness x. μ is called the absorption coefficient, defined as

$$\mu = \sigma_{\text{all}} \rho_{\text{at}} = \frac{\rho_m N_A}{M} \sigma_{\text{all}} \tag{2.9}$$

Here ρ_{at} is the numeric density of atoms, σ_m the mass density, N_A the Avogadro number and M the molar mass. σ is the total atomic scattering cross section that consists of several contributions from the different processes, given by

$$\sigma_{\text{all}} = \sigma_{\text{classical}} + \sigma_{\text{absorption}} + \sigma_{\text{compton}}. \tag{2.10}$$

To inspect the reflection and transmission of an X-ray beam on thin films, a simple interface between two media with the refractive indices $n_{1,2}$ and the wave vectors $\vec{k}_{0,1,2}$ is considered, which is shown in Figure 2.10a.

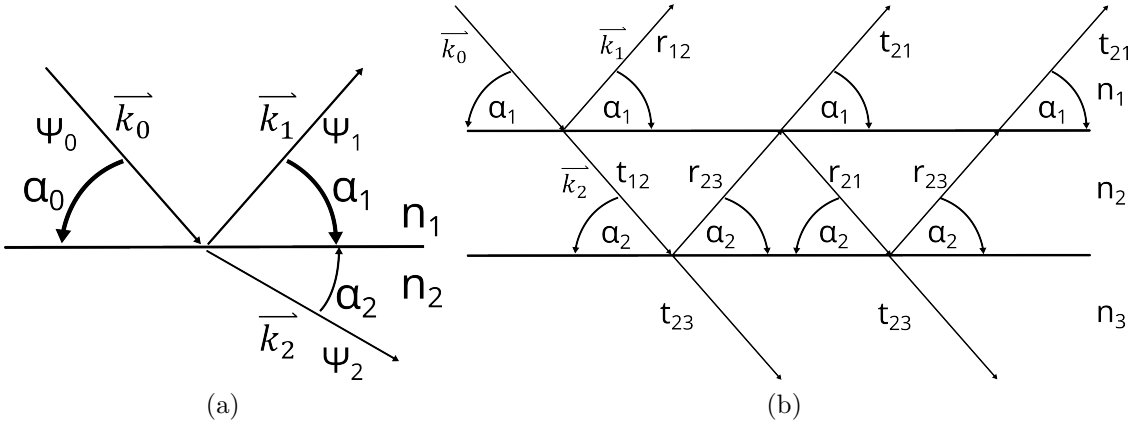

Figure 2.10.: Scattering at interfaces: a) one interface and b) two interfaces.

In optics, the incidence angle equals the reflection angle ($\alpha_0 = \alpha_1$). The refraction angle α_2 can be determined from Snell´s law

$$\frac{\cos\alpha_1}{\cos\alpha_2} = \frac{n_2}{n_1} = \frac{v_1}{v_2}, \tag{2.11}$$

where $n_{1,2} = \frac{c}{v_{1,2}}$ are corresponding refraction indices of the media that are determined by the phase velocity of the light $v_{1,2}$ in these media. The refractive index is $n = 1$ for vacuum and reaches values of $n > 1$ for visible light in different materials leading to a decrease of the outgoing angle α_2. However, this does not apply to X-rays where the refractive index has values of $n < 1$ which leads to the opposite effect and is shown in Figure 2.10a. The refractive index for X-rays is given by

$$n = 1 - \frac{2\pi\rho_{\text{at}} r_e f(0)}{k^2} = 1 - \delta + i\beta, \tag{2.12}$$

with the atomic density ρ_{at} and the scattering amplitude of an atom $r_e f(0)$. This equation can be written with a real (δ) and imaginary part ($i\beta$). When the incident wave propagates from vacuum/air to a material with a smaller refractive index below a critical angle $\alpha_0 \leq \alpha_c$, total external reflection can be observed, which is a very typical case for X-rays. This effect

also appears in optics in the opposite case when the wave is moving to a medium with a lower density. By applying several approximations, the critical angle can be written as

$$\alpha_c = \sqrt{2\delta} = \sqrt{\frac{r_0 \lambda^2}{\pi} N_A \frac{z + f'}{A} \rho} \tag{2.13}$$

to relate it to the film density [73]. Here $r_0 = 2.82 \cdot 10^{-5}$ Å is the classical radius of the electron, λ the X-ray wavelength, z the atomic number of an atom, A the atomic mass, f' the dispersion correction to the atomic scattering factor and ρ the mass density. On the X-ray reflectivity (XRR) curve, the total external reflection leads to a plateau for $\alpha < \alpha_c$ where all incident intensity is reflected. Equation 2.13 also shows that the critical angle increases with the density of the film.

The transmission t and reflection r index coefficients of an ideal interface can be described by using a wave function $\psi_{0,1,2}$ for the incoming, reflected and transmitted wave. The results can be represented with the Fresnel equations

$$r = \frac{\psi_1}{\psi_0} = \frac{n_1 \sin\alpha_1 - n_2 \sin\alpha_2}{n_1 \sin\alpha_1 + n_2 \sin\alpha_2}, \tag{2.14}$$

$$t = \frac{\psi_2}{\psi_0} = \frac{2n_1 \sin\alpha_1}{n_1 \sin\alpha_1 + n_2 \sin\alpha_2}. \tag{2.15}$$

For multilayer thin films, the Fresnel equations can be applied to calculate the reflectivity. An example which consists of air (n_1), thin film (n_2) and substrate (n_3) and therefore two interfaces where scattering occurs, is shown in Figure 2.10b. The first transition (air to thin film) is from refractive index n_1 to n_2 and therefore the index 12 is used. The first number stands for the origin of the wave and the second number for the destination of the wave. At the first interface 12 between the air (n_1) and the film (n_2), part of the intensity is reflected from the interface (r_{12}) and the rest of the intensity is transmitted into the bulk of the film (t_{12}). The transmitted part is then partially reflected from the lower interface (r_{23}) or penetrates into the substrate (t_{23}). The reflected wave is further reflected between the two interfaces (r_{21}) and (r_{23}) and at each reflection a portion of its intensity is transmitted to the air (t_{21}) or substrate (t_{23}). The total reflection coefficient of this system of two interfaces can be calculated as a ratio $r_{slab} = \frac{\psi_1}{\psi_0}$, where ψ_0 is the amplitude of the incoming wave and ψ_1 the sum of amplitudes of the reflected waves propagated in the direction of the wave vector k_1.

Each wave in this sum should be taken with a phase shift p^2 which describes the phase accumulated while the wave was travelling back and forth in a film with the thickness d between two interfaces

$$p^2 = e^{i2k_2 \sin\alpha_2 d}. \tag{2.16}$$

By summing up all the results of all possible reflections and simplifying the equation, the reflectivity can be written as

$$r_{slab} = \frac{\psi_1}{\psi_0} = r_{12} + t_{21} r_{23} t_{21} p^2 + ... = r_{12} + t_{21} r_{23} p^2 \frac{1}{1 - r_{23} r_{12} p^2}. \tag{2.17}$$

However, due to the nature of thin film growth, thin films sometimes consist not of a single layer (2 interfaces), but $N > 1$ layers with $N + 1$ interfaces. A suitable method to approach this is the Parratt formalism which allows extracting an exact result for each slab according to

$$r_{N-2,N-1} = \frac{r'_{N-2,N-1} + r_{N-1,N} p^2_{N-1}}{1 + r'_{N-2,N-1} r_{N-1,N} p^2_{N-1}}. \tag{2.18}$$

This formalism is continued recursively until the total reflectivity amplitude on the first layer is obtained. For a deeper insight on this topic, it is referred to the books from Tolan as well as Als-Nielsen and McMorrow [64, 65].

Part II.

Materials and methods

3. Materials

This chapter will give an overview of the used materials in this thesis. Starting with the very base of a thin film, the substrates, which are silicon and glass. It will then continue to the main organic molecule, the phenacene and concludes with the inorganics, namely alkali metals and gold.

3.1. Substrates

Thin film growth was performed on two types of substrates. Silicon wafers were mainly used for X-ray and AFM experiments while glass substrates were used for optical measurements like absorption or ellipsometry.

3.1.1. Silicon

P-type silicon {100} wafers with a 6-inch (15.24 cm) diameter and a thickness of 675 ± 25 µm were bought from Micro Chemicals GmbH. Under ambient conditions, they are covered with a thin native silicon oxide layer (SiO_2) of 2 nm. Silicon has a lattice constant of 5.43 Å at a temperature of 25 °C [74].

3.1.2. Glass

Fused silica glass was bought from UQG Optics with a nominal thickness of 500 $\pm$25 µm. The nominal transmittance is approximately 90% in the wavelength range $\lambda = 270 - 2000$ nm. Due to the low surface roughness of ≤ 1 nm, the morphological properties are expected to be similar to silicon.

3.2. Phenacenes

Phenacenes (see Fig. 3.1) belong to the group of polycyclic aromatic hydrocarbons (PAHs). They consist of several fused aromatic rings, starting with three rings (Phenanthrene). According to the nomenclature, the number of benzene rings is indicated in square brackets e.g. [6]Phenacene consists of six fused benzene rings. Compared to pentacene, which also

belongs to the PAHs, phenacenes have a zig-zag-shaped structural alignment of the benzene rings leading to higher stability [75].

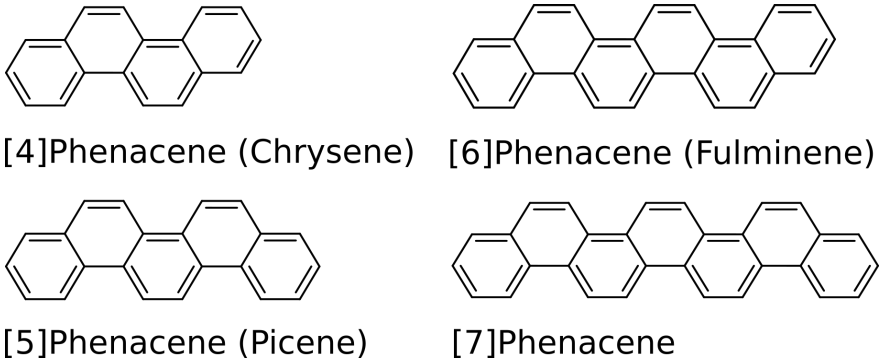

Figure 3.1.: Simplified structural formula representation of several phenacenes.

The first applications of phenacenes in organic electronics were field-effect transistors (FET) with [5]Phenacene (Picene) [76, 77]. They offered p-channel FET characteristics with field-effect mobilities of 1.1 $cm^2\,V^{-1}\,s^{-1}$ and higher stability of FET properties when exposed to O_2 atmosphere. These advantages were also found in other [n]Phenacenes where similar promising aspects were reported [78–81]. Especially [6]Phenacene (Fulminene) offered a field-effect mobility of 3.7 $cm^2\,V^{-1}\,s^{-1}$ as well as similar O_2 sensing properties compared to Picene [82] but even higher field-effect mobilities with up to 7.4 $cm^2\,V^{-1}\,s^{-1}$ were found [83] which makes phenacenes a very promising material for optoelectronic devices. The HOMO/LUMO energy values of [6]Phenacene are $-5.5/-2.4$ eV which results in an optical band gap of 3.1 eV. These values decrease slightly with increasing benzene rings [84] which is shown in Figure 3.2. Surprisingly, specific phenacenes have also shown dopant-induced superconductivity [31, 32, 85] and even other applications like potassium ion batteries show promising results [86].

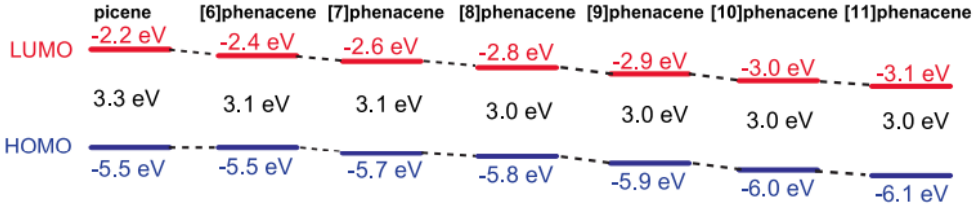

Figure 3.2.: Energy diagrams of [n]Phenacene with the optical HOMO-LUMO gap in black. Image is taken from Ref. [84].

An overview of the most popular phenacenes with their crystal structure data is shown in Table 3.1. The crystal system structure is monoclinic, therefore α and γ have values of 90 degrees.

The space group of [4]Phenacene (Chrysene) is C_{2c} with a symmetry group of C^6_{2h}. [5-7]Phenacene are in the same space group $P2_1$ but have a different symmetry group. Picene

Table 3.1.: Crystal structure data of different phenacenes.

	a [Å]	b [Å]	c [Å]	β [°]
[4]Phenacene [87]	8.4	6.2	22.8	96.5
[5]Phenacene [88]	8.48	6.15	13.52	90.5
[6]Phenacene [89]	8.4	6.2	32	98
[7]Phenacene [78]	8.4381(8)	6.1766(6)	17.829(2)	93.19(1)

and [7]Phenacene are in the C_{2v} symmetry group while [6]Phenacene is in the C_{2h} symmetry group [80]. In terms of growth, Picene as well as [6]Phenacene show a thickness-dependent change of the molecular and structural arrangement as well as the electronic properties [90, 91]. The transition dipole moment is oriented along the long molecular axis [92]. The structure and morphology of [6]Phenacene ($C_{26}H_{16}$) thin films is a part of this thesis and will be further discussed in the results section.

For this thesis, [6]Phenacene was bought from NARD Co Ltd. (Japan) with a purity of 99.9%. Information about the synthesis of several phenacenes can be found in Refs. [76, 93, 94].

3.3. Alkali metals

Alkali metals belong to the first main group in the periodic system. They have only one weakly bound electron in the highest occupied s-orbital and are highly reactive. Chemical reactions entailing an enormous heat production can already occur under ambient conditions in air, therefore they are usually stored in a vacuum or oil atmosphere. Alkali metals have a large range of applications, ranging from fertilizers, fireworks, and atomic clocks to semiconductor applications. Inorganic semiconductors doped with a small amount of alkali metals can drastically change their electrical properties and offer a wide range of further applications. The lattice parameters of the crystal structure of the alkali metals used in this thesis are shown in Table 3.2.

Table 3.2.: Overview of the crystal structure of alkali metals.

Alkali metal	$a/b/c$ [Å]	$\alpha/\beta/\gamma$ [°]
Potassium (K) [95]	5.328	90
Rubidium (Rb) [96]	5.585	90
Caesium (Cs) [97]	6.141	90

Alkali metals were deposited onto organic thin films by using alkali metal dispensers bought from SAES getters (Italy). The FT 10+10 series (see Fig. 3.3) have been used with

an active length of 12 mm and an activation current from 4.5 - 7.5 A. The content of each molecule is shown in Table 3.3.

Table 3.3.: Overview of the alkali metal dispensers used with the respective contents. Taken from Ref. [98].

Alkali metal	Content [mg]
Potassium (K)	2.9
Rubidium (Rb)	4.5
Caesium (Cs)	5.2

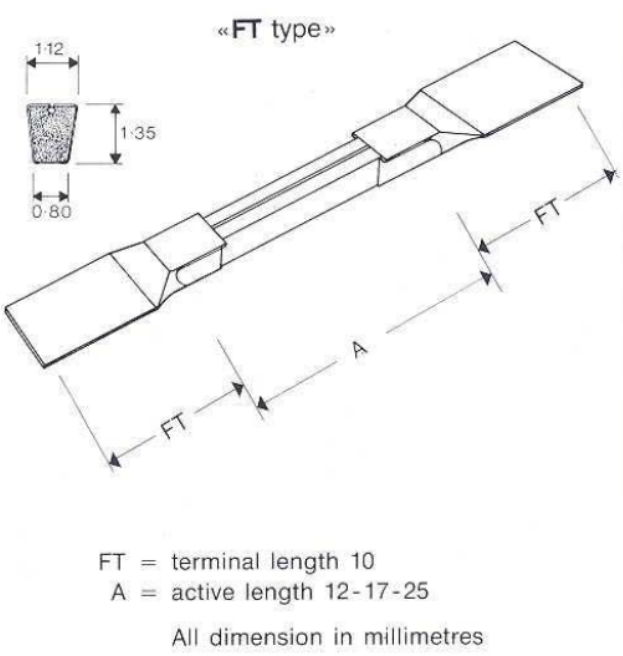

Figure 3.3.: Schematic illustration of an alkali metal dispenser. Image taken from Ref. [98].

The dispensers consist of two terminals where a current can be applied to start the deposition. The active part of the dispenser is a metal container that holds the used molecules. The applied current depends on the alkali metal dispenser as well as the preferred deposition rate. A sketch of the dispenser is shown in Fig. 3.3. The active part consists of a mixture of an alkali metal chromate with the formula X_2CrO_4 where X is the symbol for the alkali metals (K, Cs, Rb) used in this thesis as well as the reducing agent St 101 which consists of 84% Zr and 16% Al. By applying a current and therefore heating up the dispenser, a redox reaction occurs between the metal chromate and the St 101 alloy. That causes pure alkali metals to be evaporated [99, 100]. The detailed redox reaction that occurs is sketched below with X as the alkali metal K, Cs or Rb.

Oxidation: $Zr \longrightarrow Zr^{4+} + 4\,e^-$
Reduction: $4\,X^+ + 2\,CrO_4{}^{2-} + 4\,e^- \longrightarrow 4\,X + 2\,CrO_4{}^{2-}$
Redox reaction: $Zr + 2\,X_2CrO_4 \xrightarrow{\Delta T} 4\,X + Zr(CrO_4)_2$

The rate of alkali metal evaporation can then be controlled by changing the dispenser current while controlling the desired rate with a quartz crystal microbalance (QCM).

3.4. Gold

Gold (Au) is a chemical element with an atomic number of 79. It is a transition metal with good conductivity as well as ductility. It has also no toxicity and low reactivity that leads to a general resistance regarding oxidation and corrosion. This makes gold very useful in electronic applications where it is commonly used as a contacting material for electrical contacts. The lattice parameters of the fcc crystal structure of gold are shown in Table 3.4. The gold structure was plotted with the software Mercury [101] and is visualised in Figure 3.4.

Table 3.4.: The crystal structure of gold.

	$a/b/c$ [Å]	$\alpha/\beta/\gamma$ [°]
Gold (Au) [102]	4.0704	90

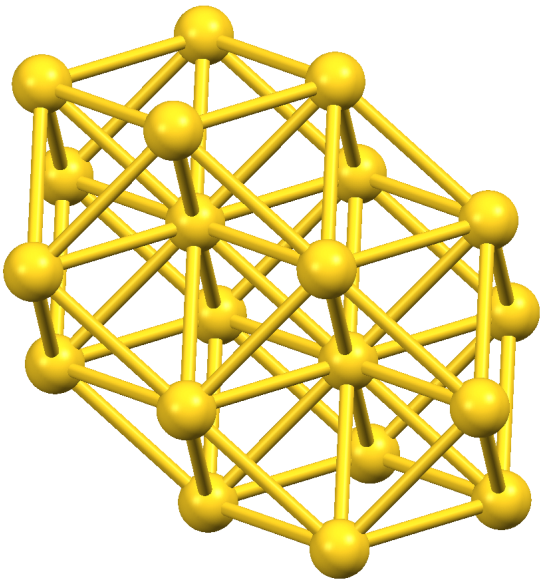

Figure 3.4.: Side view of the gold unit cell structure. Visualized from Ref. [102].

Gold granulate was bought from ESG Edelmetall-Service (Germany) with a purity of 99.9%.

4. Experimental methods

This chapter will give an overview of the experimental methods utilized in this thesis. It will start with a brief introduction to vacuum technology and organic molecular beam deposition, which were important for the growth of thin films. The chapter will then cover various analysis methods and is mainly split into X-ray and non-X-ray methods, starting with X-ray production and concluding with atomic force microscopy and optical methods.

4.1. Vacuum technology

A properly well-maintained vacuum inside the deposition chamber is crucial for contaminant free as well as reproducible thin film samples. Therefore this subsection covers a brief introduction to vacuum technology. This subsection is based on the books [103–105].

Air is a mixture composed of several different gases. These are mostly nitrogen ($N_2 \approx 78\%$) and oxygen ($O_2 \approx 21\%$) but also many other components like hydrogen (H), helium (He) or argon (Ar) are part of this mixture and have to be taken into account when discussing vacuum technology. The average air pressure is around 1013 mbar (≈ 10.13 Pa) depending on the current humidity, temperature and distance to sea level. To get an insight into the number of particles and the impact on molecule deposition at this pressure, the kinetic gas theory can be used. Starting with the Avogadro constant which gives the number of particles per mol:

$$N_A = 6.022 \cdot 10^{23}\ \mathrm{mol}^{-1}. \tag{4.1}$$

By using the number of particles N, the amount of substance ν can then be written as:

$$\nu = \frac{N}{N_A}. \tag{4.2}$$

By using the ideal gas law $\frac{p \cdot V}{T} = \text{const}$ with the pressure p, the volume V and the temperature T it can be rewritten by using the Gas constant $R = k_B \cdot N_A \approx 8.314 \frac{\mathrm{J}}{\mathrm{mol \cdot K}}$ with the Boltzman constant k_B.

$$p \cdot V = \nu \cdot R \cdot T \tag{4.3}$$

The particle density is defined as $n := \frac{N}{V}$ and can be transformed by using Equation 4.3 which gives us the particle density at normal conditions of $T_n = 273.15$ K and $p_n = 1013.25$ mbar:

$$n_n = \frac{p_n}{k_B \cdot T_n} = 2.687 \cdot 10^{25} \mathrm{m}^{-3}. \tag{4.4}$$

A moving particle in this environment exhibits collisions with other particles after a certain travel distance. The average distance without collisions of a particle with the diameter d can be defined as the mean free path λ and is written as:

$$\lambda = \frac{1}{\sqrt{2} \cdot \pi \cdot d^2 \cdot n} = \frac{k_B \cdot T}{\sqrt{2} \cdot \pi \cdot d^2 \cdot p} \tag{4.5}$$

To ensure a contaminant-free deposition of molecules onto a substrate a low particle density (see Eq. 4.4) which then leads to a high mean free path (see Eq. 4.5) is preferred. The overview of the corresponding values for particle density and mean free path depending on the pressure range and vacuum level can be seen in Table 4.1.

Table 4.1.: Overview of vacuum levels and characteristic values at $T = 300$ K. Taken from Ref. [104].

Vacuum type	Pressure p [mbar]	Particle density n [cm^{-3}]	Mean free path λ [m]
Rough (RV)	$1000 - 1$	$10^{19} - 10^{16}$	$10^{-7} - 10^{-4}$
Medium (MV)	$1 - 10^{-3}$	$10^{16} - 10^{13}$	$10^{-4} - 0.1$
High (HV)	$10^{-3} - 10^{-7}$	$10^{13} - 10^{9}$	$0.1 - 10^{3}$
Ultra-high (UHV)	$< 10^{-7}$	$< 10^{9}$	$> 10^{3}$

Another important aspect of maintaining a good vacuum is the monolayer time τ which is responsible for sorption and diffusion onto the substrate such as oxygen that sticks onto the surface of a freshly cleaned silicon substrate.

For a molecule that sticks on the surface without re-evaporation and air, the average time for the formation of one monolayer is defined as:

$$\tau = \frac{3.6 \cdot 10^{-6}}{p\ [mbar]}\ [s]. \tag{4.6}$$

It can reach values from 10^{-9} seconds at 1000 mbar up to values of > 36 seconds at ultra-high vacuum at $p < 10^{-7}$ mbar.

To reach and maintain such a high vacuum, different pumps for different pressure levels have to be used (see Fig. 4.1). UHV systems for organic molecular beam deposition or X-ray measurements consist of several connected pumps that cover different pressure ranges. To start pumping from ambient pressure, several types of rotary or sorption pumps are available. The most common types are oil pumps, scroll pumps and membrane pumps. The working principle is simple. Gas is sucked in by an inlet, compressed with a rotor or membrane system

and discharged through an outlet into the atmosphere. The ultimate pressure that can be reached with these types of pumps is around $p \approx 10^{-3}$ mbar. After reaching approximately 10^{-2} mbar, usually turbomolecular pumps are used to create pressures down to around 10^{-11} mbar. Turbomolecular pumps are molecular turbines consisting of several stacked layers of blades that can operate with rotor speeds up to 90.000 rpm. Due to the high rotor speed and danger due to overheating, they need a rough vacuum at their exhaust created by a rotary pump for operation. Depending on the size of the vacuum chamber usually, a pressure of 10^{-7} mbar can be expected within several hours. After contact with air, the walls inside the chamber are usually covered with moisture which evaporates slowly and therefore slows down the pressure decrease significantly. To speed up this process, the chamber is degassed at a high temperature which then results in pressures up to 10^{-10} mbar or even lower. For reaching and maintaining this UHV pressure, also other pump types like ion and titanium sublimation pumps are used. Both are capture pumps that capture molecules and bind them to their pump walls.

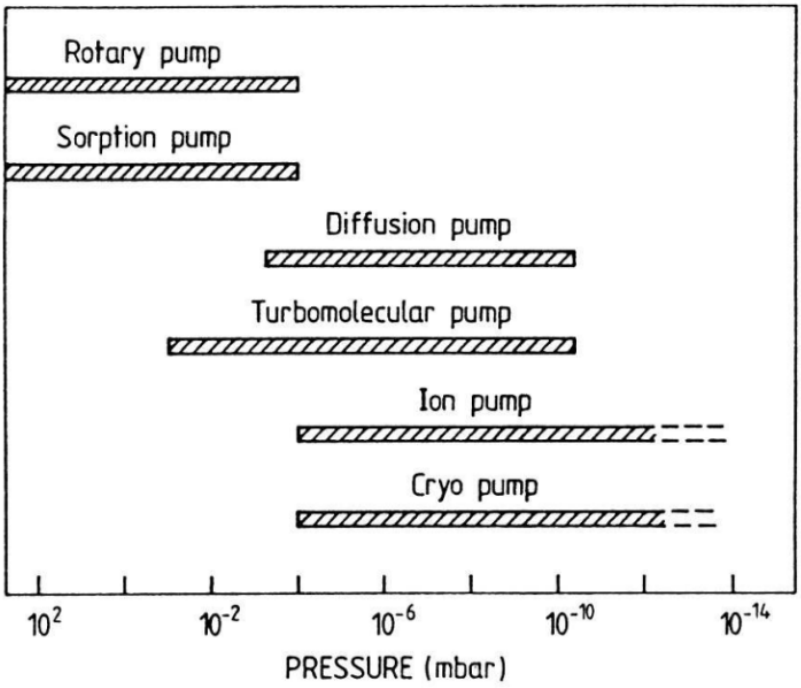

Figure 4.1.: Overview of various vacuum pumps with their usable pressure ranges. Taken from Ref. [106].

4.2. Organic molecular beam deposition

The thin films in this thesis were produced using organic molecular beam deposition (OMBD), which is a suitable method for the growth of well-ordered films [26]. A crucible containing organic molecules is installed inside a Knudsen (effusion) cell [107]. Knudsen cells contain feedthroughs for heating wires, thermocouples as well as an shielding that houses the crucible. A shutter was used above the shielding to start or stop the deposition. Figure 4.2 shows a custom build Knudsen cell that was used with [6]Phenacene molecules.

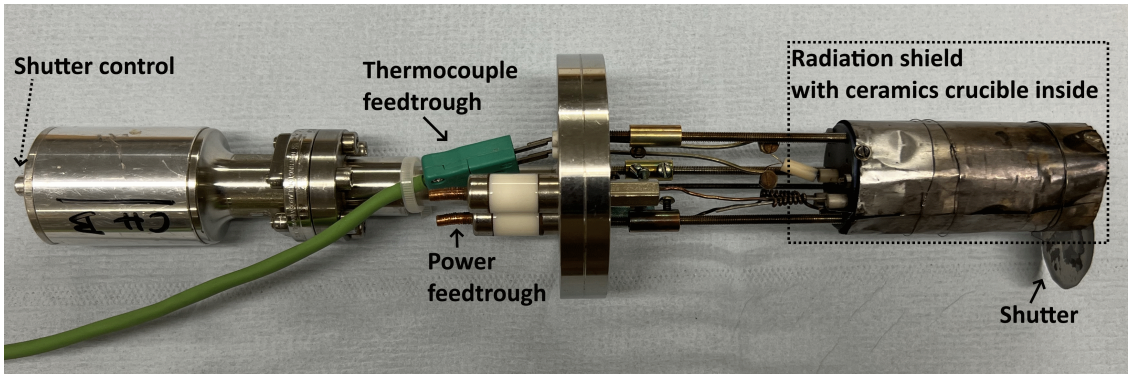

Figure 4.2.: Overview of a Knudsen (effusion) cell for the evaporation of organic molecules.

By heating up the Knudsen cell to a specific temperature, the molecules start to evaporate and can then be absorbed onto a substrate to form a thin film. Figure 4.3 shows an overview of the experimental setup used for film growth.

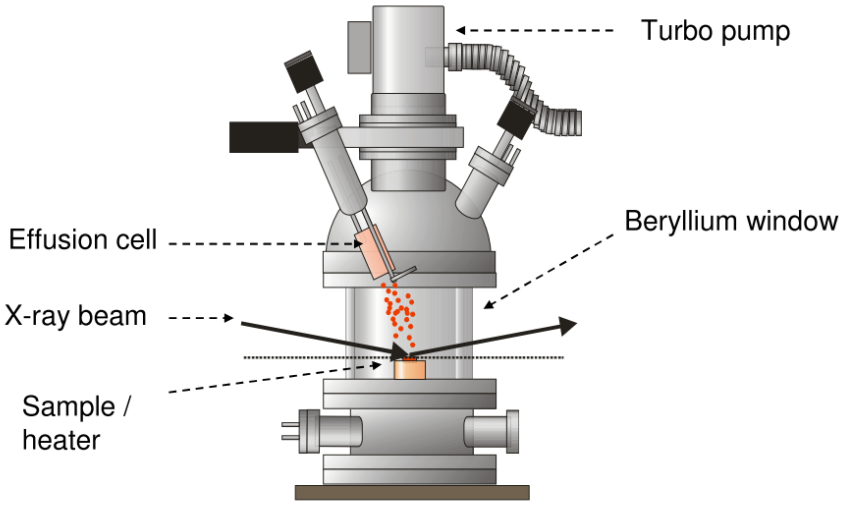

Figure 4.3.: Small UHV chamber for thin film deposition. Taken and modified from Ref. [71].

The Knudsen cell was mounted onto a small portable UHV chamber. Due to the top-

down mount, the materials inside the crucible had to be fixed using glass wool. The UHV chamber contained a substrate holder that was able to be cooled down with liquid nitrogen to sub-zero as well as heated up to 500 °C. The chamber was pumped down to UHV conditions of $10^{-7} - 10^{-9}$ mbar using a membrane as well as a turbo pump. It was also possible to install a second Knudsen cell or a feedthrough cell for the deposition of alkali metals. To observe the deposition rate and thickness, a water-cooled quartz crystal microbalance (QCM) [108] in the vicinity of the Knudsen cell was used. The chamber was equipped with a beryllium window and could be mounted on standard diffractometers making in-situ X-ray experiments possible [59, 109]. Stationary UHV chambers were also used especially for gold deposition due to the ability to mount a metal evaporation cell. By using a load lock for sample transport and using additional pumps like ion and titanium sublimation pumps those chambers were able to reach pressures up to $10^{-10} - 10^{-11}$ mbar.

4.3. Sample preparation

The substrates (silicon as well as glass) were cut into 5×10 mm or bigger pieces. Usually, silicon was cut along the {100} axis with a 10° miscut to reduce the silicon Bragg diffraction in X-ray imaging. Afterwards, the substrates were cleaned for 15 minutes each using an ultrasonic bath with acetone (purity $\geq$ 99.8%) as well as isopropyl alcohol (purity 99.9%), both bought from Sigma-Aldrich. The substrate holder in the small deposition chamber [109] was also cleaned with both solvents and tissues before mounting the substrates. For in-situ real-time experiments or experiments with stationary chambers, the substrates had to be fixed onto the substrate holder due to the tilting of the substrate holder during measurements or the sample transfer. This was done by using small amounts of silver paste or Gallium-Indium eutectic. For the gold deposition in the XPS chamber, a special substrate holder was used which was cleaned using the same methods. In this case, the substrates were mounted using a special adhesive tape. To prevent contamination also the tips were cleaned regularly. After closing and pumping down the chamber to a high vacuum, the substrate holder was heated up to 450 °C for around 12 hours to get rid of contaminations. The Knudsen cell (for organic molecule deposition), as well as the feedthrough cell (for alkali metal deposition), were also heated up to around 100 °C for 6 hours for the same reason. The cooldown to room temperature after this process was usually done overnight to get a lower pressure.

4.4. X-ray methods

Applying X-ray scattering on organic-inorganic surfaces was the main technique for analyzing thin film properties in this thesis. This section will start with a brief introduction to X-ray sources and detectors. Especially synchrotron radiation is crucial for in-situ real-time experiments. Afterwards, several analysis methods that use X-rays will be introduced. The contents of this section were mostly taken from the book of Als-Nielsen and McMorrow [65]. An introduction to X-ray scattering processes can be found in section 2.6.

4.4.1. X-ray sources and detectors

X-ray tubes are the most common sources of X-rays. By heating up a filament, electrons are produced which are then accelerated towards an anode. After hitting the anode, the electrons are subsequently decelerated, producing bremsstrahlung as well as characteristic radiation which depends on the anode material (see Fig. 4.4). Simple X-ray tubes use water cooling to keep the anode temperature stable. However, due to the simple design, the maximum power and thus beam intensity is limited, so other types were invented such as rotating anodes, where only a part of the anode is irradiated, resulting in an overall higher output power.

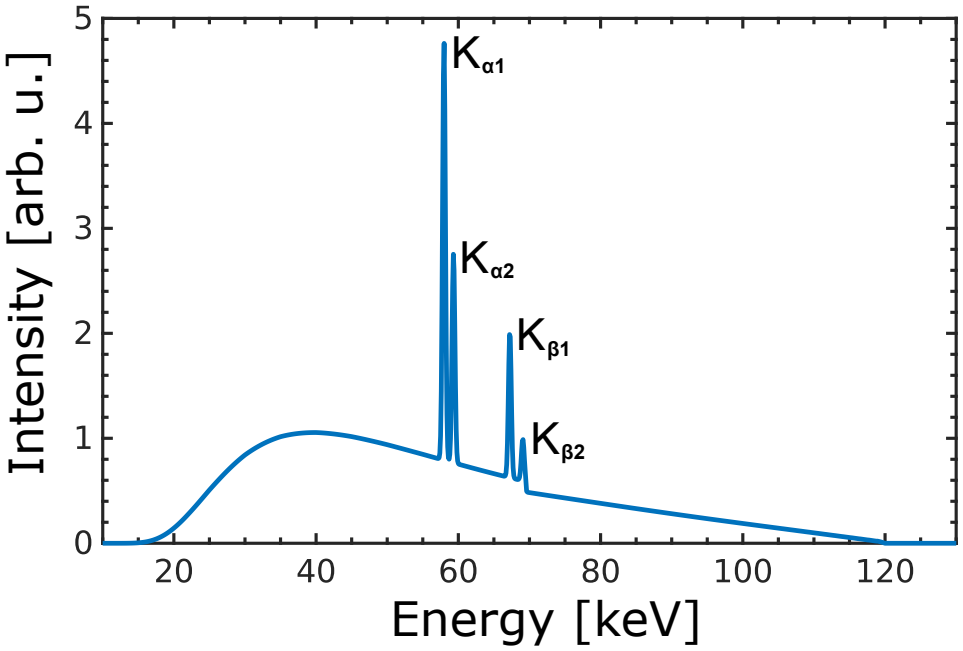

Figure 4.4.: X-ray spectra from a standard X-ray tube that shows continuous radiation (bremsstrahlung) which is dependent on the energy as well as discrete lines ($K_{\alpha1,2}$, $K_{\beta1,2}$) from a copper anode. Adapted from Ref. [110].

For scattering experiments usually, a monochromatic beam is used by utilizing the copper K-alpha line (K_α). Therefore only a small fraction of the total X-ray spectra is used, which leads to a smaller photon flux and therefore smaller measured intensities and longer acquisition times. This leads to disadvantages when trying to measure in-situ real-time data with standard laboratory sources. Another method to generate X-rays without these drawbacks are synchrotrons, which will be discussed in the next section. The scattered X-rays can then be recorded by using various types of detectors. The most common type are 2D-area detectors. These consist of an array of charge-coupled device (CCD)-chips that convert X-rays into electrical signals by using the photoelectric effect. The measured 2D signal, which depends on the photon flux as well as the photon energy can then be used for different types of scattering experiments which will be discussed in one of the next sections.

4.4.2. Synchrotron radiation

Synchrotron sources offer high-quality X-ray beams for scattering experiments. Higher intensity of the X-ray beam results in a higher scattering signal, which allows one to study smaller samples and perform faster measurements which is crucial for in-situ experiments. A small collimation (given in mRad) is also favourable because an X-ray beam diverges as it propagates. Focusing X-rays on a small object is easier for smaller source areas therefore a small value (given in mm^2) is also important. Depending on the source, various photon energies contribute differently to the measured intensity. Therefore, a fixed relative energy bandwidth (BW) for the monochromator crystal of 0.1% has been defined. All these aspects can be combined in the single term "Brilliance" which is determined by the Equation 4.7.

$$\text{Brilliance} = \frac{\text{Photons/second}}{(\text{mRad})^2 \cdot (\text{mm}^2 \text{ source area}) \cdot (0.1\% \text{ BW})} \tag{4.7}$$

Synchrotron radiation is produced by charged particles travelling at relativistic speeds in curved paths due to experiencing an acceleration perpendicular to their movement direction which is a direct consequence of the Maxwell equations. The X-rays are generated when electrons are accelerated in a magnetic field created by bending magnets or specially designed insertion devices (wigglers and undulators). The X-rays created from electrons are then transferred to one of the beamlines which are specialized for different scientific setups or measurement methods.

In this thesis, synchrotron facilities at ESRF (Grenoble, France) and PETRA III (DESY, Hamburg, Germany) were used. Both synchrotrons work with an electron energy of 6 GeV, a brilliance up to 10^{21} (photons per second) / ($mRad^2$ mm^2 0.1% bandwidth) and a beam current of 100 mA (PETRA III) or 200 mA (ESRF). At PETRA III, the beamlines P03 and P23 have been used with a mobile UHV chamber. P03 is specialized in grazing incidence

experiments like GIWAXS/GISAXS while P23 was used for diffraction experiments with the availability of fast energy tuning between 5 and 35 keV. At ESRF the beamlines ID10 and BM32 offered X-ray diffraction as well as grazing incidence methods. While ID10 allowed the mounting of our own mobile UHV chamber, BM32 was already equipped with a stationary UHV chamber that could be used for the evaporation of metals. BM32 also uses bending magnets instead of undulators for electron injection.

Radiation leads to beam damage in the organic samples which is a very relevant problem when performing synchrotron experiments due to the high flux. X-rays that are hitting a sample are generating electrons due to the photoelectric effect or Auger emission. These electrons lead to inelastic scattering which is sufficient to break several bonds [111] in the carbon and hydrogen structure. Further effects are mass loss of the sample due to the escape of light gaseous elements like hydrogen, nitrogen and oxygen [112]. These effects are visible as an intensity decrease of Bragg reflections, especially when a sample is being measured over long periods of time e.g. in in-situ real-time experiments. To avoid this effect, pre-deposited thin films were brought to the beamline to find out the correct absorber settings for the in-situ measurements. The goal was to get an equilibrium between minimum beam damage and good image quality. Additionally, shorter measurement times can be used to minimize beam damage. Due to the small beam width, the beam damage is concentrated on a small spot. Therefore the beam spot was changed to a fresh one after long measurements.

4.4.3. X-ray reflectivity

X-ray reflectivity (XRR) is used to investigate the out-of-plane structure of thin films. The acquired data were used to get an insight into the thickness, roughness and lattice parameter of the samples. This subsection will cover the basics of this technique. For a deeper introduction to XRR, the reader is referred to the book of Tolan [64]. A beam of X-rays is hitting a crystalline sample under the angle θ_{in}. The beam is then reflected under the same angle θ_{out} and subsequently measured by an X-ray detector as shown in Figure 4.5.

By changing the angle of the X-ray source and the detector simultaneously, i.e. $\theta_{\text{in}} = \theta_{\text{out}}$, an XRR curve is obtained. An example measurement is shown in Figure 4.6.
The XRR pattern consists roughly of four parts that can be used to describe different aspects of the thin film. The first part is the total reflection edge which occurs under a very small angle. This happens because the refractive index of X-rays is lower than that of the surrounding medium (air, vacuum) and therefore the incident beam is completely reflected by the surface of the thin film. This can be used to determine the electron density of a thin film. For inorganic materials on top of a silicon substrate, the electron density of the film is higher than the electron density of the silicon substrate and therefore the edge position can be used to determine the density of the film. However, organic materials have

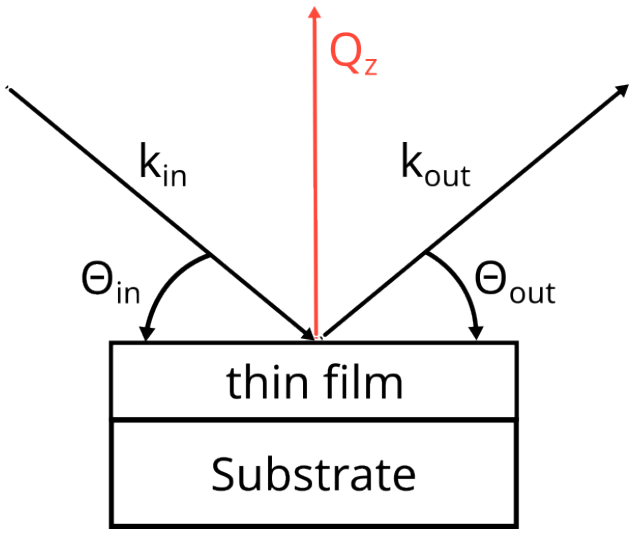

Figure 4.5.: Schematic representation of an XRR measurement. An incoming beam with the wave vector k_{in} and the angle of incidence $\theta_{\text{in}} = \theta_{\text{out}}$ is hitting a thin film grown on a substrate. The beam is reflected with the wave vector k_{out}.

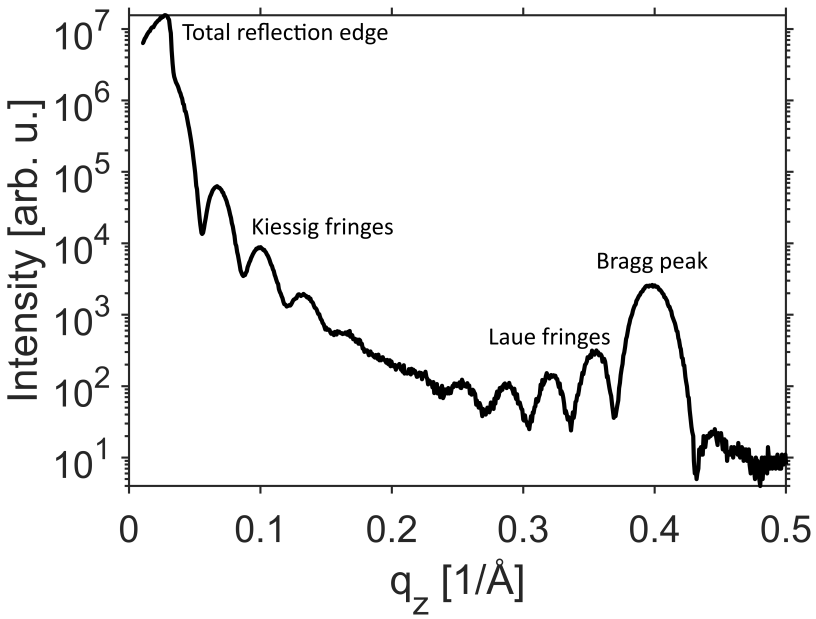

Figure 4.6.: XRR data of [6]Phenacene grown at 2 Å/min with a final thickness of 18 nm shows several parts that can be used for further evaluations as described in the text. The intensity is plotted in a logarithmic scale.

a lower electron density than the substrate, which is why two critical angles are observed for sufficiently thick layers, the lower one referring to the organic film and the second one to the silicon substrate. The second part is caused by the wave interference of the reflections on the top and bottom interface of the thin film and leads to the appearance of Kiessig fringes/oscillations. The periodicity and damping of these fringes can be used to calculate the average thickness D and surface roughness σ of the sample. By using the distance of two Kiessig fringes $\Delta q_z = \frac{2\pi}{D}$ a rough estimation of the average thickness can be done. The last part are the Bragg peaks that are caused by the constructive interference of waves diffracted by the crystal lattice in the out-of-plane direction. They are a direct consequence of Bragg's law

$$2 \cdot d \cdot \sin\theta = n \cdot \lambda, \tag{4.8}$$

with the distance between crystallographic planes (lattice spacing) d, the angle of incidence θ, an integer number n and the wavelength λ of the reflected X-rays.

Bragg peaks are also surrounded by Laue oscillations which are caused by interference from the crystalline domain structure. These fringes can also be used to make an approximation of the size of coherent crystalline domains but it has to be taken into account that Laue fringes are sensitive to crystalline disorder, while Kiessig fringes are sensitive to the interface properties. Therefore both of them provide only complementary information. By using the wavelength of the X-ray source the XRR plot can be transformed into reciprocal space to make it comparable to other X-ray sources

$$q_z = \frac{4\pi}{\lambda} \cdot \sin\theta. \tag{4.9}$$

By using the position of the Bragg peak, the distance between crystallographic planes d can be calculated

$$d = \frac{2\pi}{q_z}, \tag{4.10}$$

as well as the lattice parameter a

$$a = \frac{2\pi}{q_z}\sqrt{h^2 + k^2 + l^2}. \tag{4.11}$$

Additionally, by using the FWHM of a previously fitted peak it is possible to calculate the crystallite size

$$l = \frac{2\pi}{\mathrm{FWHM}}. \tag{4.12}$$

The Equations 2.12 and 2.13 with the classical radius of an electron r_e can be used to

calculate the electron density ρ of a thin film with the position of the total reflection edge in q-space q_c. The resulting equation is shown below:

$$\rho = \frac{q_c^2}{16\pi r_e}. \tag{4.13}$$

A GE inspection technologies XRD 3003 TT with copper K-alpha radiation ($\lambda_{K\alpha}$ = 1.54 Å) was used to acquire XRR data in the laboratory. However, to acquire high-quality real-time data, several beamlines at DESY (P23) and ESRF (ID10, BM32) have been used. The standard way of data evaluation was the program GenX [113] that uses the Parratt formalism [114] to simulate X-ray reflectivity curves for thin films consisting of several layers. A faster way to determine thin film properties, especially the average thickness and the surface roughness was a machine learning algorithm developed in our group [115–118].

4.4.4. Grazing-incidence wide-angle X-ray scattering

To study the in-plane structure of prepared thin films, grazing-incidence wide-angle X-ray scattering (GIWAXS) was used. As the name suggests, during the measurement, the X-ray beam hits the sample at a shallow angle (grazing-incidence) close to the angle of total external reflection of the substrate. An example of the setup is shown in Figure 4.7. This creates a large-area beam footprint on the surface of the sample, which allows averaging the information from a significant part of the sample at the same time. In combination with the 2D detectors, a large part of the reciprocal space can be recorded at the same time. This is especially useful for the real-time in-situ study of thin film growth. Furthermore, depending on the angle of incidence, the probing depth can be varied. At very shallow angles of incidence, the penetration depth of an X-ray beam is limited and the measurement is surface sensitive. On the other hand, by increasing the angle of incidence slightly, also the part of the thin film closer to the substrate can be probed.

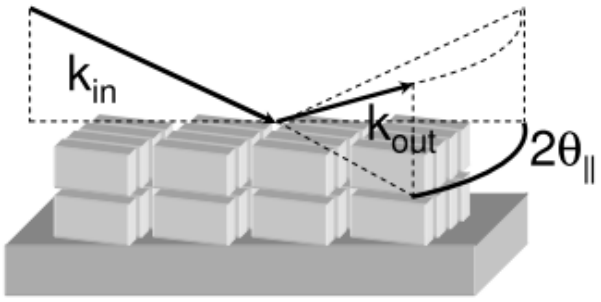

Figure 4.7.: Overview of the grazing incidence scan geometry probing the upper film layers. Taken from Ref. [71].

Another method that uses the grazing-incidence geometry is called grazing-incidence

small-angle X-ray scattering (GISAXS). During the GISAXS measurement, the focus is on the low q-range of the reciprocal space. To increase the resolution of this part of the reciprocal space, the detector is positioned further away from the sample, i.e., the sample-to-detector distance (SDD) is larger. The geometry of both grazing-incidence setups is shown in Figure 4.8. GISAXS allows the study of structures with sizes in the range of a few tens to hundreds of nanometers, while GIWAXS is most suitable for smaller structure details in the range of a few nanometers.

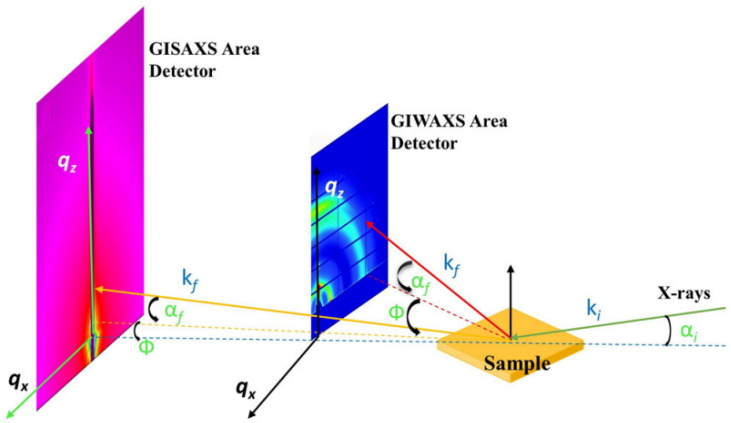

Figure 4.8.: Schematic sketch of the GISAXS and GIWAXS geometry. Image is taken from Ref. [119].

A Xenocs XEUSS 2.0 with copper K-alpha radiation ($\lambda_{K\alpha} = 1.54$ Å) and a Pilatus 300K area detector were used to acquire GISAXS/GIWAXS images in the laboratory. In this thesis, GIWAXS was used to get an insight into the unit cell structure of thin films. The measured reciprocal space maps consist of several Bragg reflections. Randomly oriented films produce isotropic rings, while highly oriented films produce well-defined spots. Partial rings are a sign of partially oriented films with some preferred orientation. Figure 4.9 shows an example of these effects. Further calculations were done using MATLAB which will be discussed in the next two paragraphs taken from Ref. [89].

4.4.4.1. Unit cell determination

The unit cell parameters of thin films were determined from the positions of Bragg reflections in the measured reciprocal space maps. The genetic algorithm (GA) optimization method based on the GIXSGUI package [121] for MATLAB was used. Using the parameters of already known structures, the unit cell parameter c was manually optimized until all of the visible Bragg reflections could be indexed. The positions (q_z and q_{xy}) of the most well-defined Bragg peaks were fitted and subsequently used as constraints for automated GA optimization of the unit cell parameters. The overall distance between experimentally ob-

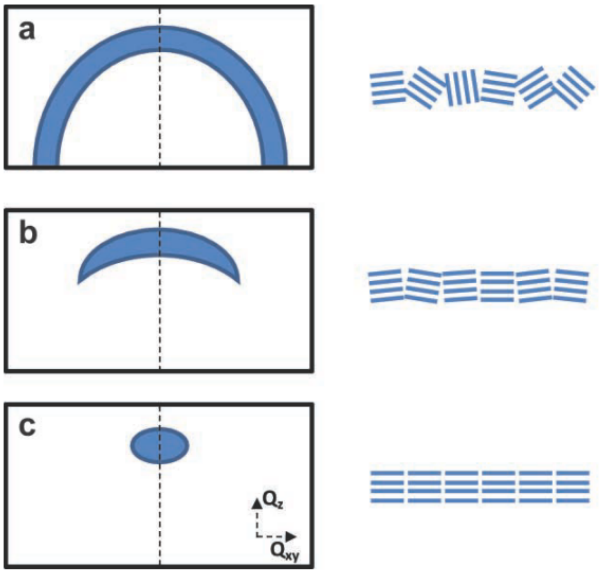

Figure 4.9.: Examples of GIWAXS patterns: a) randomly oriented, b) oriented with some defects and c) highly oriented. Taken from Ref. [120].

served and theoretically calculated Bragg peak positions was defined as the fitness function. The optimization was stopped when the fitness function of the GA reached a predefined value.

4.4.4.2. Molecular orientation

To determine the molecular orientation inside the unit cell, an initial guess was made by positioning a given number of phenacene molecules inside a unit cell with previously determined unit cell parameters. The initial position and orientation of the molecules were chosen such that there is no overlap between neighbouring molecules and the volume of the unit cell was fully occupied. The GA was used to optimize the position and orientation of molecules based on experimental data. During the optimization, all molecules inside the unit cell were randomly rotated and shifted as a rigid object in a predefined range, resulting in several configurations with slightly different positions and molecular orientations. The assumption of rigid objects is expected to lead to reasonable results considering the relative stiffness of phenacenes compared to small organic molecules such as oligothiophenes and alkenes. For each such configuration, X-ray peak intensities were calculated based on the atomic scattering factors. Intensity values calculated from scattering factors were compared with experimentally acquired GIWAXS data. Because of the grazing-incidence symmetry of the experimental measurement, X-ray peak intensities were corrected using Lorentz-polarization correction. The fitness values were assigned to each molecular configuration based on how close the calculated X-ray intensities were to experimentally acquired ones. Configurations

with the best fitness values were then used as starting points for the next iteration. The overlap of neighbouring molecules was calculated for each configuration based on the van-der-Waals radii of atoms. Configurations with overlap greater than 10% were not used in the next iteration of a calculation. After the fitness values for a best individual orientation reached the desired value, the calculation of the molecular orientation was stopped.

4.4.5. X-ray photoelectron spectroscopy

X-ray photoelectron spectroscopy (XPS) is a surface-sensitive technique that is based on the photoelectric effect. The energies that are used are usually $\hbar\omega > 100$ eV for XPS or $\hbar\omega < 100$ eV for ultraviolet photoelectron spectroscopy (UPS). Both methods are also known under the more general term photoelectron spectroscopy (PES). For a deeper introduction, it is referred to the book of Woodruff [122] as well as the publications from Penn [123], Fadley [124] and Papp [125] which were used as a reference for this section.

A photon with an energy of $\hbar\omega$ is irradiated onto a solid surface. The incident photon can then be absorbed by an electron with the binding energy E_B. The result is a photoelectron which is being ejected out of the vacuum level with the kinetic energy

$$E_{kin} = \hbar\omega - E_B. \tag{4.14}$$

Each atom has different binding energies for its orbitals, therefore the equation is solved by E_B

$$E_B = \hbar\omega - E_{kin}. \tag{4.15}$$

E_B can then be used to determine the components of the surface by using an electron energy analyser to determine E_{kin} of the ejected electrons. The excitation process is also illustrated in Figure 4.10. To adjust this equation for solids where the binding energy is referred to as the Fermi-level the equation can be written as

$$E_B = \hbar\nu - E_{kin} - \phi_w, \tag{4.16}$$

with the work function of the material ϕ_w, which represents the minimum energy required to remove an electron from the surface of the material.
It is also worth mentioning that the emitted electron leaves a core hole in the electron shell from which it was liberated, which leads to an energy release of another electron to fill its place and can then lead to a second photoelectron (Auger electron). A more detailed view of secondary electron emissions as well as other phenomena can be found in ref [126]. By using an electron energy analyser, the photoelectrons can be detected and plotted as a function of

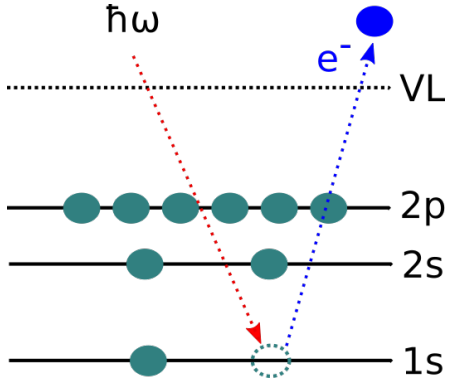

Figure 4.10.: A core-level electron is excited to unoccupied states above the vacuum level (VL) by X-rays which is the fundamental principle for XPS.

counts over the energy $\hbar\omega$. Fitting the relevant peak areas of the spectra can be used for the investigation of surface reactions or chemical analysis [125, 127, 128]. Another interesting aspect is the calculation of coverages on the sample which can be done by using the equation

$$\sigma_A = \frac{E_A}{E_B} \cdot \frac{I_A}{I_B} \cdot \frac{\mu'_s}{\mu'_a} \cdot \frac{N\lambda_s\sigma_s \cos\phi}{M_s}, \tag{4.17}$$

with the surface concentration σ_A in cm^{-2}, the adsorbate A, the substrate B, the kinetic energy E, the integrated peak intensity I, the modified photoelectron cross-section μ', Avogadro´s number N, the escape depth of photoelectrons through the substrate λ_s, the substrate density σ_s, the emission angle with respect to the surface normal ϕ and the molar mass of the substrate M_s [129]. XPS can also be used to approximate the thickness d of the sample, which is very useful when other methods do not provide reliable data. Additional atoms on top of an existing layer lead to a decrease of the signal intensity from the lower layer I_0. By using the intensity ratio $\frac{I}{I_0}$ together with the inelastic mean free path λ the resulting equation can be written as

$$\frac{I}{I_0} = \exp\left(\frac{-d\cos\phi}{\lambda}\right). \tag{4.18}$$

In this thesis, a Scienta Omicron [130] Sphera II electron energy analyser was used. It offers parallel detection with 7 channeltrons. The radiation was provided by a DAR 400 X-ray source with an aluminium anode. An anode voltage of 15 kV and a filament current of 4 A was used without a monochromator. The measurement was analysed with the software EIS-Sphera with a Constant Analyser Energy (CAE) of 50 eV. Further calculation was done by the software CASA XPS [131] to fit the relevant peak areas.

4.5. Atomic force microscopy

Atomic force microscopy (AFM) is used to gain insight into the surface morphology of the samples. The contents of this section were taken from the JPK AFM handbook [132] which is from the AFM machine that was used in this thesis. From the topography of the prepared samples, it is possible to determine the growth regime of a thin film (layer-by-layer, island formation or layer-plus-islanding) and the grain size. Depending on the conditions during the thin film preparation, such as substrate temperature and deposition rate, grains of different sizes are formed. For the applications in organic semiconducting devices, large grain sizes, and therefore the low density of grain boundaries, are highly desirable [133]. To estimate the grain size from the AFM measurement, the image has to have a sufficiently high resolution to distinguish individual grains. A variety of automated methods for grain marking as well as manual grain counting per area can be used to determine the average grain size. The experimental setup consists of a cantilever with a small tip which was moved over the sample. The tip can be either in direct contact with the sample (contact mode) or tapping over it with a high frequency created by a quartz crystal (tapping or intermittent contact mode). In both cases, a laser beam is directed onto the tip which is reflected and then captured by a photodiode. While probing the sample line by line, its structure leads to a variation of the cantilever height during the measurement changing the deflection of the laser and by examining the intensity of the reflected beam, a height profile of the sample can then be created. Figure 4.11 shows a simplified version of the experimental setup.

In intermittent contact mode, the oscillation of the tip is described by the function $f = \frac{1}{2\pi} \cdot \sqrt{\frac{k}{m}}$ with the resonance frequency f, the tip constant k and the mass of the cantilever m. This method is very suitable for sensitive molecules that are not completely fixed on the surface. Unfortunately, there is also a higher probability of complications due to sticky molecules that can contaminate the tip. Overall, AFM is a great tool for the imaging of organic semiconductors due to the possibility to measure a 3D surface profile without the need for further preparation of the sample.

In this thesis, a JPK Nanowizard II AFM was used. The device was placed on top of an anti-vibration table (Micro 40 from Halcyonics). The AFM was equipped with an antimony n-doped silicon TESPA-V2 tip from BRUKER [134] with a length of 127 µm and a lattice constant of 42 $\frac{\mathrm{N}}{\mathrm{m}}$. The images were acquired in tapping mode usually with a resolution of 512 x 512 pixels and an area of 5 x 5 μm. Image evaluation was mainly done using the software Gwyddion [135] by applying mean plane subtraction, row alignment and scar correction to every image. The colour range was altered for best contrast and the minimum height value was shifted to zero. In terms of data evaluation, mainly the RMS roughness and plot profile were extracted from the images.

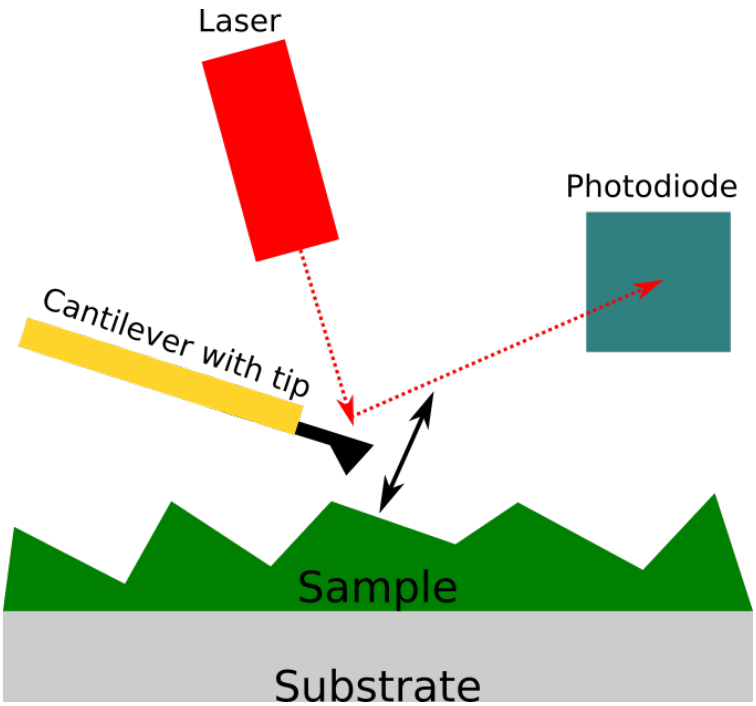

Figure 4.11.: Schematic view of an AFM measurement. A cantilever is moved over a sample while measuring the tilt with a laser and photodiode.

4.6. Scanning electron microscopy

An alternative method to obtain surface morphology imaging is scanning electron microscopy (SEM). For the contents of this section, it is referred to the books from Goldstein [136] and Ul-Hamid [137]. Compared with a light microscope, images are obtained by a beam of high-energy electrons instead of photons. Usually, the maximum resolution of a microscope can be described by using the Abbe-limit

$$g = \frac{\lambda}{A}, \tag{4.19}$$

with the wavelength λ and the numerical aperture A. To increase the resolution the numerical aperture can be increased or the wavelength of the beam can be decreased. SEM uses wavelengths of $0.2479 - 0.0413$ nm, which is much lower than the wavelength of visible light ($380 - 760$ nm). This leads to a useful magnification factor of 200000x compared with 1000x of a standard light microscope. A typical SEM system (see Fig. 4.12) consists of two parts that are kept in a vacuum: An electron column where the electrons for the measurement are produced and focused, a specimen chamber which houses the sample and an electron detector. A computer system is used to evaluate the data.

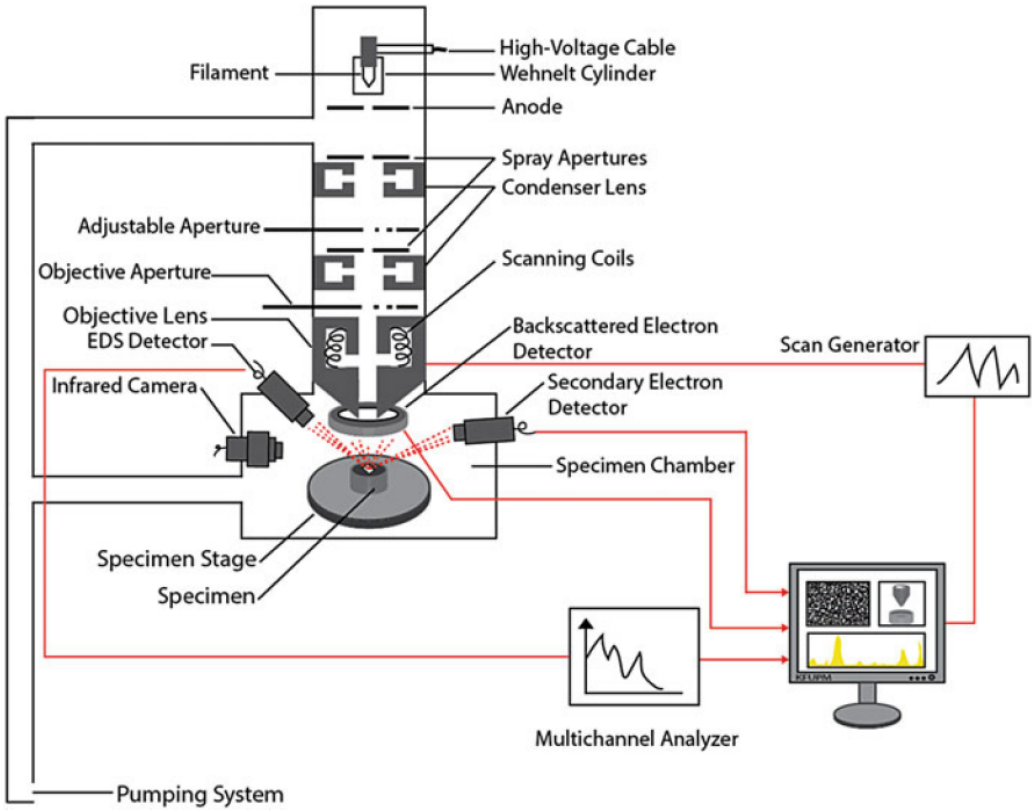

Figure 4.12.: Overview of a typical SEM system. Taken from Ref. [137].

To create an electron beam, a cathode filament is heated up with a voltage between 5 and 30 kV and the generated electrons are focused onto the sample with several lenses. The majority of electrons are absorbed by the sample but some electrons are emitted out of the surface. The emitted electrons consist of backscattered electrons (BSE) which are part of the original beam as well as secondary electrons (SE) which are caused by an inelastic event in the sample. SE only occur near the sample surface due to their low energy while BSE has higher energy and therefore a higher penetration depth. Both electron types can then be measured by an electron detector. The signal has no height information but a 3D impression is created due to the contrast. Compared to the AFM technique, the acquisition is faster and also a larger image range is possible, which makes it easier to check if the structure of the sample is homogeneously distributed. To gather topographical data, the SE can be measured while an incidence angle smaller than 90 degrees is being used. It is also possible to gain information about the composition of the material by using the dependence on the atomic number Z.

In this thesis, a Phillips XL30 as well as a Jeol JSM 6500 F, have been used with an voltage of 5 kV.

4.7. Variable angle spectroscopic ellipsometry

The contents of this section were taken from the Woollam Ellipsometer software manual [138]. Variable angle spectroscopic ellipsometry (VASE) is an optical measurement technique that uses the change of a polarized optical beam to determine the optical functions of thin films. To achieve this, a light goes through a polarizer which makes the light linearly polarized before hitting a sample. The reflected (or transmitted) light is then measured by a detector equipped with an analyser. VASE is only dependent on the polarized state of the light and not the intensity, which makes it a very accurate technique to characterize thin films. An overview of the setup is shown in Figure 4.13.

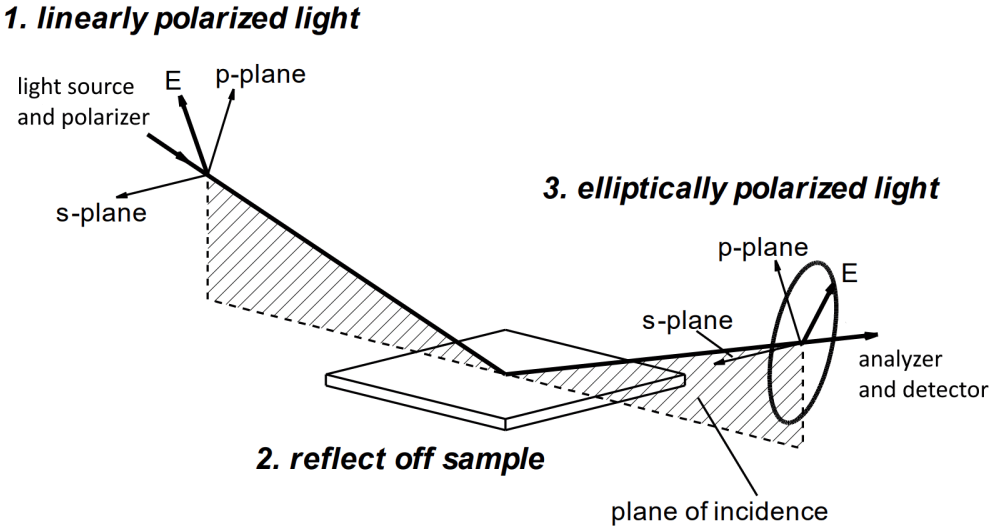

Figure 4.13.: Overview of an ellipsometric measurement. The p- and s-plane (parallel- and perpendicular-plane) of linear polarized light is shifted after reflection from a sample. Taken and modified from Ref. [138].

By moving the corresponding angle of the light source and detector the reflected and transmitted light changes its polarization. This effect depends on the optical properties of the sample and is described by Equation 4.20. ρ is the complex ellipsometric parameter which depends on the Fresnel reflection coefficients R_p and R_s that describe p- and s-polarized light. ψ describes the ratio of the p- and s-direction reflection coefficients for the sample, while Δ is the phase difference between both direction coefficients. Both are the measured values and are described in the last part of the equation

$$\rho = \frac{R_p}{R_s} = \tan(\psi)\exp^{i\Delta}. \tag{4.20}$$

Further analysis was performed by creating and fitting a two-layered model of the thin films, consisting of the substrate and the thin film. To get enough data, three different substrates (SiO_2, glass, glass with roughened backside) together with reflection, as well as

transmission measurements, were performed.

VASE measurements were performed with a Woollam M-2000 ellipsometer in reflection and transmission mode by using different incidence angles. The analysis was performed with the WVASE32 software from Woollam [138].

4.8. UV/vis/NIR absorption spectroscopy

Absorption spectroscopy with ultraviolet (UV), visible (vis) and near-infrared (NIR) light is another method to determine the optical properties of thin films. In general, the transmittance T of light with different wavelengths is measured through an optical sample which can be written as the ratio of incoming and transmitted light. The resulting equation

$$T = \frac{I(d)}{I_0} = \exp(-\alpha d) \tag{4.21}$$

is based on the Lambert-Beer law and includes the absorption coefficient α as well as the thin film thickness d which was measured prior by XRR. The resulting absorption coefficient can then be used to calculate the extinction coefficient k_{xy} in the in-plane direction according to

$$k_{xy} = \frac{\alpha\lambda}{4\pi}, \tag{4.22}$$

where λ is the wavelength of the light that was varied from $200 - 1100$ nm. These values correspond to an energy of $1.1 - 6.1$ eV. The measurements were performed by using a Varian Cary 50 UV-Vis. To minimize errors, a cleaned and empty glass substrate was measured and subtracted as a baseline.

Part III.

Results and discussion

This chapter contains the main part of this thesis, the characterization of organic-inorganic thin films. For a comprehensive understanding of the impact of alkali metal doping or gold deposition on the organic thin film structure, and ergo the optoelectronic properties, it is vital to investigate the pristine samples first. The first section of this chapter is dedicated to the study of the [6]Phenacene thin film structure and morphology. [6]Phenacene was chosen as a material of interest due to its attractivity as a component in organic-organic interfaces [91]. In the following subsections, the in-plane and out-of-plane structures of prepared thin films were investigated using different X-ray diffraction methods. Additionally, the thin film morphology and optical properties were studied employing AFM measurements and a variety of optical methods. These ex-situ measurements were performed in the home laboratory and were necessary to obtain enough data and experience with the sample preparation to perform further in-situ real-time experiments. Therefore, the following subsections were dedicated to the more demanding study of in-situ thin film growth, which demands the use of state-of-the-art high-speed X-ray detectors and X-ray sources with a high flux only found at synchrotrons. In-situ experiments were performed at DESY P03, P23 and ESRF ID10 as well as BM32 covering various X-ray diffraction methods like XRR and GIWAXS.

Once an extensive insight into the pristine thin film behaviour and properties was gained, the same experimental methods to study alkali metal doped [6]Phenacene thin films were applied. The second section of the chapter discusses the alkali metal doping-induced structural and optical changes in prepared thin films and follows a similar structure of subsections as for the pristine thin films. Doping is an important method for altering the properties of thin films and the work was focused on potassium, caesium and rubidium doping. Especially potassium in combination with [5]Phenacene recently attracted focus due to its relevance to superconductivity which has been demonstrated recently [31].

The third section covers gold deposition on [6]Phenacene thin films. Gold is a common material for electrical contacting and therefore very important for optoelectronic devices [54]. This section discusses the metal-induced structural and morphological changes when gold is deposited on top of a [6]Phenacene thin film. Also, the opposite situation is briefly discussed, where [6]Phenacene is deposited on top of gold, which already showed major structural changes in other materials [55].

5. Pure [6]Phenacene thin films

In order to understand organic-inorganic hybrid systems, thin films of pure [6]Phenacene were characterized first. Silicon, glass and roughened glass substrates were prepared according to chapter 4.3. To get an insight into the influence of different growth parameters, thin films of different thicknesses were grown using the OMBD chamber in the home laboratory. Afterwards, all films were characterized by their ex-situ properties using various techniques including XRR, AFM, UV-Vis and ellipsometry. To measure the evolution of structure formation during the deposition of the film, silicon substrates were installed in a small vacuum chamber that was equipped with a beryllium window making in-situ scattering experiments possible. In-situ GIWAXS measurements were performed at DESY P03. Further in-situ XRR data was acquired during a beamtime at ESRF ID10. Parts of this section have been published in Ref. [89].

5.1. Crystal structure

The determination of the crystal structure was performed by X-ray scattering and is divided into the out-of-plane structure, which covers XRR measurements, as well as the in-plane structure which was determined using GIWAXS. In both subsections, the ex-situ measurements of thin films, which were grown in our home lab, are presented first, before focus is given to the in-situ real-time measurements, which were performed at various beamlines.

5.1.1. Out-of-plane structure

Figure 5.1 shows XRR of a series of [6]Phenacene thin films with different thicknesses prepared at identical growth conditions. The substrate temperature during the growth was kept at a room temperature of 297 K. All prepared [6]Phenacene thin films show well-developed out-of-plane stacking as concluded from the presence of well-defined (002) and (004) Bragg reflections. Altering the thickness leads to changes in the roughness as well as the Bragg peak width and position.

Further analysis was performed by using the software GenX [113] to calculate the film thickness as well as the roughness. The (002) Bragg peak was fitted with a Gaussian to

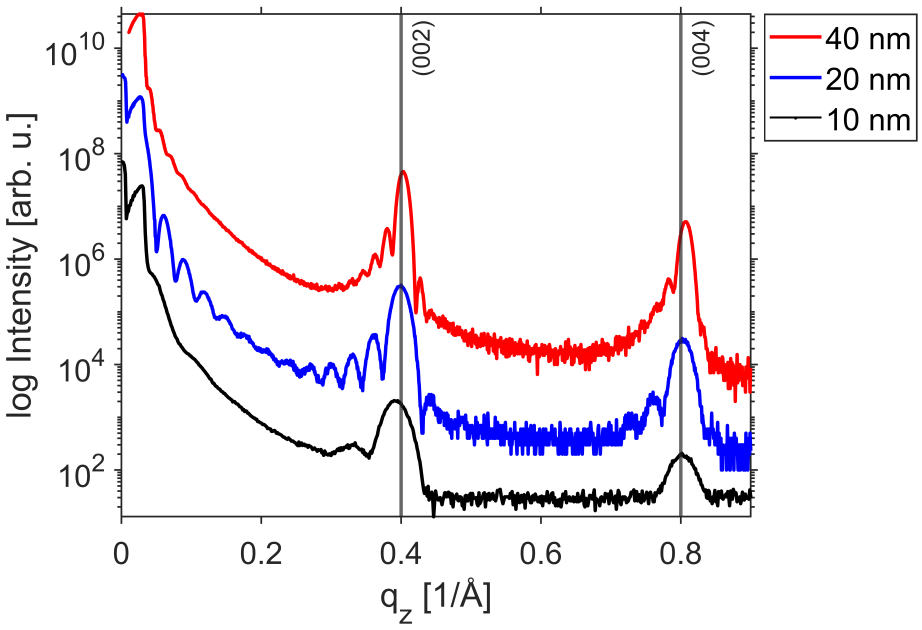

Figure 5.1.: XRR data of pure [6]Phenacene with thicknesses of 10, 20 and 40 nm. The grey vertical lines indicate the (002) and (004) Bragg reflections as determined from the film with the 20 nm thickness. The intensity in this and the following reflectivity figures are plotted in a logarithmic scale.

calculate the peak position, FWHM as well as the lattice parameter using Equation 4.11. The results of the calculation and peak fitting can be found in Table 5.1.

Table 5.1.: Film parameters derived from XRR measurements of pure [6]Phenacene thin films. The thickness and roughness was calculated with GenX. The other data was calculated from the (002) Bragg reflection.

Thickness [nm]	Roughness [nm]	q_{Bragg} [1/Å]	FWHM [1/Å]	Lattice parameter [Å]
9	1.55	0.384	0.039	32.76
21	2.16	0.399	0.023	31.49
36	4.22	0.403	0.013	31.18

The calculated thickness is shown in the first row and shows a slight variation of ±1 nm for the thinner two films which can be explained due to rate instabilities of the Knudsen cell during the deposition combined with the error rate of the QCM (around 10%) that was used to check the current thickness. Especially long deposition times can lead to a higher difference which can be seen in the third 36 nm film. The calculated thin film surface roughness shows a strong thickness dependence. For the 9 nm thick sample, the surface is relatively smooth. However, with the increasing thickness of the thin film, the roughness also increases. This suggests the formation of islands rather than layer-by-layer growth. The position of the observed Bragg reflections, and therefore, the lattice parameter, also

changes with the film thickness. This is most likely caused by a formation of a transient structure in the thin film [59]. This interaction apparently only affects the first monolayer, and therefore the change in peak position is only significant for very thin film samples, as there is practically no difference between the 21 nm and 36 nm thick samples. Finally, changes in FWHM can be correlated to grain size, as described by the Scherrer equation [139], as well as a degree of molecular ordering. In our case, the FWHM of the observed Bragg peaks decreases with increasing thin film thickness, as the individual out-of-plane domains are getting larger during the growth. Overall, the observed Bragg reflections are very narrow, indicating a high degree of ordering in an out-of-plane direction.

To properly study the [6]Phenacene thin film growth process from the very early stages of deposition, in-situ XRR measurements at ESRF ID10 were performed. At the beginning of the deposition, there is only a small amount of material on the substrate. The high photon flux of modern synchrotrons achieves a sufficiently high signal to study these early stages of thin film growth. Figure 5.2 shows the in-situ real-time XRR image of [6]Phenacene grown at a deposition rate of 2 Å/min and at room temperature until a final thickness of 20 nm.

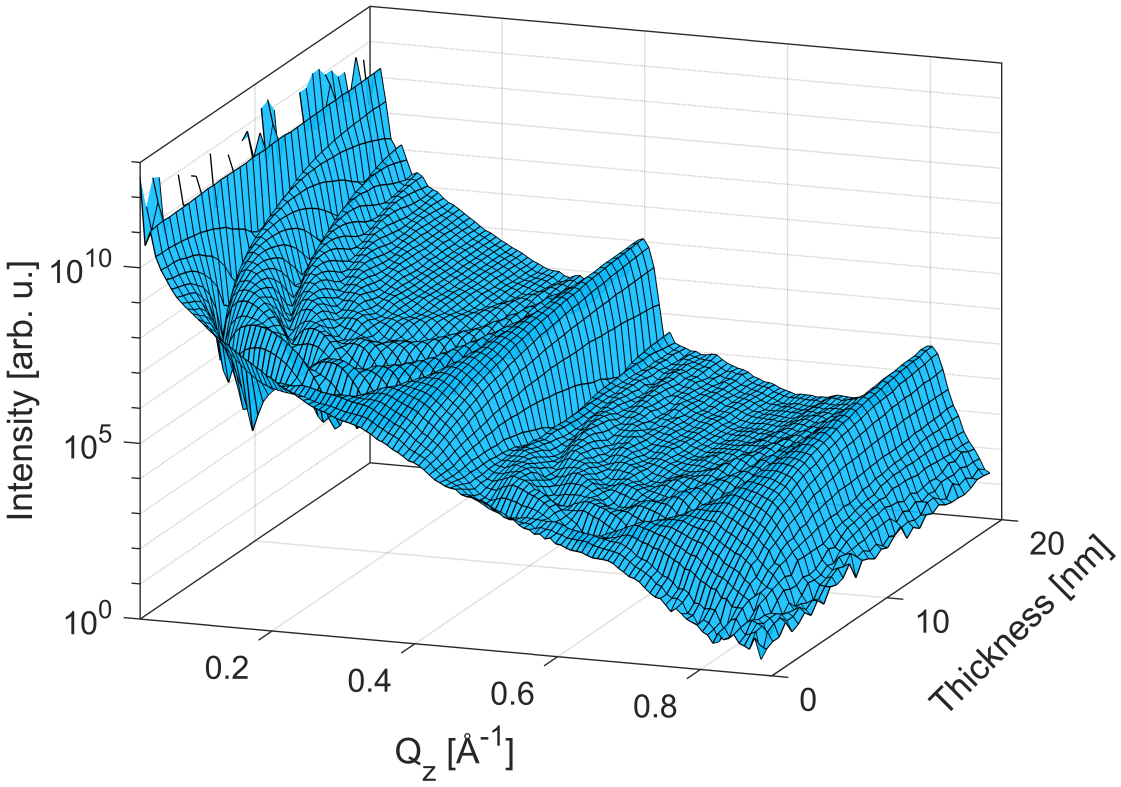

Figure 5.2.: In-situ XRR measurement of the growth of a pure [6]Phenacene thin film.

The 3D plot shows a smooth film phase for the first 10 nm and increased roughening afterwards. The (002) and (004) Bragg peaks are also visible after several nm and are getting

more pronounced with increasing thickness. The roughness and the lattice parameter were calculated using the same method as above. Both values were plotted and are shown in Figures 5.3. They will be discussed in the next paragraph.

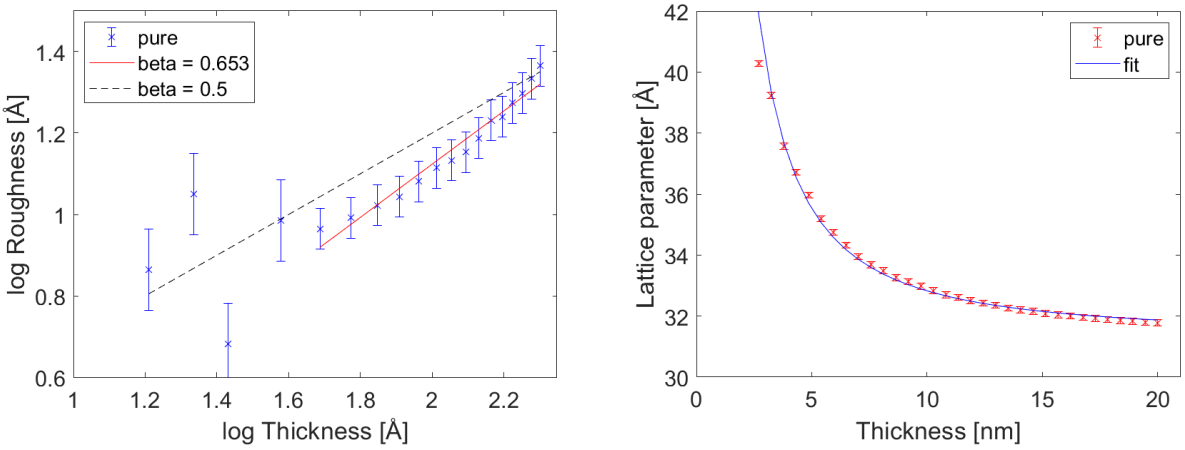

Figure 5.3.: Data of the pure [6]Phenacene thin film: a) roughness calculated with GenX and b) lattice parameter calculated with the [6]Phenacene (002) Bragg peak.

Figure 5.3a shows the [6]Phenacene surface roughness evolution with increasing film thickness. The data can be fit by a linear function inside a logarithmic plot with the slope $\beta = 0.65$. It is slightly above $\beta = 0.5$ which is the random deposition limit. This can be an indication for mild rapid roughening [140, 141]. The initial smooth stage is followed by a gradual increase of surface roughness during the thin film growth, which is an indication of the Stranski-Krastanov growth regime [27]. Figure 5.3b shows the evolution in the lattice parameter, calculated from the Bragg peak position, with increasing thickness of the [6]Phenacene thin film. A sharp decrease in the lattice parameter during the initial stages of the thin film growth was observed. It was fitted successfully with the function $1/(x^{1.5}a) + b$ and the fit parameter $a = 46.7$ and $b = 31.35$. The resulting fit is also shown in Figure 5.3b. As mentioned earlier, at the start of the deposition, deposited [6]Phenacene molecules mainly interact with the substrate. This interaction guides the molecules to crystalize in a slightly different configuration than the one expected for the bulk phase. After the first few monolayers are fully formed, the substrate interaction is surpassed by intermolecular interaction and therefore the unit cell changes. This new configuration does not change with increasing thickness as seen in Figure 5.3b, where after 15 nm, the lattice parameter is almost constant at a final value of 31.78 Å.

5.1.2. In-plane structure

The in-plane structure of a 20 nm [6]Phenacene thin film deposited onto a Si/SiO_2 substrate by OMBD was determined by GIWAXS measurements. Figure 5.4a shows the resulting reciprocal space map which shows several pronounced Bragg reflections resulting from a well-ordered thin film structure. At $q_{xy} \approx 0$ a series of (00l) reflections along q_z, partially hidden by a missing wedge [121], arises from the ordered stacking of molecules in a direction perpendicular to the substrate surface. The number of Bragg reflections with non-zero h and k Miller indices suggests a good ordering of thin film even in the plane. A high degree of molecular ordering in both in-plane and out-of-plane directions is beneficial to achieve a high charge carrier transport in organic FETs. From the positions of the Bragg reflections in the reciprocal space map, the unit cell parameters can be deduced. [6]Phenacene molecules nucleate in a monoclinic structure with the unit cell parameters: $a = 8.4$ Å, $b = 6.2$ Å, $c = 32$ Å and $\beta = 98°$. The long c axis of the unit cell is oriented almost perpendicular to the substrate surface, implying a standing-up configuration of molecules in the thin film. This configuration is commonly observed in cases where molecule-substrate interactions are weak compared to molecule-molecule interactions. The positions of the Bragg reflections that correspond to the calculated unit cell structure are also marked in the reciprocal space map (Figure 5.4a) as black crosses. There is a good agreement between the experimentally measured and calculated positions, confirming the determined unit cell structure. When the results are compared with the already published structure of [4]Phenacene [87], almost identical a and b unit cell parameters are observed, i.e. a very similar packaging is projected in the in-plane direction. The difference in the c parameter and angle β can be explained by the [6]Phenacene molecule having two extra benzene rings and therefore a longer conjugated core.

Figure 5.5 shows the molecular packing of [6]Phenacene inside the unit cell. The comparison in Figure 5.4b between experimentally measured Bragg peak intensities and the ones calculated from determined molecular packing using structure factor equation shows a good agreement. Each unit cell contains four molecules packed in a herringbone structure. Herringbone packing is characteristic for its tilted edge-to-face configuration. In the case of [6]Phenacene, neighbouring molecules are rotated 63° with respect to each other. This configuration then mediates a two-dimensional (2D) charge carrier transport resulting in high field-effect mobility of organic FETs [142].

During our [6]Phenacene study the unit cell results showed a similarity to other phenacene molecules. It was noticed that apparently, the molecular stacking depends on the parity of the conjugated core. Therefore structural data for [7]Phenacene for which the parity changes from even to odd compared to [6]Phenacene was investigated additionally. The reciprocal space map of a 20 nm thin film of [7]Phenacene in Figure 5.6a shows fewer Bragg reflections

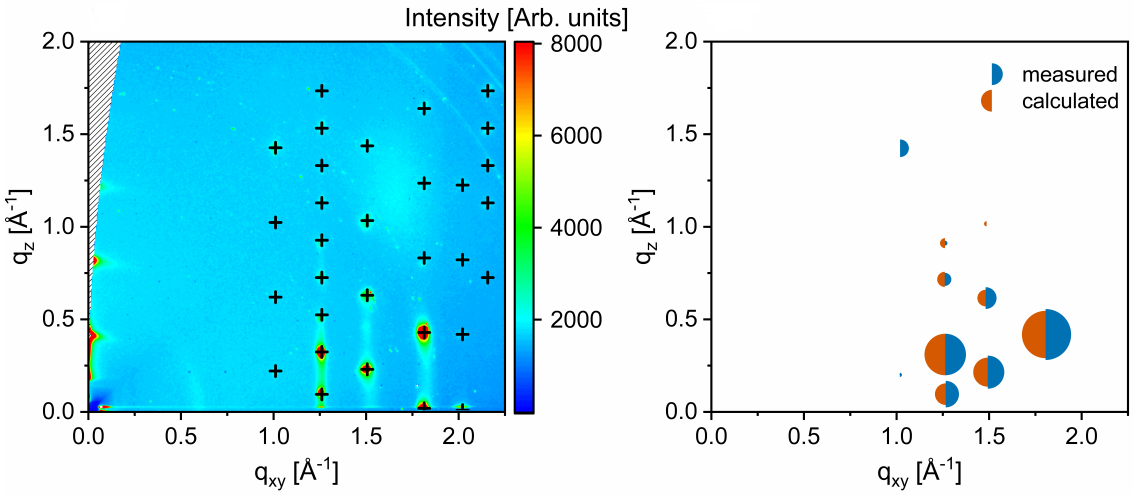

(a) (b)

Figure 5.4.: Reciprocal space map from [6]Phenacene taken from Ref. [89]: a) GIWAXS pattern and calculated peaks and b) comparison of measured and calculated Bragg peak intensities. The area of each circle corresponds to the peak intensity.

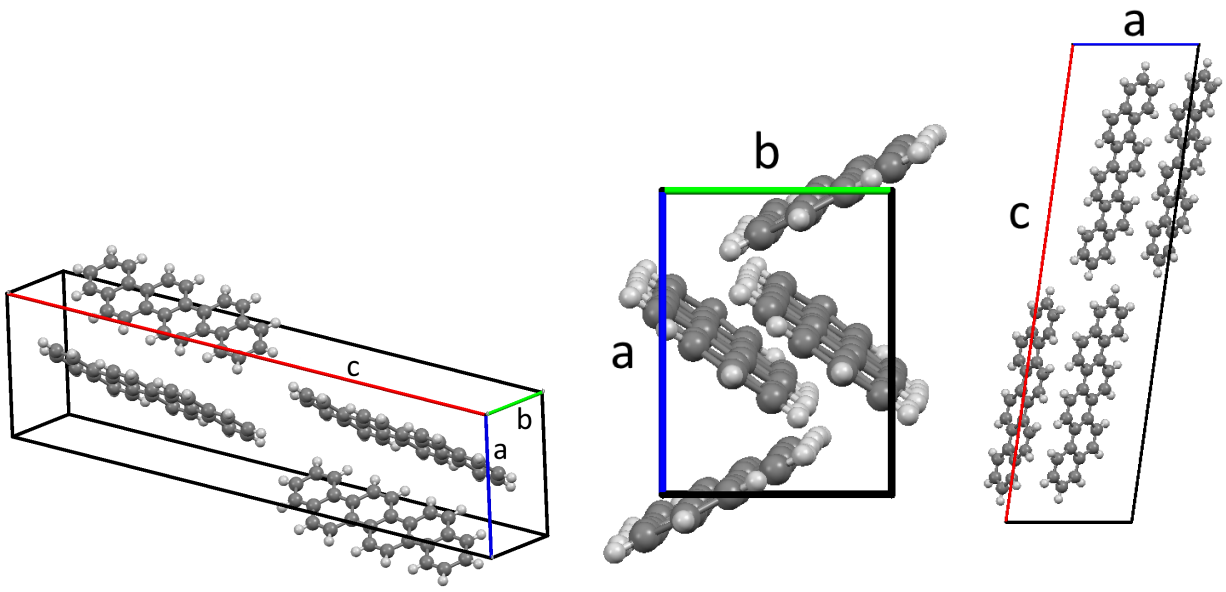

(a) (b) (c)

Figure 5.5.: Unit cell orientation of [6]Phenacene taken from Ref. [89]: a) side view b) *ab*-plane perpendicular to the substrate surface and c) *ac*-plane parallel to the substrate surface.

when compared to the thin film of [6]Phenacene. While a series of Bragg reflections in the q_z direction suggests a well-ordered structure in the direction perpendicular to the substrate, the degree of in-plane ordering is relatively low. The Bragg reflections are broader compared to the [6]Phenacene film, hinting at an overall less organized structure. The evaluation of unit cell parameters from the reciprocal space map reveals two sets of Bragg peaks belonging to two distinct crystallographic structures. While the in-plane structure is relatively similar for both structures, one polymorph, the H-polymorph (see Ref. [90]), has its peaks at slightly higher q_{xy} values than the L-polymorph. The overlap of Bragg reflection resulting from such a similar structure, at least partially explains the observed peak broadening. The H-polymorph has a unit cell structure of $a = 8.24$ Å, $b = 6.22$ Å, $c = 36.64$ Å and $\beta = 89.64°$ while the L-polymorph shows a similar unit cell of $a = 8.51$ Å, $b = 6.15$ Å, $c = 18.34$ Å and $\beta = 93.06°$. Both observed structures are monoclinic with very similar a and b unit cell parameters while the angle β is different between polymorphs. Interestingly, the c unit cell parameter is doubled for the H-polymorph, effectively doubling the volume and therefore also the number of molecules per unit cell. Black and red crosses in Figure 5.6a indicate theoretically calculated positions of experimentally observed Bragg reflections resulting from the H- and L-polymorph, respectively. From their positions, it is possible to determine the orientation of the unit cell with respect to the substrate. As expected, both polymorphs grow in a standing-up configuration on a Si/SiO_2 substrate, which means that the a and b axis is parallel to the substrate surface, see Fig. 5.7.

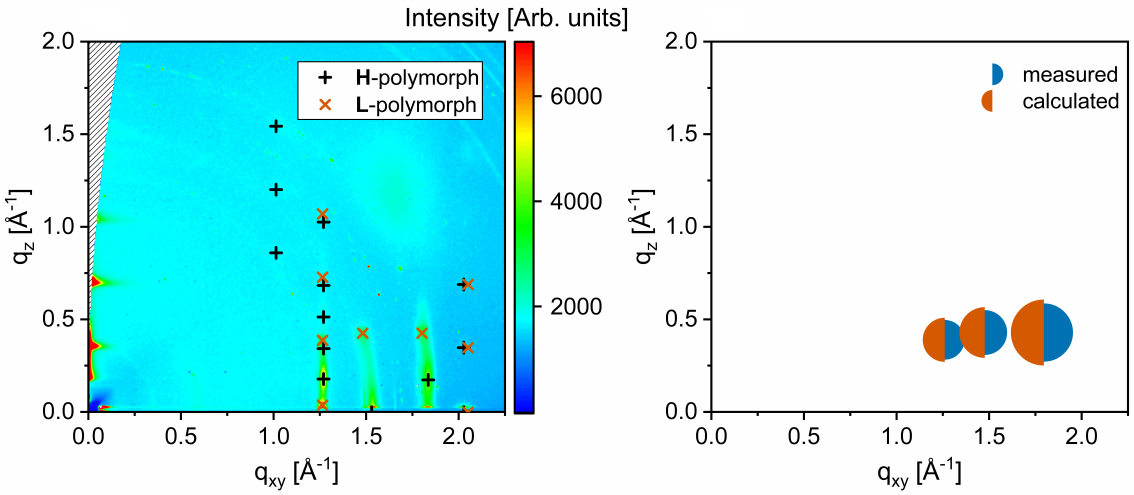

(a) (b)

Figure 5.6.: Reciprocal space map of [7]Phenacene taken from Ref. [89]: a) GIWAXS pattern and calculated Bragg peak comparison and b) comparison of measured and calculated peak intensities of the L-polymorph. The area of each circle corresponds to the peak intensity.

The [7]Phenacene structure shows similarities to the already published structure of [5]Phenacene [88], which has the same parity. The unit cell parameters are comparable to our L-polymorph, the only differences being the length c and angle β. Similarly to [6]Phenacene, this is caused by molecular length variation of [5] and [7]Phenacene. However, the observed H-polymorph structure is clearly different. A similar observation of two distinct polymorphs for [5]Phenacene has been in Ref [90]. For [5]Phenacene the polymorph distribution is thickness-dependent, where the initial layers close to the substrate nucleate in the H-polymorph, followed by L-polymorph growth after ∼8 nm. In this case, the same growth behaviour for [7]Phenacene thin film growth is observed. A possible explanation for the coexistence of two distinct polymorphs is proposed by Hayakawa et al. [143]. To reduce the high surface energy of SiO_2 interface, a high-density packing of [7]Phenacene molecules induces stress on a unit cell. Observed stress is compressive and in an in-plane direction, causing a slight shift of q_{xy} Bragg reflection positions for the H-polymorph. After sufficient strain relaxation with an increase in film thickness, the formation of an L-polymorph is energetically favoured. The molecular packing of the [7]Phenacene L-polymorph was calculated only, as there are not enough clearly visible Bragg reflections for the H-polymorph to be fitted properly. Some peaks overlap between polymorphs and the overall number of observed reflections is much lower than for [6]Phenacene. Nonetheless, an approximation of the molecular packing for the L-polymorph based on a subset of peaks with sufficient intensity is provided. Figure 5.7 shows the molecular packing of the [7]Phenacene L-polymorph. Each unit cell contains two [7]Phenacene molecules in an edge-to-core configuration, creating a herringbone packing motif.

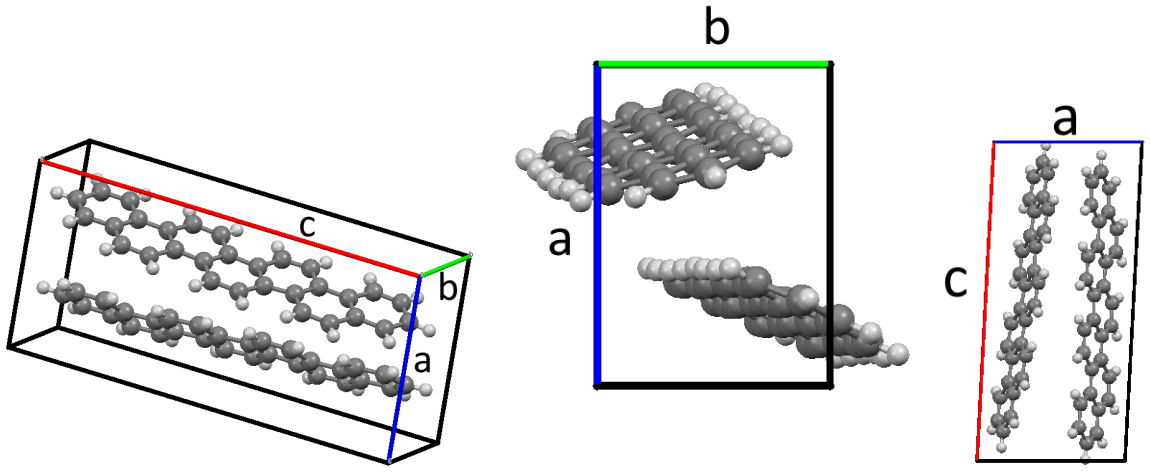

(a) (b) (c)

Figure 5.7.: Unit cell of [7]Phenacene taken from Ref. [89]: a) side view b) *ab*-plane perpendicular to the substrate surface and c) *ac*-plane parallel to the substrate surface.

A comparison of both molecules shows that [6]Phenacene has a higher crystallinity than [7]Phenacene which is usually favourable for better charge carrier transport [144, 145]. To achieve a better crystallinity or to change other device aspects, various methods like doping [146] or post-growth annealing [147] can be utilised. The doping method has been applied in the next chapter. In general, both molecules exhibit a standing-up configuration and show similarities in the unit cell compared to [4]Phenacene and [5]Phenacene.

To study the process of thin film growth, in-situ GIWAXS measurements were conducted to track the reflection positions during thin film growth. [6]Phenacene was deposited onto a Si/SiO_2 substrate while acquiring a reciprocal space map every 10 seconds. The final GIWAXS pattern after deposition is shown in Figure 5.8a. A series of integrated linecuts in reciprocal space was extracted and subsequently fitted with a Gaussian to determine the position of each visible Bragg reflection. The positions were tracked in the q_z and q_{xy} direction for each acquired frame during thin film growth. As an example, the (111) Bragg reflection is shown in Figure 5.8b.

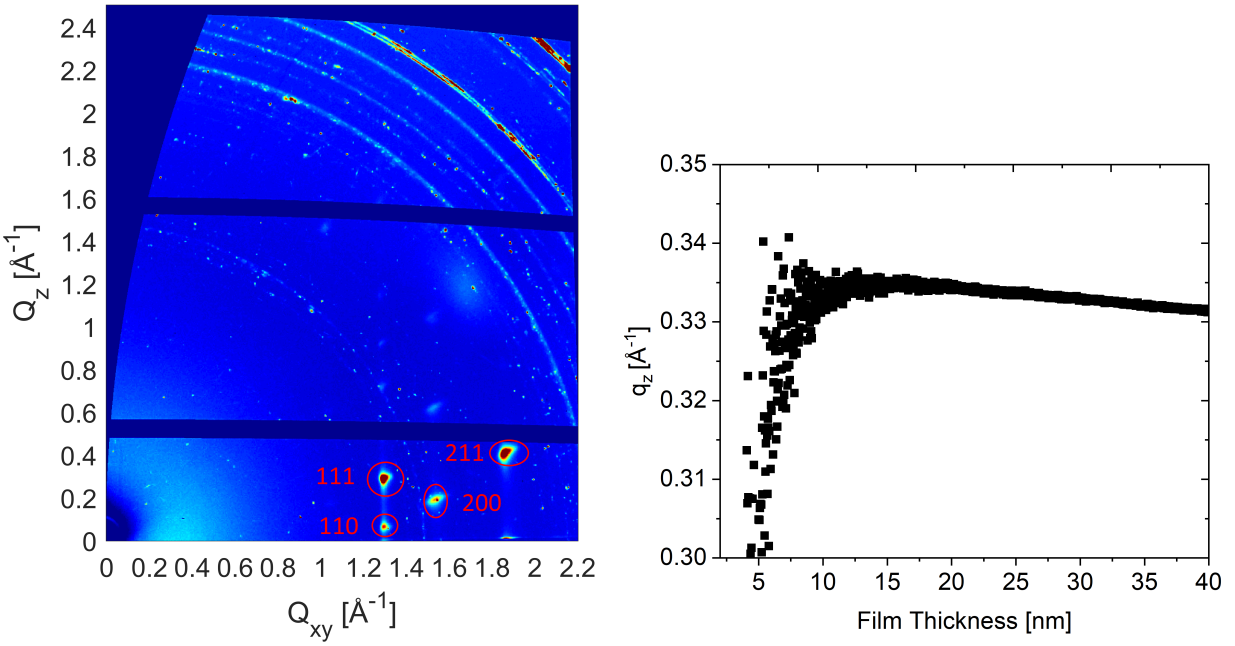

(a) (b)

Figure 5.8.: 40 nm of [6]Phenacene: a) reciprocal space map b) evolution of the (111) Bragg peak during growth.

From the positions of all observed Bragg reflections it was possible to calculate the full set of unit cell parameters as described in subsection 4.4.4.1. Figure 5.9 shows the evolution of the unit cell parameters with increasing thickness during the deposition.

A significant change of the c unit cell parameter is observed, while a and b stay constant during the entire growth. A similar behaviour was already observed in the lattice parameter of the XRR data. Additionally, a small change in the angle β was observed while the rest

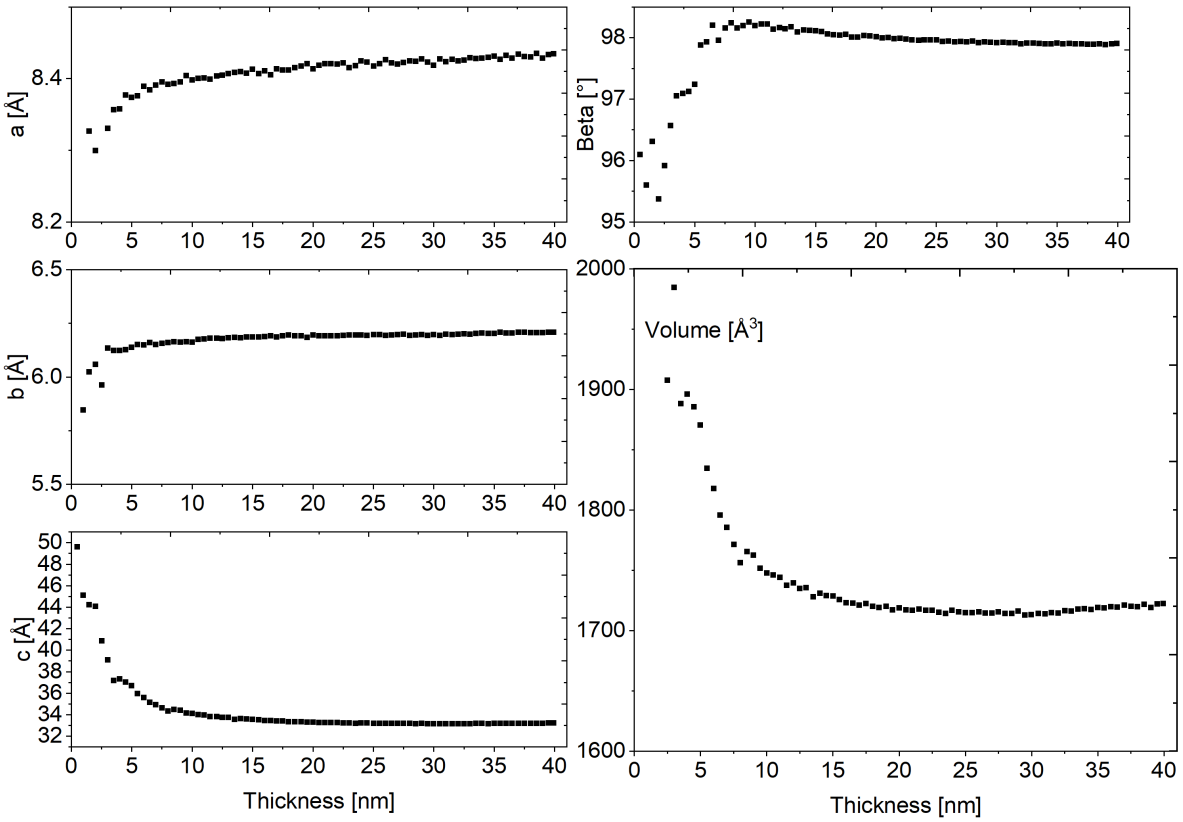

Figure 5.9.: Measured changes in the unit cell parameters during [6]Phenacene deposition.

of the angles stay constant at 90 degrees. It is important to note that the determination of the unit cell parameters for films with a thickness below 10 nm is not as high as for larger films. This is due to Bragg reflections with a very low intensity that are needed to calculate the unit cell parameters, resulting in inaccuracy in peak position fitting. From the unit cell parameters, it is possible to calculate the unit cell volume and track its change during deposition. Figure 5.9 shows a significant change in the unit cell volume during the early stages of thin film growth. As discussed before, at the start of the thin film growth, the interaction between molecule-molecule and molecule-substrate is different for the first monolayer. The difference is caused by the interaction between deposited molecules and the substrate. After the first few monolayers, the interaction is suppressed by intermolecular interactions and the thin film structure changes. The observed change in the unit cell volume is attributed to the change of the orientation of [6]Phenacene molecules inside the unit cell, as they are adapting to the energetically more favourable configuration.

5.2. Morphology

AFM was used to gain insight into the surface morphology of [6]Phenacene thin films. Figure 5.10 shows an overview of the conducted measurements which cover the same $10 - 40$ nm thick films as investigated in Subsection 5.1.1.

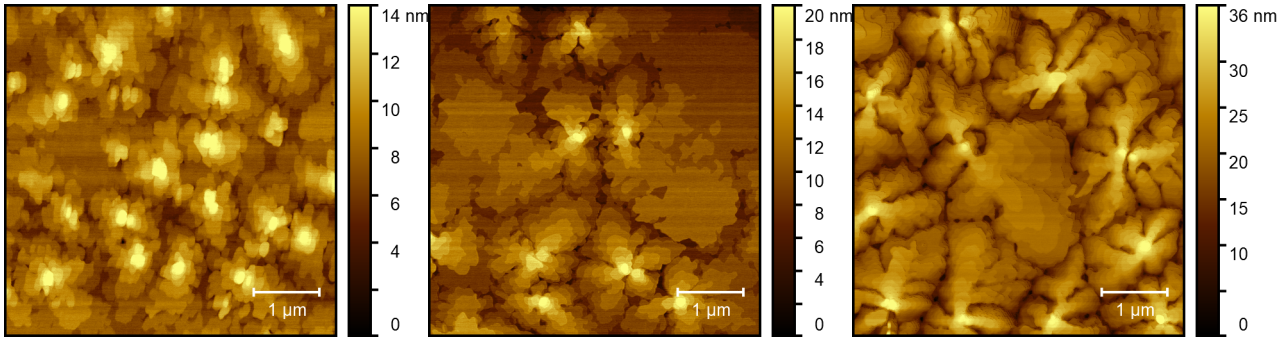

(a) (b) (c)

Figure 5.10.: AFM images (5 x 5 µm) of pure [6]Phenacene films grown at 2Å/min and room temperature: a) 10 nm, b) 20 nm and c) 40 nm.

Figure 5.10 shows [6]Phenacene thin films forming islands with the wedding cake structure. With increasing thickness the number of terraces per area increases, while the number of islands stays constant. The RMS roughness was extracted with Gwyddion from all prepared thin films by using the entire image. The results are shown in Figure 5.11, which compares the results with the XRR measurements.

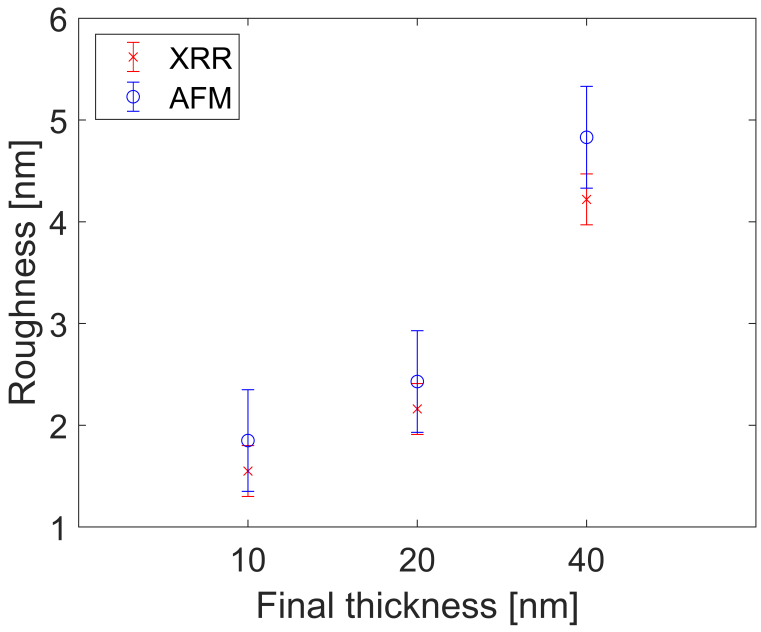

Figure 5.11.: Roughness comparison between XRR and AFM.

Both XRR and AFM show the same trend in surface roughness evolution with increasing thickness of the [6]Phenacene thin film. It has to be mentioned that AFM measurements were only covering a 5×5 µm^2 area while XRR gives information from a much larger area and therefore a much better statistical average of surface roughness. This fact was taken into account in the respective error bars. By taking a look at the wedding cake structure, planar terraces with well-defined edges can be seen. Linecuts of these terraces were made along the step edges (as shown in Figure 5.12a) to determine the height difference.

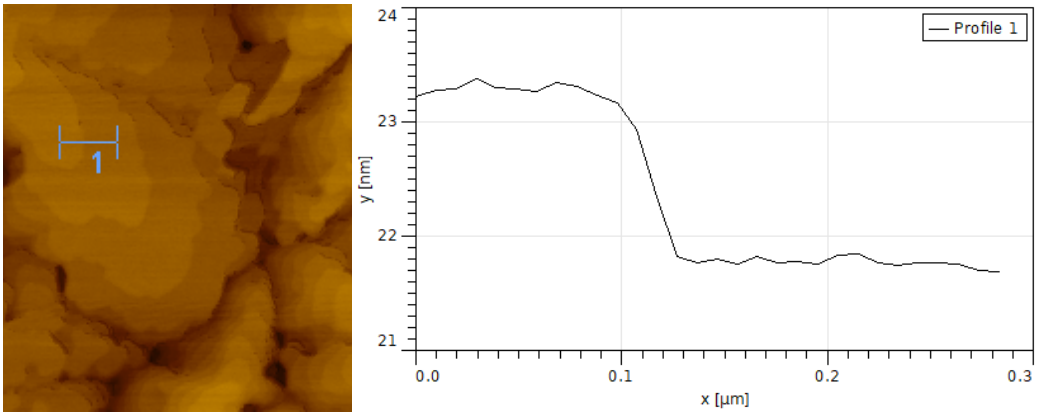

(a) (b)

Figure 5.12.: Sample AFM linecut of Figure 5.10c: a) linecut of a [6]Phenacene terrace and b) corresponding height profile.

The average step height is 1.51 nm, which approximately corresponds to the length of one [6]Phenacene molecule. The transitions between terraces are very well-defined and sharp, therefore it is expected that the slope between two terraces in the linecut (Figure 5.12b) is caused by the width of the AFM probing tip. From the GIWAXS data mentioned previously and the calculation of the molecular orientation of the unit cell, it can be depicted that the [6]Phenacene molecules grow in a standing-up configuration with their long molecular axis almost perpendicular to the surface of the substrate. Therefore, each terrace consists of one monolayer of [6]Phenacene molecules.

5.3. UV/vis/NIR spectroscopy and ellipsometry

The optical properties were studied using ultraviolet-visible-near-infrared (UV/vis/NIR) absorption spectroscopy as well as variable-angle spectroscopic ellipsometry (VASE). Figure 5.13 shows the UV/vis/NIR absorption spectra with the extinction coefficient k of pure [6]Phenacene thin films corrected to their measured final thickness of 10 and 20 nm. The optical properties will not change with the thin film thickness, but due to differences in the thin film preparation, the intensity of both films shows slight differences. The first peak

at 3.17 eV is identical to the first transition from $S_0 \rightarrow S_1$ [84]. Followed by two sharp peaks at 3.37 and 3.51 eV and a broad peak at 4.15 eV [81]. These [6]Phenacene thin film absorption spectra show similarity to the solution spectra [148]. The first three peaks have an equidistant energy spacing of 0.17 eV which is a sign for a vibronic progression [149–151].

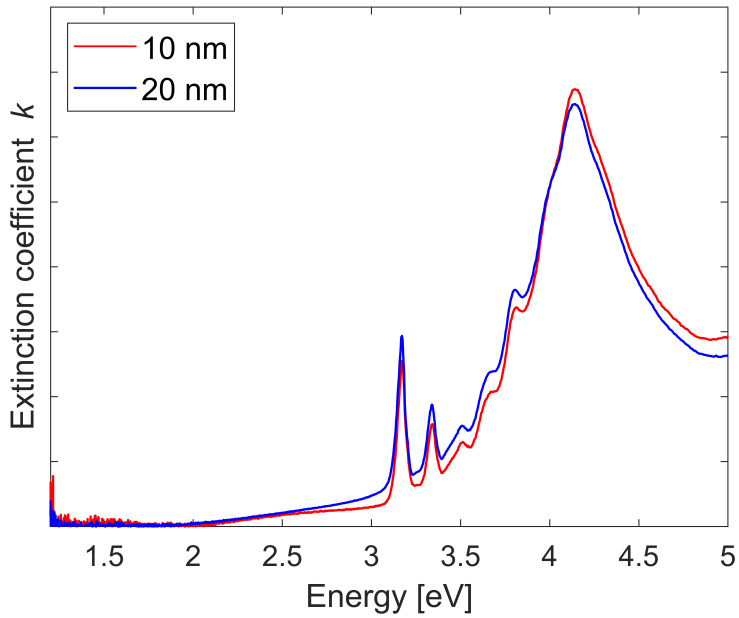

Figure 5.13.: UV/vis/NIR absorption spectra of pure [6]Phenacene thin films with different thicknesses.

Organic molecules with an asymmetric molecular structure often exhibit strong anisotropy in their optical properties [152]. This is also expected for crystalline [6]Phenacene due to the rod-like shape of its molecular entity. As previously shown, the [6]Phenacene molecules on an inert surface like glass or silicon are oriented in a standing-up configuration, therefore the whole thin film exhibits different optical properties depending on the direction of incoming light. This effect was investigated using VASE. Figure 5.14 shows the energy dependence of in-plane and out-of-plane extinction coefficient components. The raw data can be found in the Appendixes in Figure 9.2. The strength of the observed optical transitions above 3.3 eV is strongly dependent on the direction of the incoming light. The dominant k_z component indicates that the transition dipole moment is oriented perpendicular to the substrate surface, which is in the direction of the long molecular axis of [6]Phenacene.

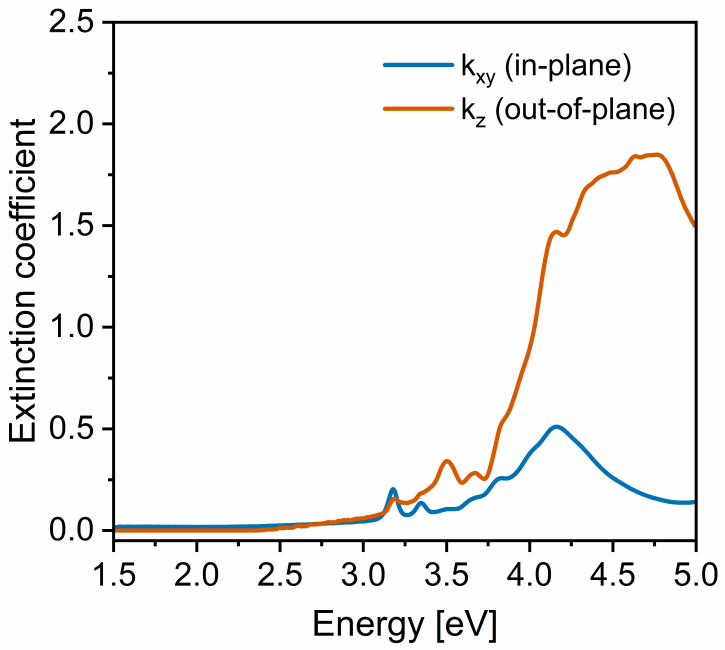

Figure 5.14.: VASE data of pure [6]Phenacene thin films. Taken from Ref. [89].

5.4. Discussion

The crystal structure and morphology of [6]Phenacene thin films grown on native silicon substrates were investigated using real-time XRR and GIWAXS measurements during a deposition. The results were supplemented with AFM and optical measurements.

The presence of well-defined (002) and (004) Bragg reflections in the XRR data together with a thickness-dependent roughness indicates a mild rapid roughening with increasing thickness. The (002) Bragg peak width and position showed a sharp decrease of the lattice parameter during the initial stages of growth. AFM images indicate a wedding cake structure with a well-defined and sharp transition between the terraces [153, 154]. The average step height corresponded to the length of one [6]Phenacene molecule, therefore each terrace consists of approximately one monolayer of [6]Phenacene molecules in a standing-up configuration. Thickness-dependent morphology changes were mainly observed for the number of terraces that increased with the thickness.

By combining the data from XRR and AFM measurements, the growth regime of [6]Phenacene thin films can be determined. Based on XRR data, the Stranski-Krastanov growth regime was suspected. The analysis of the surface morphology together with the surface roughness evolution from AFM imaging supports this initial presumption. Based on kinetic Monte Carlo simulations performed by Empting et al. [70], the Stranski-Krastanov growth regime is characterized by an initial surface roughness oscillation at the start of the thin film deposition followed by a monotonic increase in surface roughness. The change

in surface roughness evolution is caused by switching from 2D layer-by-layer growth after a critical thickness is achieved to a 3D island formation. Figure 5.3a indicates that the initial smooth stage of [6]Phenacene thin film growth has large error bars and is followed by a gradual roughening which is expressed by the linear fit. This change in the surface roughness evolution trend happens at the thin film thickness of roughly $3.5 - 4$ nm. This approximately corresponds to the length of two [6]Phenacene molecules. Therefore, it can be concluded that the critical thickness is two monolayers. After that, additional deposited molecules form islands that grow mainly in height, increasing the surface roughness. The oscillation of the surface roughness at the early stages of thin film growth, expected based on calculations from Empting et al., is not visible in our XRR data [70]. The reason for this is a combination of relatively large error bars and a limited number of data points, caused by low Bragg peaks intensity at the initial stages of the thin film deposition. A schematic representation of the [6]Phenacene thin film growth is shown in Figure 5.15.

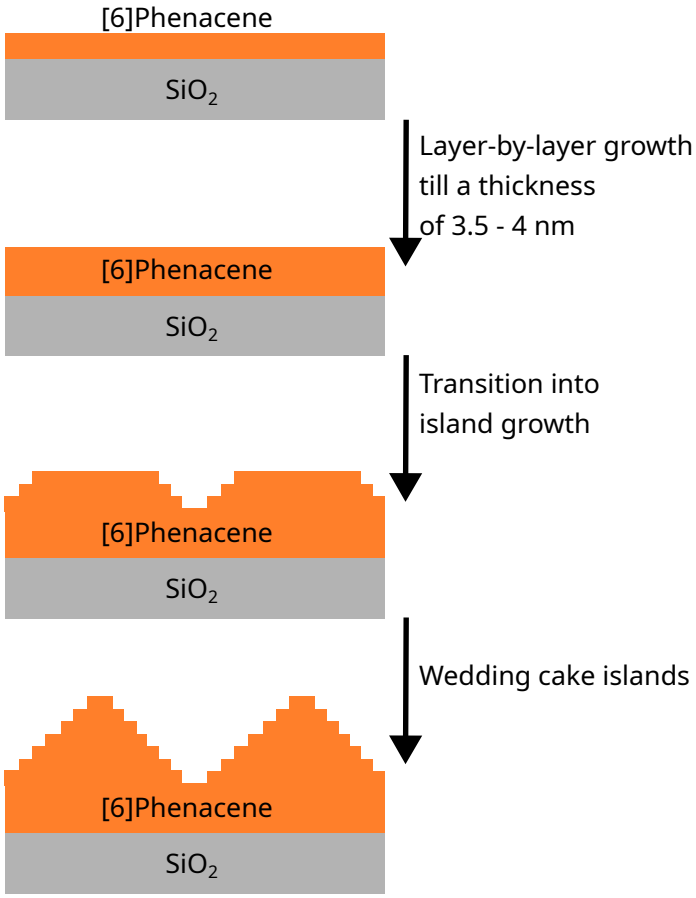

Figure 5.15.: Overview of [6]Phenacene thin film growth. Growth begins with layer-by-layer growth. After a certain thickness, it transitions to island growth. This growth mode is called Stranski-Krastanov growth. The resulting islands are called wedding cake islands.

The unit cell structure and orientation of [6]Phenacene was calculated using reciprocal space maps from GIWAXS measurements [89]. Based on the calculated unit cell volume, a unit cell with four molecules was used. The molecular packing of [6]Phenacene showed a standing-up configuration with a herringbone structure that is characteristic for its tilted edge-to-face configuration and is important for high field-effect mobilities of OFETs [142]. The results showed similarities to other previously investigated phenacene molecules with the same even parity, therefore additional data of [7]Phenacene that had an odd parity, was also investigated with this method. [7]Phenacene shows two polymorphs with a standing-up configuration. The unit cell structure of both polymorphs was calculated. However, due to the broader and lower amount of Bragg reflections, it was only possible to calculate the molecular packing of the L-polymorph. The comparison of both molecules showed that [6]Phenacene has a higher crystallinity than [7]Phenacene which is usually favourable for a better charge-carrier transport [144, 145]. A representation of the molecular packing of both molecules is shown in Figure 5.16. Additional in-situ GIWAXS measurements of [6]Phenacene concluded the data.

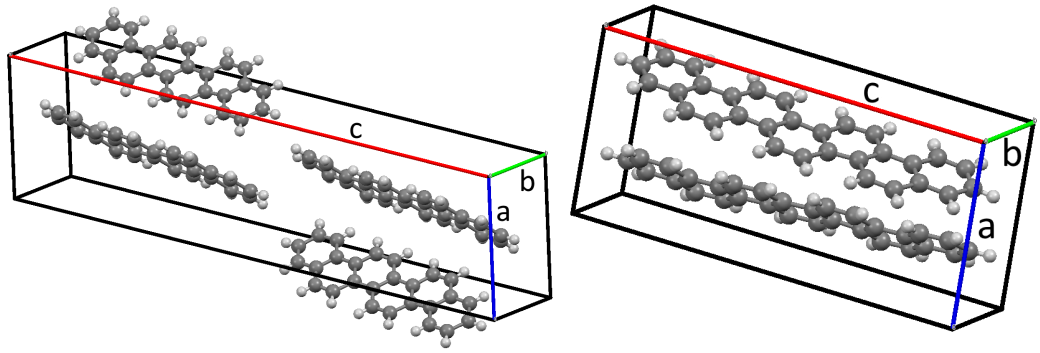

(a) (b)

Figure 5.16.: Unit cell side view of different phenacenes taken from Ref. [89]: a) [6]Phenacene and b) [7]Phenacene L-polymorph.

The optical measurements of [6]Phenacene showed the first $S_0 \rightarrow S_1$ transition as well as an equidistant energy spacing of 0.17 eV for the first three peaks, which is a sign for a vibronic progression in organic molecules with a conjugated core backbone [149, 151]. Due to the herringbone structure of [6]Phenacene with its edge-to-face configuration, an impact on the optical properties depending on the molecular orientation was expected. Therefore, this effect was investigated using VASE measurements, showing a strong dependency of the direction of incoming light with a dominant k_z component.

The results of this chapter showed the crystal structure and morphology of [6]Phenacene. It is important that the orientation of the thin film with respect to the incoming light has to be considered for any possible applications of [6]Phenacene thin films in organic

photovoltaics. Similar behaviour can be found in polymers [155]. [6]Phenacene is, therefore, more common in OFETs [80, 83, 156]. For organic solar cell applications, it would be more suitable if the in-plane component would be dominant in this specific case due to the incoming light from above [157, 158]. Finally, the study of pure [6]Phenacene thin films is the first step in the investigation of doping-induced changes in a thin film structure, presented in the next chapters.

6. Alkali metal doped [6]Phenacene thin films

The first organic-inorganic hybrid system of this study to be characterized was [6]Phenacene together with either potassium, rubidium or caesium. Silicon and glass substrates were prepared according to Section 4.3 and an alkali dispenser cell as described in Section 3.3 was mounted in a small vacuum chamber. The deposition was performed using two different procedures. Thin films of pure [6]Phenacene with a deposition rate of 2 Å/min and a final thickness of 20 nm were grown. Afterwards, alkali metals were deposited on top of it for 30 minutes. These films are called "top" in the sections below. The second method was growing thin films of [6]Phenacene together with alkali metals by simultaneous deposition using the same deposition rate and time as above for the pure films. These films are called "co" in the sections below. To increase reproducibility each alkali metal dispenser was replaced by a fresh one after doing a "top" and "co" deposition. Afterwards, all films have been taken out and measured with various techniques including XRR, GIWAXS, AFM, SEM and UV/vis/NIR spectroscopy. Additionally, XPS was used to estimate the ratio between [6]Phenacene and alkali metals. To measure the structural evolution during [6]Phenacene deposition together with alkali metals, in-situ experiments were performed. Therefore silicon substrates were installed in a small vacuum chamber that was equipped with a beryllium window as well as deposition cells for organic molecules and alkali metals. In-situ GIWAXS and XRR measurements were performed at ESRF ID10. Further measurements with a focus on rubidium as the alkali metal were performed at DESY P23, which allowed us to perform in-situ XRR measurements at different X-ray energies below and above the total reflection edge of rubidium. Parts of this section have been published in Ref. [89].

6.1. Crystal structure

The determination of the crystal structure was performed by X-ray scattering and is divided into the out-of-plane and the in-plane structure similar to subsection 5.1.

6.1.1. Out-of-plane structure

Figure 6.1 shows XRR data of several [6]Phenacene thin films that are either pure, doped with alkali metals on top or have been co-deposited together with alkali metals (co). Figure 6.1a shows the q_z interval that covers the range from the total reflection edge up to the second Bragg reflection. Figure 6.1b shows a more detailed view of the total reflection edge and the Kiessig oscillations while Figure 6.1c shows the q_z range up to the silicon (111) reflection. The comparison between the pure and the on-top thin film reveals, that the out-of-plane crystal structure of [6]Phenacene stays intact after the deposition of the alkali metals. This can be concluded from the strong similarity in the XRR scans with only minor changes in the position of the first two Bragg reflections. However, co-deposition shows more drastic changes, as Bragg reflections vanished, got broader or slightly shifted in the q_z position. The high q_z range shown in Figure 6.1c shows the loss of Bragg reflections for nearly all alkali co-deposited thin films.

Further analysis was performed by using the software GenX [113] to calculate the roughness. Due to the changed internal structure of the thin films, the fitting model reached its limits and therefore a higher error value of the calculated roughness has to be expected. The first (002) Bragg peak was fitted with a Gaussian distribution function to calculate the peak position, FWHM as well as the lattice parameter using Equation 4.11. The results are shown in Table 6.1.

Table 6.1.: Film parameters derived from XRR measurements of alkali metal doped [6]Phenacene thin films.

Film	Roughness [nm]	q_{Bragg} [1/Å]	FWHM [1/Å]	Lattice parameter [Å]
Pure	4.00	0.400	0.020	31.34
K top	2.78	0.397	0.028	31.69
K co	1.90	0.383	0.107	32.84
Rb top	3.86	0.395	0.019	31.78
Rb co	3.26	–	–	–
Cs top	3.66	0.399	0.011	31.52
Cs co	3.43	0.398	0.014	31.55

In general, doping of the [6]Phenacene thin film leads to a different roughness due to the additional molecules that are distributed over the surface and inside the organic thin film. In this case, a lower roughness is obtained. This can be explained by the rougher pure film. In this case, alkali metals can fill the free space between the wedding cake islands of the pure film and therefore lead to a decrease in roughness. Regarding the lattice parameter, the co-deposited thin films with potassium showed the most pronounced change. The lattice parameter of rubidium could not be calculated due to the missing Bragg reflection and therefore the loss of the out-of-plane crystallinity. These significant changes in the thin

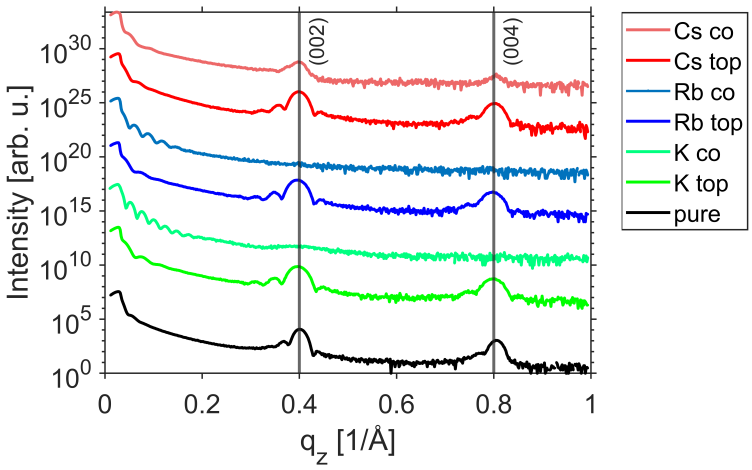

(a)

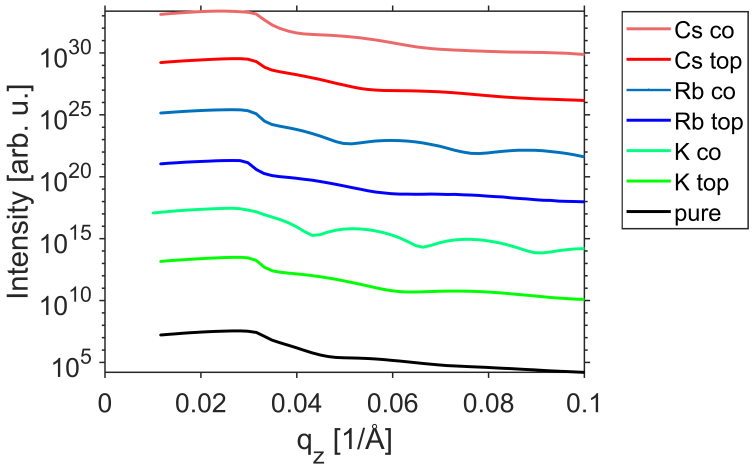

(b)

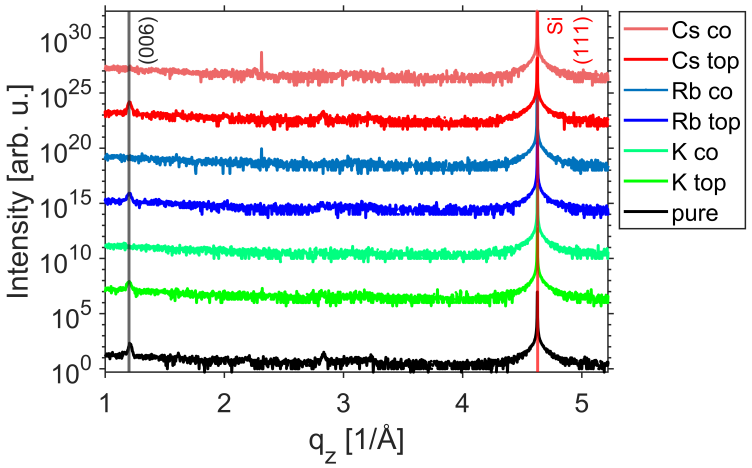

(c)

Figure 6.1.: XRR data of alkali metal doped [6]Phenacene thin films: a) standard q_z range b) low q_z range and c) high q_z range

film structure in-situ series with both dopants were further investigated at beamlines ID10 (ESRF) and P23 (DESY).

Potassium doping was performed at ESRF ID10 while measuring in-situ real-time XRR. Figure 6.2 shows the measurement of the co-deposition of 20 nm of [6]Phenacene at 2 Å/min together with potassium.

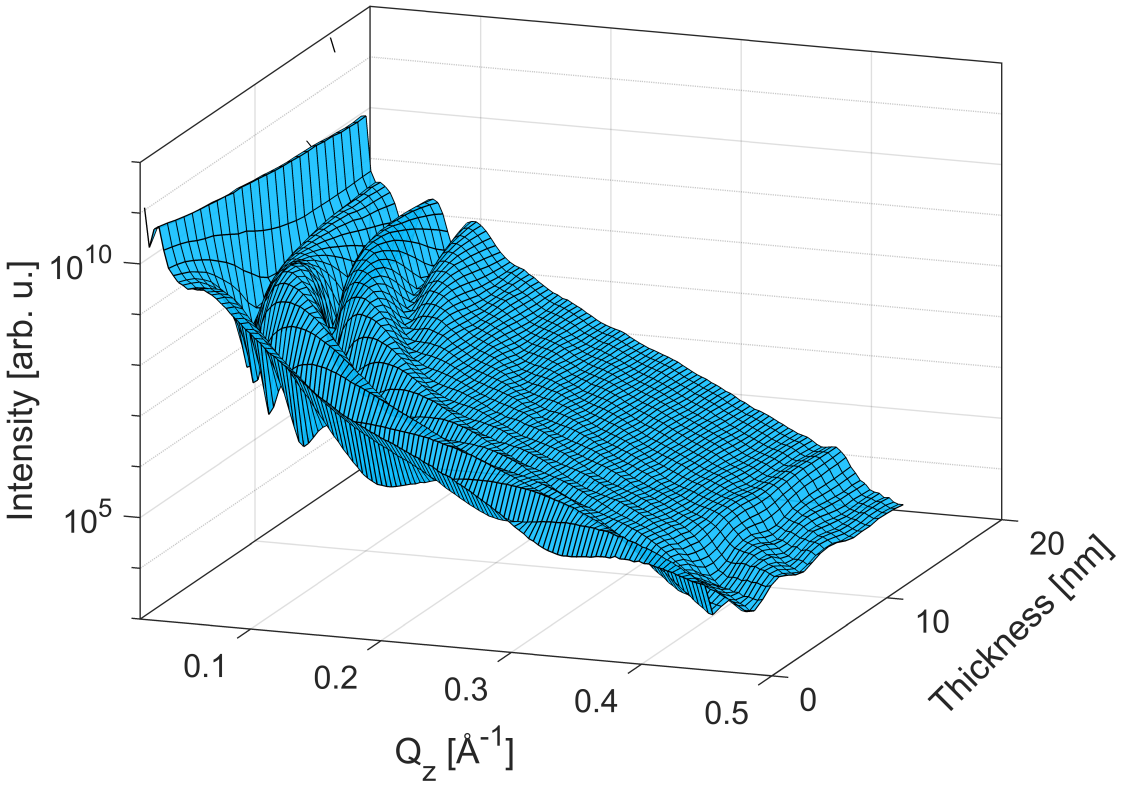

Figure 6.2.: In-situ XRR data of potassium co-deposition with [6]Phenacene.

Compared to the pure film, which was shown in Figure 5.2 in the last section, the (002) [6]Phenacene Bragg peak is less well pronounced than in the pure thin film. This Bragg peak gets visible at a film thickness of around 10 nm and gets more pronounced with increasing thickness. At a film thickness of around 20 nm, the peak is still barely visible and hard to fit compared to the pure [6]Phenacene thin film. Further analysis was performed by using the software GenX [113] to calculate the roughness. Due to the intercalated potassium atoms in the [6]Phenacene thin film, it was difficult to find a suitable fitting model and therefore a higher error in the calculation has to be taken into account. The fitting error can also be explained by the higher growth rate of the combined molecules and an XRR measurement with a longer integration time during the deposition. The results in Figure 6.3a show a steady increasing roughness with an increasing thickness which is a similar behaviour as the pure film. The roughness was fitted by using a linear fit inside a logarithmic plot with the

slope β of 0.42. It is slightly below the random deposition limit of $\beta = 0.5$ which is a sign for mound growth [140, 141]. The lattice parameter was calculated using Equation 4.11 and the (002) peak position that was fitted with a Gaussian distribution function. The results are shown in Figure 6.3b in which the date of the pure [6]Phenacene thin film is reproduced (compare with Figure 5.3a). To stop the thin film growth on time in the experimental setup, it was necessary to stop the measurement after its last full run at 18 nm. Therefore there is a slight gap between this value and the final value (20 nm) which was measured after stopping the deposition. The lattice parameter shows slightly higher values than the pure film, indicating the presence of additional potassium molecules inside the [6]Phenacene unit cell.

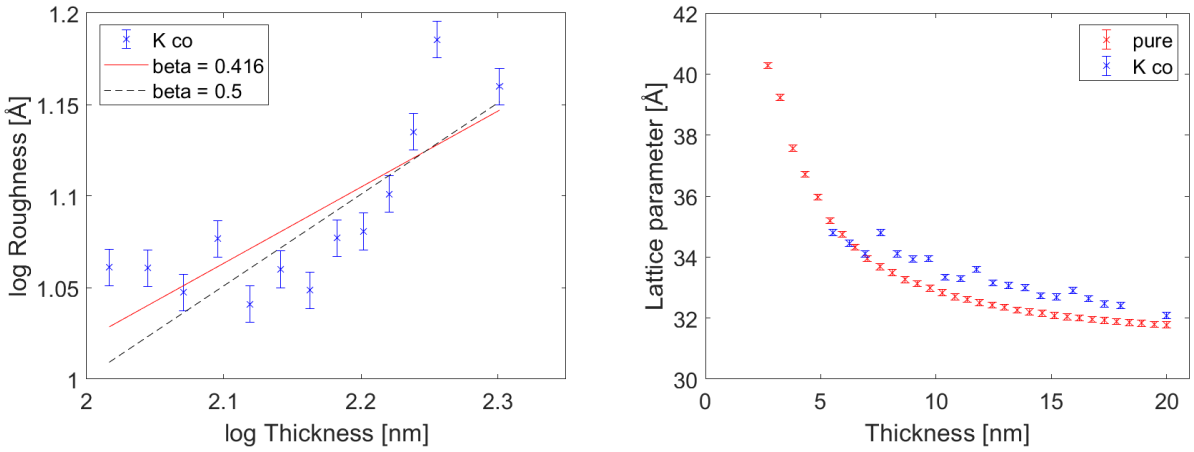

(a) (b)

Figure 6.3.: Data of the [6]Phenacene thin film co-deposited with potassium: a) roughness calculated with GenX and b) lattice parameter calculated with the [6]Phenacene (002) Bragg peak.

Rubidium doping was performed at DESY P23 while measuring in-situ real-time XRR. Figure 6.4 shows the measurement of the co-deposition of 20 nm of [6]Phenacene at 2 Å/min together with rubidium.

Compared to the pure [6]Phenacene thin film which is shown in Figure 5.2, rubidium co-deposition leads to the absence of Bragg reflections indicating a very low out-of-plane crystallinity in the [6]Phenacene thin film. The Kiessig oscillations however are very dominant, indicating a low roughness and a smooth thin film over the entire growth. The roughness was calculated by using the software GenX [113] and due to the intercalated rubidium atoms, a higher error has to be taken into account, *vide supra*. The results are shown in Figure 6.5 and indicate a more or less constant growth behaviour. However, due to the high error bars in the plot, it was waived to perform a fit to determine β.

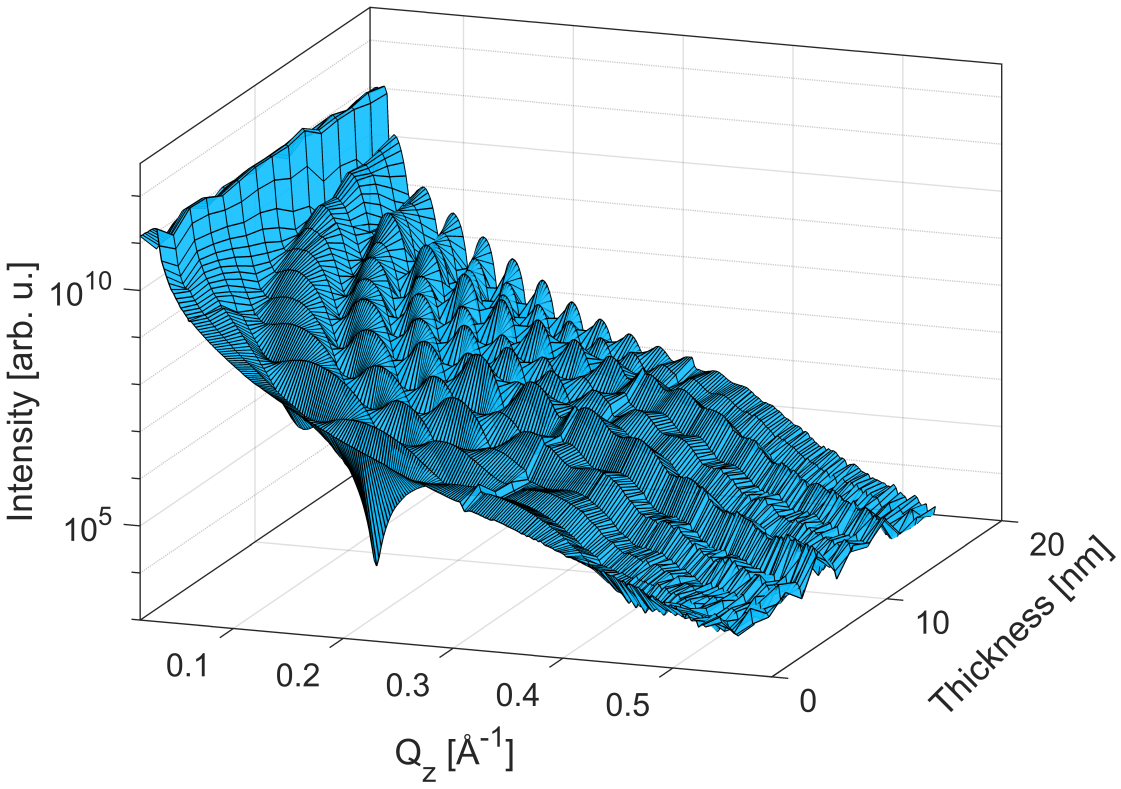

Figure 6.4.: In-situ XRR data of rubidium co-deposition with [6]Phenacene.

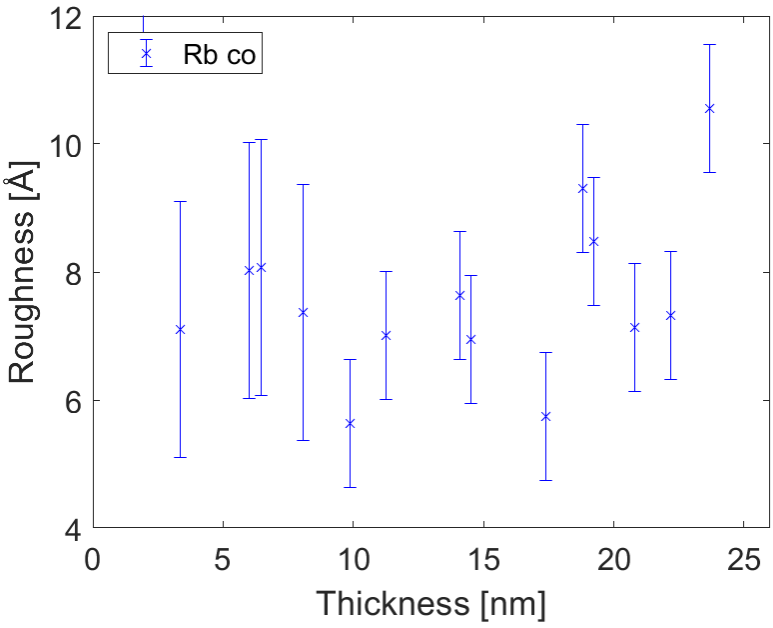

Figure 6.5.: Data of rubidium co-deposition with [6]Phenacene. Roughness determined with GenX.

The beamline P23 at DESY allowed to change the photon energy of the beam within seconds. This made it possible to study the thin film below and above the absorption edge of rubidium at 15.20 keV to study the distribution of the alkali metal in the thin film. In-situ measurements were performed at a photon energy of 12 keV to prevent beam damage. Further post-growth measurements were performed at additional energies of 15.10, 15.20 and 15.25 keV. Figure 6.6 shows an overview of the conducted measurements, containing the co-deposited film discussed above as well as the pure [6]Phenacene thin film for which after the growth of the organic layer and subsequent post-growth measurement, rubidium was deposited on top of it (Rb top).

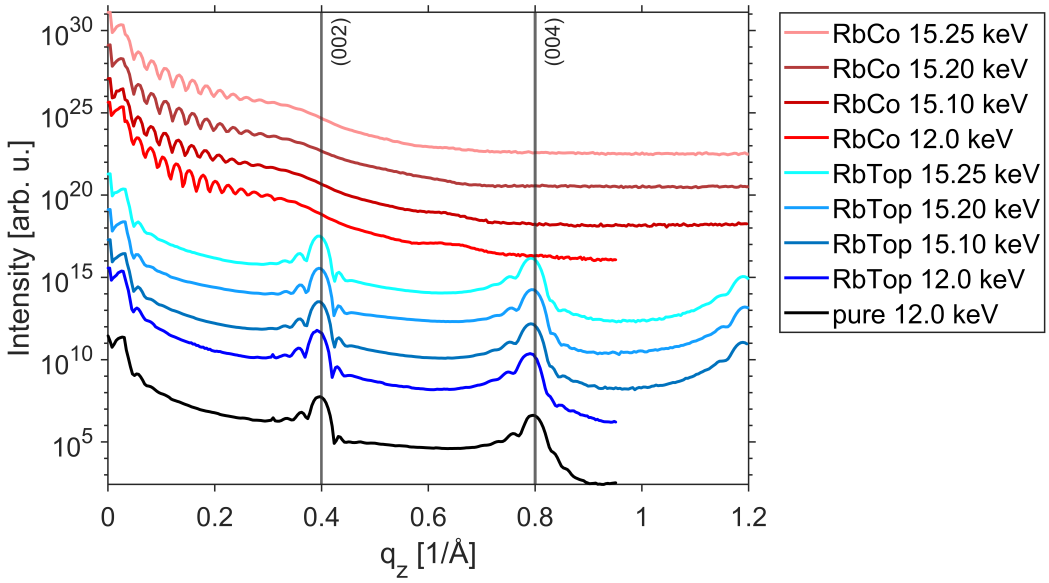

Figure 6.6.: XRR data of rubidium doped [6]Phenacene thin films. The measurements were conducted with different photon energies around the absorption edge of rubidium.

Compared to the co-deposited films, the on-top and pure films show the (002) and (004) Bragg reflections, indicating a high out-of-plane crystallinity. Differences between the pure and Rb top films are barely visible but a slight peak shift of the (002) and (004) Bragg reflections to lower q_z are observed. By tuning the photon energy, slight differences in the number of visible Kiessig oscillations especially for the co-deposited films can be seen. Further calculations, namely roughness calculation as well as fitting of the (002) peak were done using the same methods as above. The results are shown in Table 6.2.

Compared to the pure [6]Phenacene thin film, the on-top deposition of rubidium leads to a slightly smoother surface. This can be explained by rubidium molecules filling the gaps between the wedding cake islands of [6]Phenacene. The energy measurements show a smaller roughness before the absorption edge of rubidium and higher values after it. This

Table 6.2.: Film parameters derived from XRR measurements of rubidium doped [6]Phenacene thin films.

Film	Roughness [nm]	q_{Bragg} [1/Å]	FWHM [1/Å]	Lattice parameter [Å]
Pure 12.00 keV	3.38	0.396	0.021	31.72
Rb top 12.00 keV	3.33	0.392	0.020	32.04
Rb top 15.10 keV	3.04	0.396	0.021	31.82
Rb top 15.20 keV	3.03	0.396	0.018	31.76
Rb top 15.25 keV	3.19	0.395	0.019	31.81
Rb co 12.00 keV	1.06	–	–	–
Rb co 15.10 keV	1.08	–	–	–
Rb co 15.20 keV	1.09	–	–	–
Rb co 15.25 keV	1.11	–	–	–

is an indication that rubidium is responsible for the small roughness decrease. The lattice parameter also shows a change to a higher value, indicating that the [6]Phenacene unit cell changes slightly by the additional rubidium molecules. This however is not affected by higher photon energies showing nearly identical values above, at and below the total absorption edge of rubidium. Co-deposition leads to a total loss in out-of-plane crystallinity and shows only a small roughness increase for higher energies. However, the overall roughness is slightly lower than for the pure organic thin film, indicating a probably amorphous structure [159].

6.1.2. In-plane structure

Unit cell calculations: The in-plane crystal structure of all samples was investigated using GIWAXS measurements. Figure 6.7 shows an overview of the results. The upper image shows the pure [6]Phenacene thin film followed by the on-top deposited films on the left and the co-deposited films on the right side. It was expected that the alkali metals deposited on top intercalate into the already present [6]Phenacene thin film structure as shown by Roth et al. [42]. The intercalation influences the thin film structure by changing the unit cell parameters. This results in shifts of the position of reflections in reciprocal space to smaller q-values in general.

By comparing the position of Bragg reflections with pristine [6]Phenacene thin films, no change in the unit cell structure is observed. This would suggest that the atoms of alkali metals do not intercalate into the [6]Phenacene thin film, but stay at the top of the [6]Phenacene organic layer. The overall decrease in Bragg reflection intensity and disappearance of weak Bragg reflections support this observation. The layer of alkali metals on the surface of a thin film works as an attenuator that dampens the intensity of the X-ray beam that penetrates into the sample as well as the diffracted signal leaving the sample.

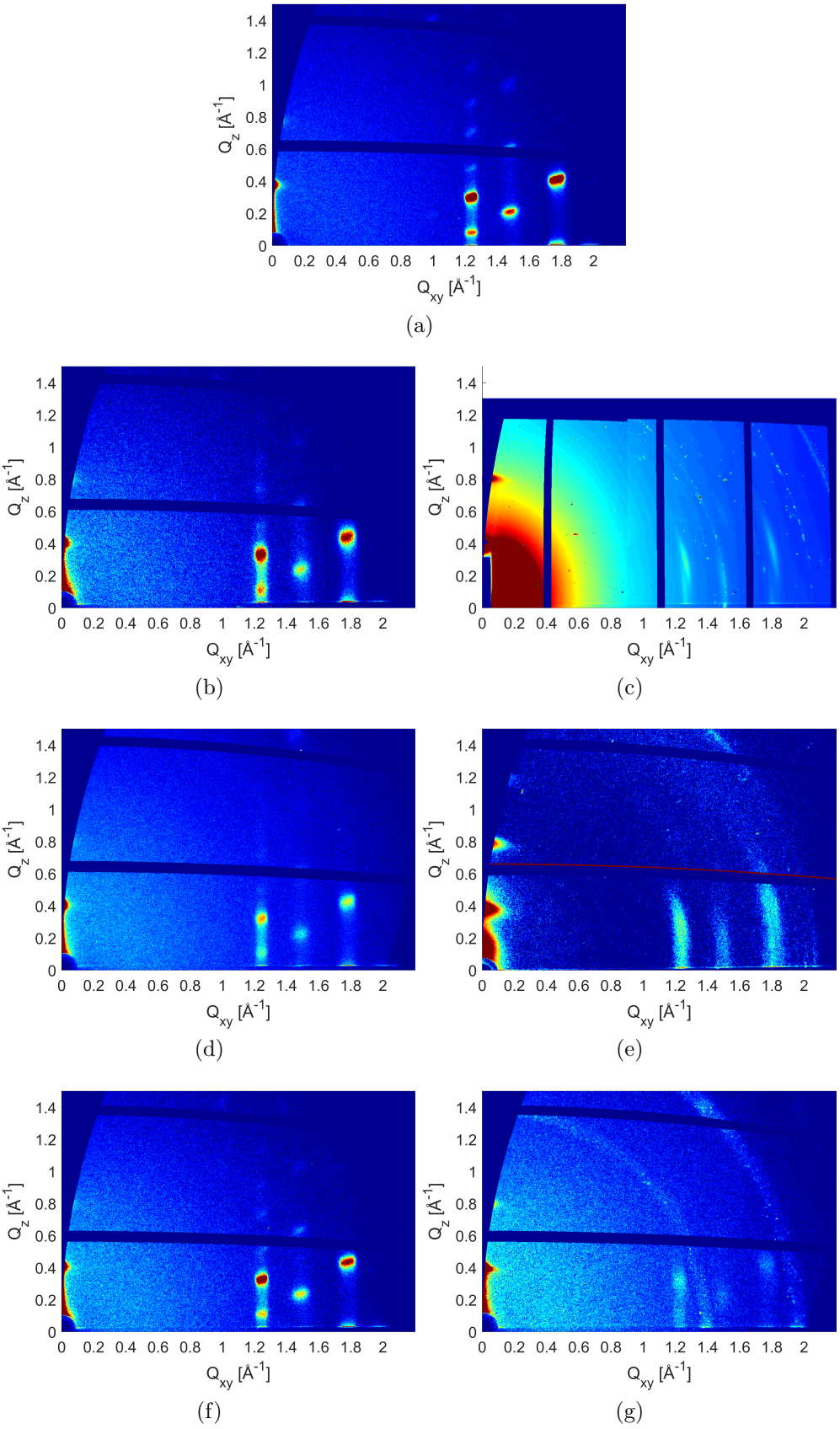

Figure 6.7.: GIWAXS images of 2 Å/min 20 nm [6]Phenacene films mixed with various alkali metals: a) pure, b) K on top, c) K co-deposition, d) Rb on top, e) Rb co-deposition, f) Cs on top and g) Cs co-deposition.

It was possible to perform further real-time in-situ measurements by continuing the measurements from Section 5.1.2. Potassium was deposited on top of [6]Phenacene while measuring in-situ real-time GIWAXS. These results connect directly to Figure 5.9 and show the evolution of unit cell parameters with increasing potassium thickness during the deposition. These results are depicted in Figure 6.8.

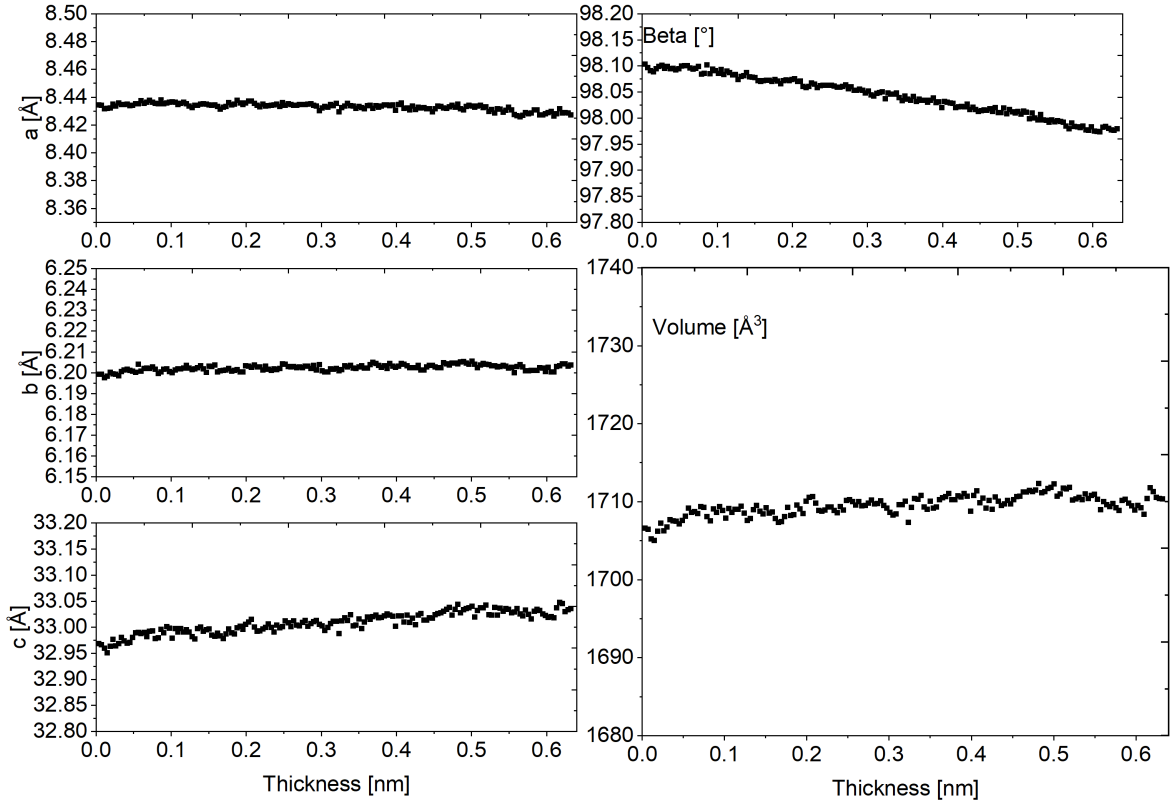

Figure 6.8.: Measured changes in the unit cell parameters during potassium deposition on top of [6]Phenacene. Continuation of Figure 5.9.

Potassium growth only shows a slight increase of c and a decrease of the β parameter which also supports the assumption that potassium does not intercalate into the [6]Phenacene thin film. True intercalation would have a stronger effect, therefore these very small changes can be mainly explained by experimental instabilities.

To study if thin film annealing could lead to the intercalation of potassium atoms into the [6]Phenacene unit cell, further experiments were performed with a 40 nm [6]Phenacene thin film with a higher potassium amount on top. GIWAXS at DESY P03 was measured during an annealing experiment [89]. The evolution of the (211) Bragg reflection was analysed and the resulting q_z curve over time is shown in Figure 6.9. The substrate temperature was slowly increased from room temperature to 240 °C resulting in a steady decrease of the q_z value with a maximum slope around 100 to 150 °C. At 200 °C also a slight broadening of the curve is visible indicating a lower intensity of the Bragg peak. After 240 °C the annealing

was stopped and the substrate was cooled down back to room temperature resulting again in an increase of q_z. It seems that mostly minor alignment changes due to the heating of the substrate holder seem to be responsible for the q_z shift and there is not enough evidence that potassium has a clear impact on the lattice plane spacing. Considering the last data point at 1800 s after cooling down, where the q_z value has decreased by ≈ 0.02 Å^{-1}, suggests a slight increase of the unit cell parameter perpendicular to the substrate.

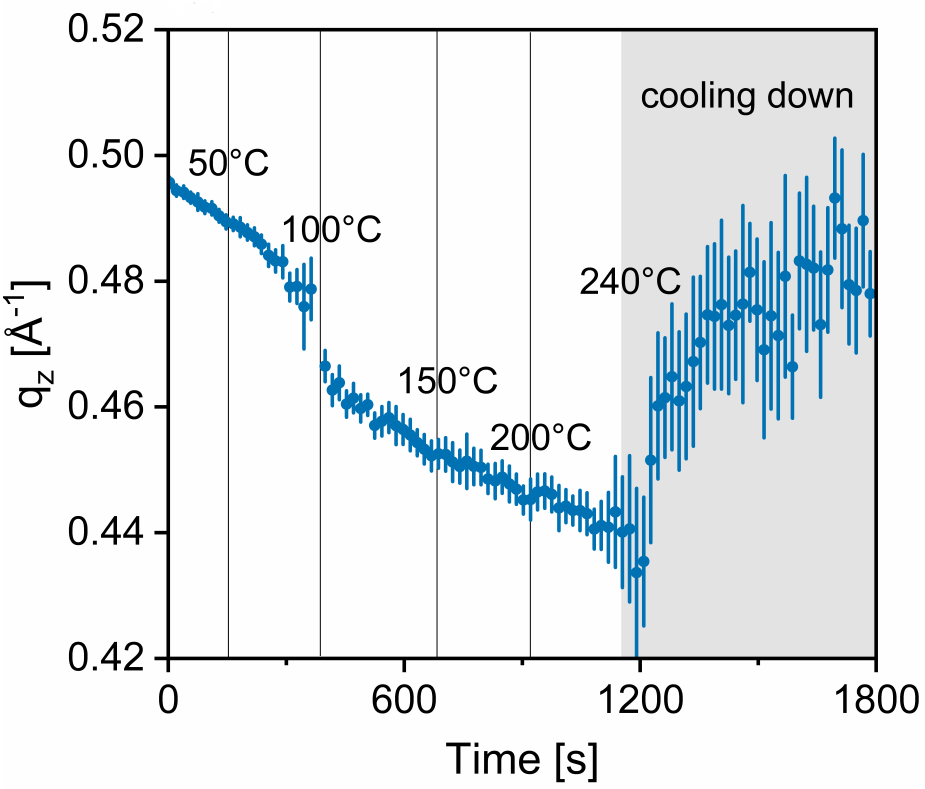

Figure 6.9.: Annealing of an 40 nm [6]Phenacene thin film with potassium on top. The (002) Bragg peak evolution is shown over time and the measured temperature values are marked in the graph with vertical lines. Taken from Ref. [89].

When alkali metals are co-deposited together with the [6]Phenacene, depending on the used alkali metal, a change in the thin film structure is observed. While the GIWAXS-patterns of the pure film (Fig. 6.7a) and the films with alkali metals on top exhibit sharp Bragg peaks, the co-deposited films lead to rings instead of sharp peaks. Sharp peaks indicate that the crystallites are well aligned with the substrate. In the case of co-deposited films, the orientation of crystallites is no longer aligned with the substrate. The statistical distribution of orientations leads to the characteristic rings seen in GIWAXS experiments. However, the overall quality of the doped thin films is relatively high, as it is possible to observe higher-order Bragg reflections in the out-of-plane direction as well as clearly defined peaks in the in-

plane direction. Based on peak positions in the reciprocal space map, the doped [6]Phenacene thin films maintain the same unit cell orientation as the pure thin films with respect to the substrate surface. When the position of the observed peaks is fitted, the unit cell parameters can be calculated, using the genetic algorithm optimization method mentioned in Section 4.4.4.1. The calculated unit cell parameters for a potassium doped [6]Phenacene thin film are: $a = 8.6$ Å, $b = 6.2$ Å, $c = 32$ Å and $\beta = 96°$. The angles alpha and gamma are 90°, as the unit cell stays monoclinic similar to the pristine [6]Phenacene thin film. When these unit cell parameters are compared with the ones calculated for the pristine thin film, several conclusions can be drawn. The c unit cell parameter does not change. From the previous GIWAXS measurements and the calculation of the molecular orientation, it is known that the molecules of [6]Phenacene are oriented in a standing-up configuration. In this case, the c unit cell parameter corresponds to two molecules since there are two molecules at the bottom of the unit cell and two molecules at the top, compared with Figure 5.5 in which the crystal unit cell of [6]Phenacene is depicted. On the other hand, the change in the a and b unit cell parameters as well as the angle β is observed. This change can be explained by a slight reorientation of [6]Phenacene molecules inside the unit cell to accommodate the additional potassium atoms. This is an indication that the potassium atoms are intercalated inside the [6]Phenacene thin film structure and not just creating phase-separated domains of pure potassium. Additionally, there are no visible reflections or rings that could be attributed to phase-separated domains of pure potassium. The previously mentioned higher degree of misorientation compared to pristine thin films can be explained by different numbers of [6]Phenacene molecules and potassium atoms between unit cells. This leads to local inhomogeneities of potassium doping concentrations on the nanoscale. Another explanation would be that the potassium atoms could weaken the substrate-molecule interaction with [6]Phenacene in favour of the interaction between potassium and [6]Phenacene. The topic of the doping ratio will be discussed later in this chapter.

A similar trend was also observed for the co-deposition of rubidium doped [6]Phenacene thin films. However, the observed reflections are even less well-defined compared to potassium doped thin films. Ordering in an out-of-plane direction is comparable to the previous thin film as it is possible to observe the higher orders of reflections from the stacking of the $00l$ planes. On the other hand, an even higher degree of misorientation than for the potassium doped thin films is observed here, indicated by strong smearing of the observed peaks. Similar to the potassium doped thin films, the position of observed reflections was fitted and subsequently, a full set of unit cell parameters was calculated. The results for rubidium doped [6]Phenacene thin films are $a = 8.4$ Å, $b = 6.4$ Å, $c = 32$ Å and $\beta = 99°$. There is no measurable change in the c unit cell parameter. The reasoning for this observation is expected to be similar to the previous case with potassium as the dopant. Intercalation of alkali metals has

no impact on the stacking periodicity in an out-of-plane direction, which is mainly influenced only by the length of molecules and their tilt relative to the direction perpendicular to the substrate surface. Intercalation of rubidium atoms into the unit cell, however, influences the molecular packing of [6]Phenacene molecules in the in-plane direction. A change in both a and b unit cell parameters is observed. This is caused by the presence of rubidium atoms inside the unit cell, which intercalate in between the neighbouring [6]Phenacene molecules, causing a slight increase in the intermolecular distance. Additionally, a small change in the unit cell angle β compared to pristine [6]Phenacene is observed, caused by a slight rotation of the molecules inside the unit cell. Similar to [6]Phenacene thin films doped with potassium, the Bragg reflections from pristine rubidium domains are not observed. This is an indication, that most atoms of rubidium intercalate into the unit cell of [6]Phenacene and do not create phase-separated pristine domains.

When [6]Phenacene is co-deposited together with the caesium atoms, complete phase segregation is observed. The position of the observed well-defined reflections corresponds to the pristine [6]Phenacene thin film. Additionally, the set of Debye-Scherrer ring features is clearly visible in the reciprocal space map. The position of the rings corresponds to the positions of caesium present as a polycrystalline powder. It can be concluded that the atoms of caesium do not intercalate into the [6]Phenacene unit cell, but rather create phase-separated domains of pure caesium atoms mixed in between domains of pristine [6]Phenacene.

Depending on the type of alkali metal atom that was used for doping of a [6]Phenacene thin film, a different mixing behaviour is observed. A possible explanation for this is that the size of the alkali atom has a significant impact on its ability to intercalate inside the [6]Phenacene unit cell. Both potassium and rubidium atoms are small enough to intercalate inside the [6]Phenacene crystal. The increased size of rubidium atoms disrupts the ordering of the thin film to a higher degree than what was observed for comparatively smaller potassium atoms. On the other hand, much larger caesium atoms are not able to admix with [6]Phenacene and instead completely phase-separate. This shows that for the proper doping of the [6]Phenacene thin films, the size of dopants has to be considered. When the size of the dopant atom is too large, only the physical mixture of the phase-separated pristine domain is obtained, instead of the homogeneous layer of an organic-inorganic mixture.

Calculations of the molecular orientation: As mentioned in the previous paragraph, if the [6]Phenacene thin film is doped by alkali atoms, there is a small but observable change in the unit cell parameters. This is caused by the slight change in the tilt of the [6]Phenacene molecules to accommodate additional alkali metal atoms in a crystal. To properly understand the doping process, it has to be determined, how the atoms of dopants are distributed in the thin film. Due to a low number of observed peaks in the GIWAXS data for alkali doped

[6]Phenacene thin films, it is not possible to use the same calculations to determine the position of atoms inside the unit cell as used for pristine thin films described in Section 4.4.4.2. However, this change in the tilt of molecules and the position of alkali metals can be estimated by using the method described below.

Four molecules of [6]Phenacene with the same molecular orientation as calculated of a pristine [6]Phenacene thin film, described in Section 5.1.2 were positioned inside of the unit cell with the unit cell parameters calculated from the GIWAXS data of alkali metal doped thin films (Figure 6.7). Subsequently, alkali metal atoms were positioned inside this unit cell. The number of alkali metal atoms was selected based on the XPS data from Section 6.3. Using the genetic algorithm, the position and orientation of the [6]Phenacene molecules as well as the position of the alkali metal atoms have been varied slightly and subsequently, the overlap between all the atoms inside the unit cell was calculated. The species with the lowest overlap was used in the subsequent generations until a reasonable result was found. The position and rotation of the [6]Phenacene molecules during the calculation was limited to only a maximum of 3% of the unit cell parameter in each direction and 5° around each of the three axes, respectively. The restriction of the unit cell size was chosen based on the calculated unit cells of the pristine and doped thin films, which were very similar, so a more significant change in the molecular orientation was not expected. The movement of alkali metal atoms was constrained so that the position follows the same packing motif as the [6]Phenacene molecules. After the reasonable estimation of the dopant atom positions was obtained, the intensity of Bragg peaks based on the structure factor was calculated and compared to the experimental data.

Figure 6.10 shows the final result for potassium doped [6]Phenacene thin films. There are eight atoms of potassium per unit cell (2:1 potassium:[6]Phenacene ratio measured by XPS, *vide infra*). The position and orientation of the [6]Phenacene molecules change slightly to better fill the slightly larger volume of the unit cell when compared to a pristine thin film. The atoms of the dopant are then distributed evenly throughout the entire volume of the unit cell of the simulation and are intercalated in between the neighbouring [6]Phenacene molecules. It was expected that the atoms of potassium can positively impact the semiconducting properties of doped thin films by mediating the charge carrier transport between the molecules of [6]Phenacene, in addition to increasing the density of charge carriers in a thin film. Unfortunately, it is not possible to perform similar calculations for the rubidium doped thin films because of the earlier-mentioned weaker crystallinity and associated ordering. Finally, atoms of caesium do not intercalate into [6]Phenacene crystals, but phase-separate.

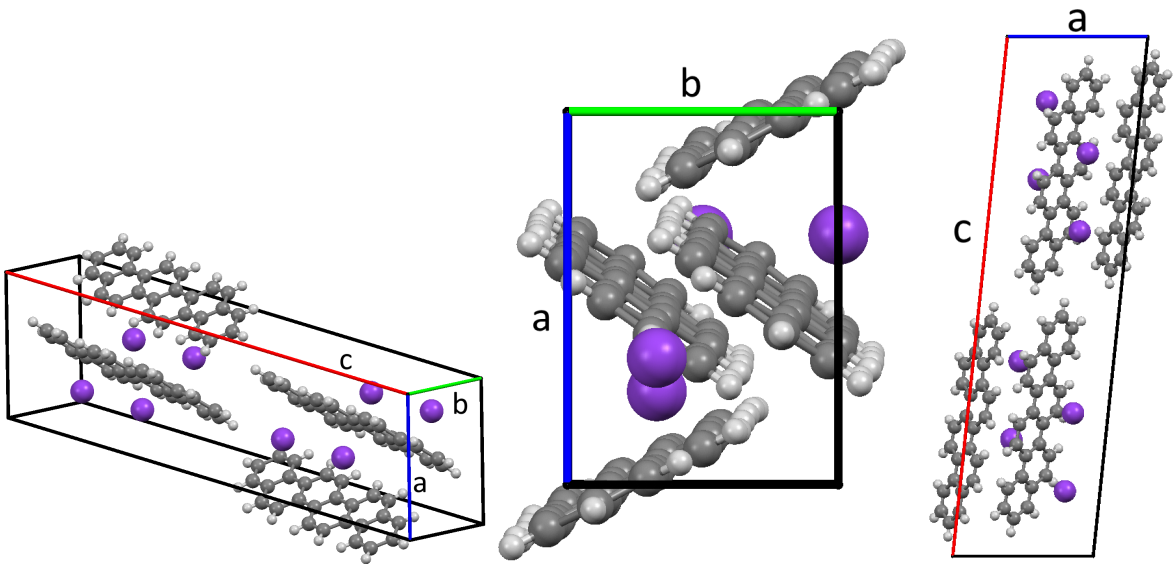

(a) (b) (c)

Figure 6.10.: Unit cell orientation of potassium doped [6]phenacene: a) side view, b) *ab*-plane perpendicular to the substrate surface and c) *ac*-plane parallel to the substrate surface.

6.2. Morphology

Figure 6.11 shows the comparison between a 2 Å/min 20 nm [6]Phenacene thin film before and after a short potassium deposition on top of it to get insight into the structure formation in the early stages of potassium deposition. Potassium on-top deposition is visible as additional dots in the AFM image while the main wedding cake structure stays intact. This causes an RMS-roughness increase from 2.35 nm for the pure film to 3.14 nm for the potassium doped thin film.

These experiments were continued with potassium, rubidium and caesium alkali metals as well as longer on-top deposition times and co-deposition together with [6]Phenacene. Figure 6.12 shows an overview of the complete series. The upper part is showing on-top deposition with potassium, rubidium and caesium (from left to right) while the lower parts show co-deposition for the same molecules.

The RMS roughness was extracted with Gwyddion using the complete or only parts of the image depending on the image quality. The grain size was calculated by marking the islands using a threshold and calculating the mean grain size. Table 6.3 shows an overview of the calculated values of all films. On-top deposition leads to an additional layer of grains on top of the [6]Phenacene thin film, while some parts of the original wedding cake structure can still be seen. This demonstrates that the organic structure is preserved even after the deposition of the alkali metals. The size of the grains depends on the used alkali

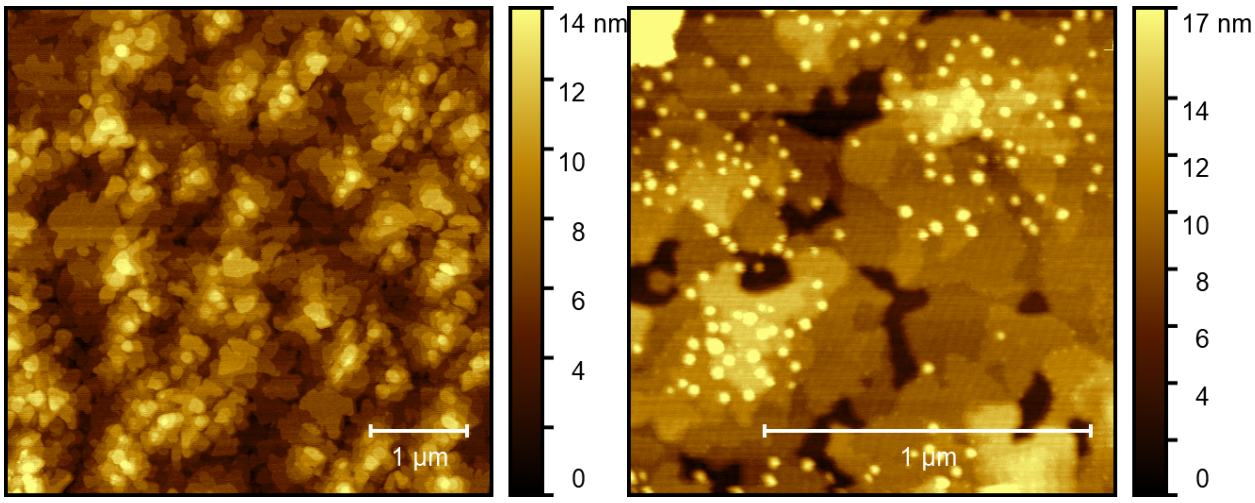

(a) (b)

Figure 6.11.: AFM images of 2 Å/min 20 nm [6]Phenacene thin films. The scale bar shows a 1 μm scale which varied for each image: a) pure and b) K on top.

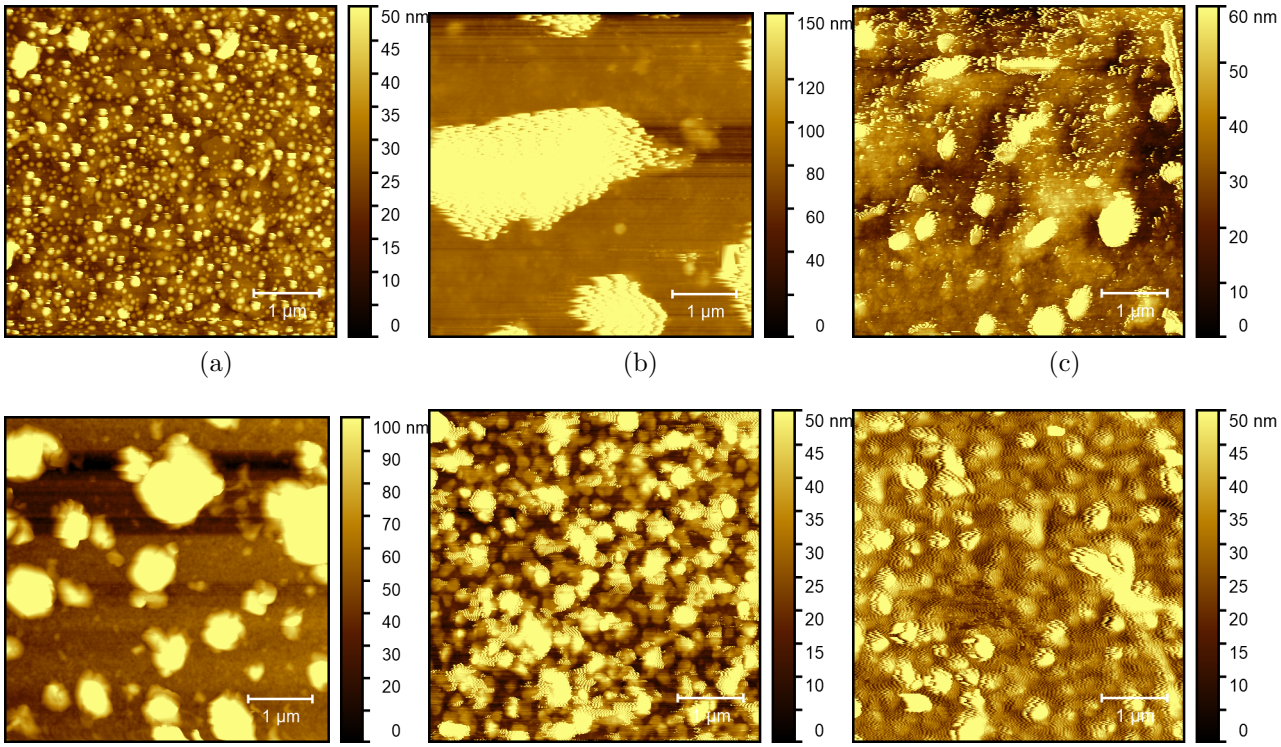

(a) (b) (c)

(d) (e) (f)

Figure 6.12.: AFM images (1 µm scale is shown in image) of 2 Å/min 20 nm [6]Phenacene films mixed with various alkali metals: a) K on top, b) Rb on top, c) Cs on top, d) K co-deposition, e) Rb co-deposition and f) Cs co-deposition.

metal and increases from potassium to caesium and rubidium. This is also the case for the RMS roughness in which potassium shows the lowest value and rubidium the highest. Co-deposition leads to the formation of islands on the thin film while the [6]Phenacene wedding cake structure is not visible anymore. The island size also depends on the used alkali metal, with potassium leading to the largest mean island size, while similar island sizes are obtained if using rubidium or caesium.

Table 6.3.: Roughness extracted from AFM images.

Film	Roughness [nm]	Mean grain size [nm]
Pure	2.1	–
K top	13.3	63.2
Rb top	51.8	1066
Cs top	23.3	278.5
K co	47.1	92.8
Rb co	22.3	18.5
Cs co	17.2	18.9

Due to the high roughness of alkali doped [6]Phenacene thin films, the acquisition and evaluation of AFM images was very difficult. Also, the image quality tends to be rather faulty with lots of artefacts compared with pure films. To solve this issue further measurements were conducted using SEM, which offers excellent contrast for thin films of high roughness. These images were post-processed using the software GIMP [160] to increase the overall sharpness and brightness. The corresponding raw images can be found in the Appendix 10.2. Figure 6.13 shows the SEM image of pure [6]Phenacene at an voltage of 5 kV, magnification of 10.000x and working distance of 10 mm. Because of the low roughness, it is very hard to notice a pattern in this picture, but the top of the wedding cake islands can be at least surmised.

Additional SEM measurements were conducted for the alkali doped films which are shown in Figure 6.14. Again, the upper row shows the on-top films with potassium on the left, followed by rubidium in the middle and caesium on the right, while the lower row shows the co-deposited films. As mentioned above, the on-top depositions show the formation of grains which cover the wedding cake structure. This is also visible much clearer in SEM though the wedding cake structure can only be adumbrated. While potassium and rubidium show round grains, caesium creates a more square-liked structure. This square-liked structure is also visible in all of the co-deposited films with a smooth structure between the grains. Additionally, long needle-like structures are visible in all films. The co-deposited films show that these consist of several long-shaped grains that are connected to each other.

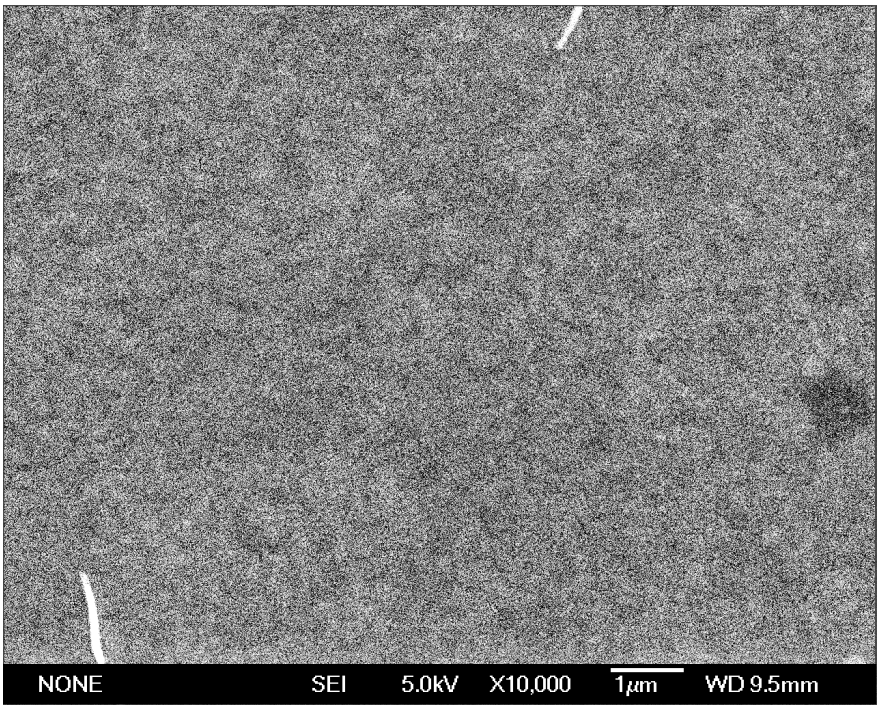

Figure 6.13.: SEM image of a 2 Å/min 20 nm [6]Phenacene thin film.

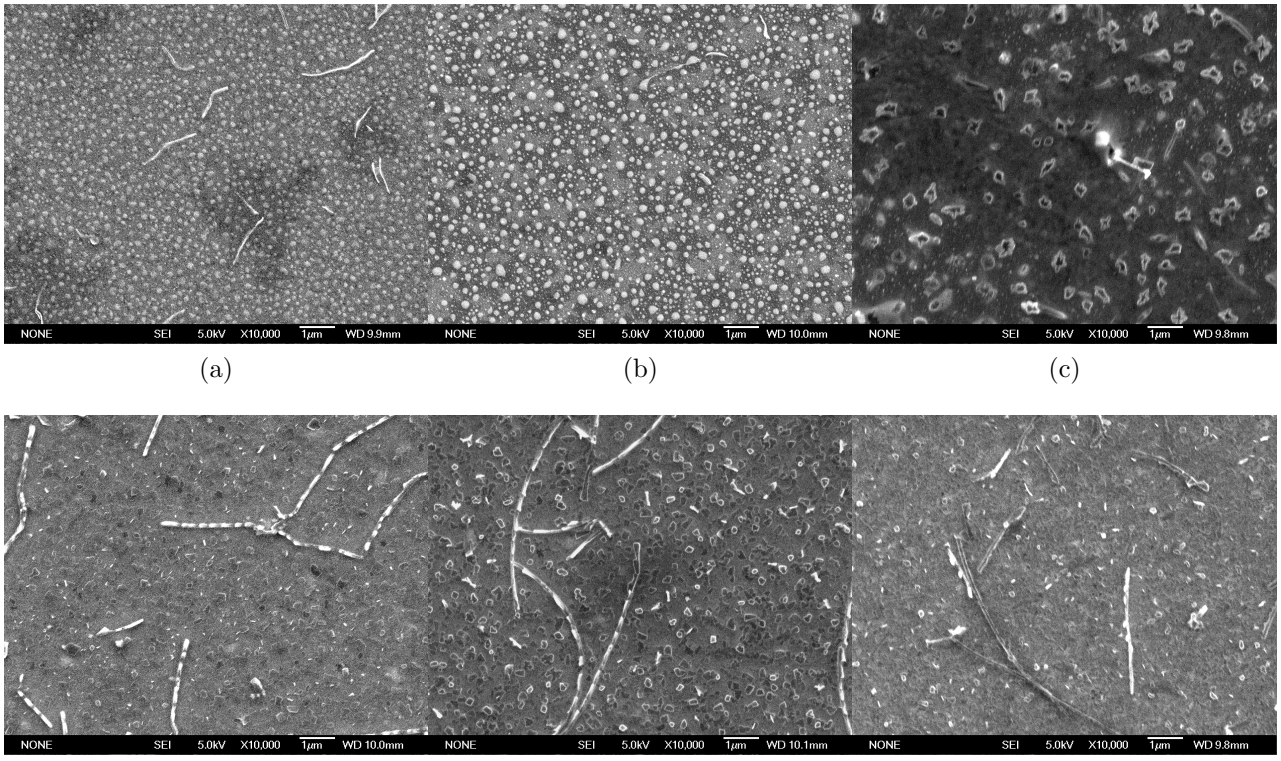

(a) (b) (c)

(d) (e) (f)

Figure 6.14.: SEM images of 2 Å/min 20 nm [6]Phenacene films mixed with various alkali metals: a) K on top, b) Rb on top, c) Cs on top, d) K co-deposition, e) Rb co-deposition and f) Cs co-deposition.

6.3. XPS

To check the success of alkali metal deposition on top and co-deposition with [6]Phenacene organic thin films, XPS was used. By performing a survey scan over the energy range from 0 to 1000 eV it was possible to identify the corresponding peaks of the used alkali metals. The scans are shown in Figure 6.15.

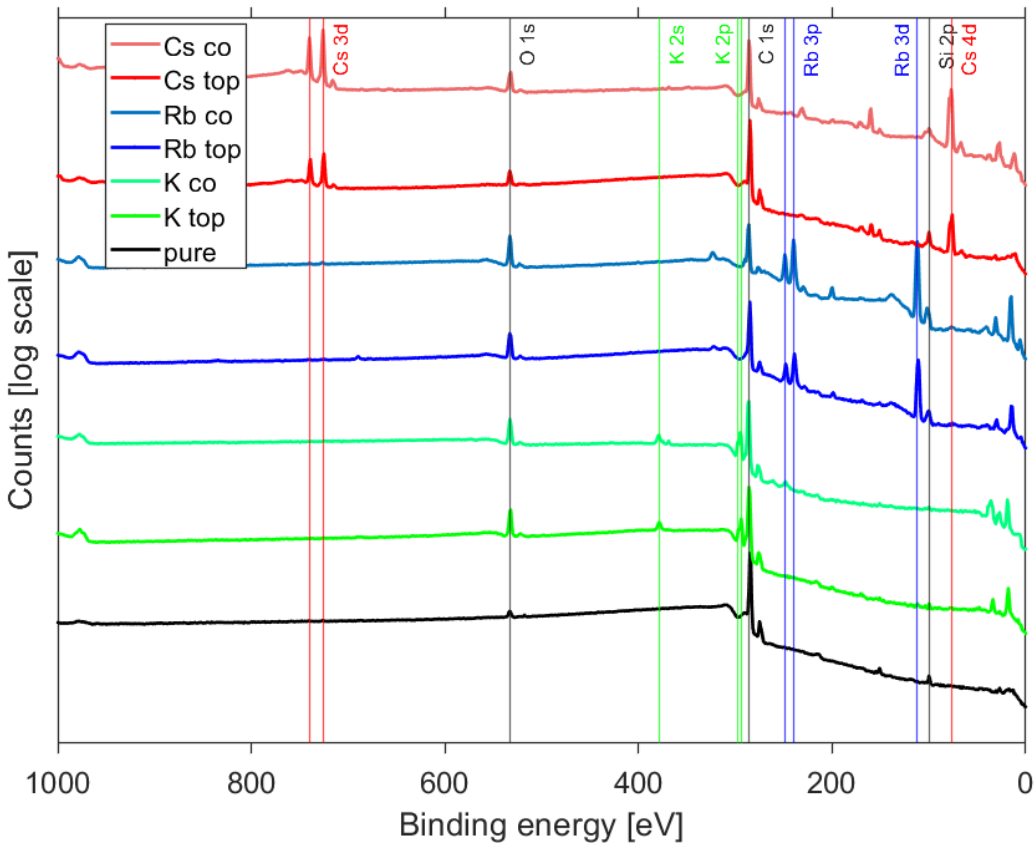

Figure 6.15.: XPS spectra of alkali metal doped [6]Phenacene thin films. The corresponding peaks for each alkali metal as well as for silicon, carbon and oxygen are marked by different coloured vertical lines.

Potassium peaks are marked in green (K 2s and 2p), rubidium in blue (Rb 3d and 3p) and caesium in red (Cs 3d and 4d) by vertical lines. The silicon (Si 2p) and oxygen (O 1s) belong to the silicon substrate, while carbon (C 1s) belongs to the [6]Phenacene organic film. These peaks are marked with a black vertical line. It is also worth mentioning that the thin films are free of cross-contaminations between the different alkali metals, which could have happened between substrate or dispenser changes during the film series. The measurements show that the corresponding alkali metals are detected on the thin film surface and possibly in the [6]Phenacene thin film structure. However, due to the different film preparation techniques (on-top and co-deposition), different approaches were taken to quantify the results. In

general, region scans were performed for each characteristic XPS peak mentioned above and a Gaussian was used to extract its integral value. For the on-top deposition, it is suspected that the most amount of alkali metals is located on top of the thin film, therefore the alkali deposition leads to an attenuation of the C 1s signal. This attenuation can be used to approximate the thickness of the alkali metal amount. By using the area value of the C 1s peak combined with the inelastic mean free path λ it was possible to calculate the alkali thickness using Equation 4.18. The results are shown in Table 6.4.

Table 6.4.: Calculations of the alkali metal amount on top of [6]Phenacene thin films using the area value of the C 1s peak intensity and the inelastic mean free path λ for each alkali metal.

Sample	C 1s	λ [Å]	Thickness [Å]
pure	437844	-	180
K top	200906	76	59
Rb top	206703	82	97
Cs top	266112	89	44

For co-deposited thin films, the alkali atoms may be intercalated into the thin film structure as a [6]Phenacene-alkali mixture. In this case, the ratio between the carbon and alkali peak was used to get an estimation of the number of alkali atoms per [6]Phenacene molecules. This was done by using the C 1s peak integral values, which were corrected with a relative sensibility factor (RSF) relative to the C 1s peak. The number of alkali atoms was calculated by using the ratios between C 1s and the corresponding alkali peaks. 26 carbon atoms were used per [6]Phenacene molecule. The results are shown in Table 6.5 and were used in Subsection 6.1.2 for the calculation of the unit cell orientation.

Table 6.5.: Estimated number of alkali atoms inside alkali metal co-deposited [6]Phenacene thin films.

Sample	Alkali atoms per C atom	Alkali atoms per [6]Phe molecule
K co	0.10	2.6
Rb co	0.34	8.8
Cs co	0.048	1.3

6.4. UV/vis/NIR spectroscopy

The optical properties of alkali metal doped [6]Phenacene thin films were studied using UV/vis/NIR absorption spectroscopy. Figure 6.16 shows the absorption spectra with the extinction coefficient k of the pure and several alkali metal doped [6]Phenacene thin films. The curves were scaled by their measured thicknesses after deposition. Beginning with the on-top deposition in Figure 6.16a, all thin films show the already mentioned vibronic progression at 3.17, 3.37 and 3.51 eV as well as the peak at 4.15 eV discussed in Section 5.3. The absorption spectra of the co-deposited thin films in Figure 6.16b show more drastic changes. The first peak gets shifted slightly around $50-100$ meV. The caesium co-deposited thin film shows a similar behaviour as the pure film with similar peak positions and a vibronic progression. However, when taking a look at potassium and rubidium thin films the vibronic progression is masked due to the stronger background and the main peak at 4.15 eV gets broadened. It is possible that through the changing unit cell parameters, the optical properties of [6]Phenacene thin films doped with alkali metals are altered.

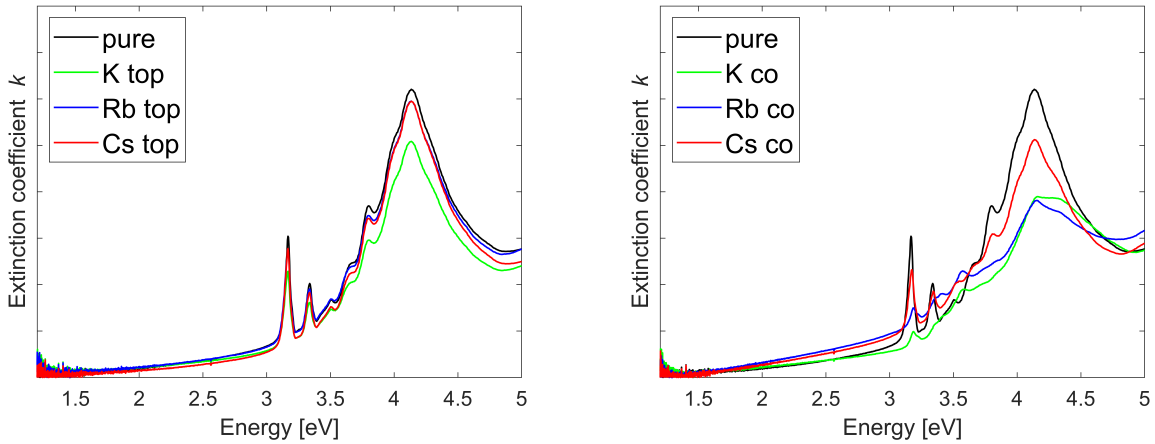

(a) (b)

Figure 6.16.: UV/vis/NIR absorption spectra of alkali metal doped [6]Phenacene thin films: a) on-top deposition and b) co-deposition.

6.5. Discussion

The crystal structure and morphology of the organic-inorganic hybrid system [6]Phenacene combined with the alkali metals potassium, rubidium and caesium grown on native silicon substrates was investigated. The deposition of alkali metals was either performed on top of a pure [6]Phenacene thin film or as co-deposition during the growth of [6]Phenacene. The resulting thin films were investigated using real-time XRR and GIWAXS measurements during deposition, supplemented with additional AFM, SEM, XPS and absorption measurements.

XRR and GIWAXS measurements showed, that if alkali metals are deposited on top of [6]Phenacene, its crystallinity in the out-of-plane and in-plane direction stays intact and no change in the unit cell structure is observed. Absorption spectroscopy measurements also showed no changes in the optical properties. It was expected that the alkali metals deposited on top intercalate into the already present [6]Phenacene thin film structure as shown by Roth et al. [42] for the molecules tetracene and pentacene. However, this was not the case here, as the alkali metal atoms did not diffuse into a [6]Phenacene thin film, but stayed on top of it. Therefore, the intercalation seems to be dependent on the used molecule or on the preparation conditions. Another method that could induce intercalation would be post-growth annealing to induce structural changes as performed by Lorch et al. [161]. During the in-situ XRR experiments with potassium and rubidium, all thin films were slowly annealed after deposition to look for intercalation and no such effect could be found. Roughness changes were observed in both XRR and AFM/SEM measurements showing a changing roughness for all on-top alkali doped thin films. XRR scans with different photon energies of rubidium on top of [6]Phenacene showed a rubidium dependence on the roughness change. The AFM and SEM images show a formation of grains, which cover the wedding cake structure and therefore these roughness changes can be explained by the additional grains on top. Depending on the roughness of the pure [6]Phenacene molecule, the additional atoms are either filling the space between the wedding cake terraces, leading to a lower roughness or covering the surface with grains, leading to a higher roughness. A schematic representation of alkali metals on top of [6]Phenacene is shown in Figure 6.17.

When alkali metals were co-deposited during [6]Phenacene growth, changes in the thin film structure that depend on the used alkali metal were observed. XRR and GIWAXS measurements of potassium and rubidium co-deposited [6]Phenacene thin films showed changes of the crystallinity in the out-of-plane and in-plane directions. Potassium showed an indication for mound growth behaviour with increasing thicknesses [140, 141]. Both potassium and rubidium thin films showed a higher lattice parameter than the pristine thin film. The GIWAXS images showed blurred Bragg peaks which could be explained by a higher degree of misorientation in [6]Phenacene and no visible reflections that can be attributed to phase-separated domains of potassium and rubidium. This misorientation can be explained

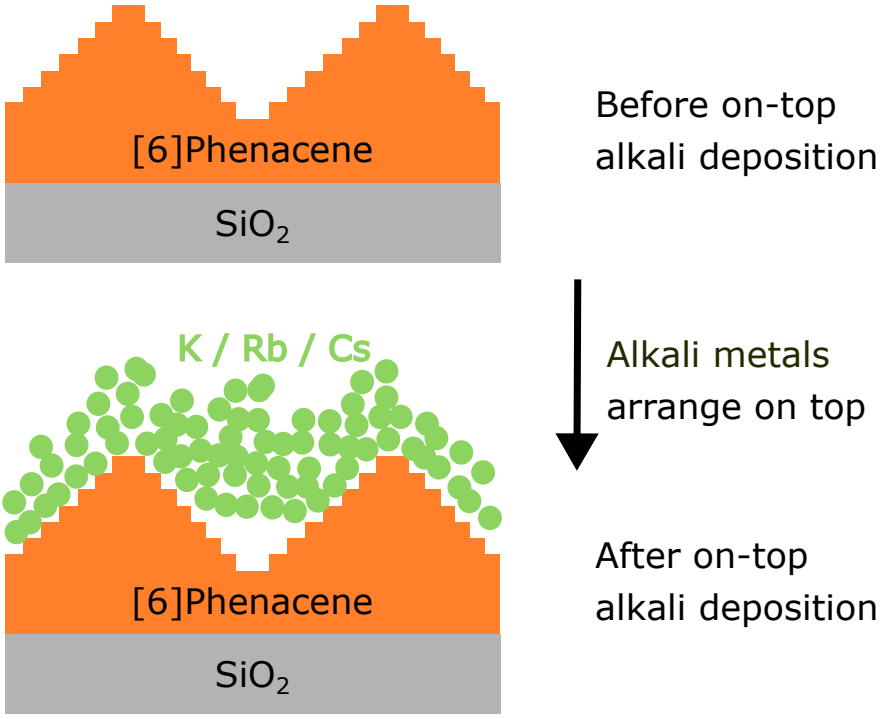

Figure 6.17.: Overview of alkali metals on top of a [6]Phenacene thin film. Alkali metals stay on top and no intercalation into the thin film was observed.

by an inhomogeneous number of potassium or rubidium atoms between the unit cells or by potassium/rubidium atoms, that weaken the substrate-molecule interaction and favoured the interaction of potassium/rubidium and [6]Phenacene. It was possible to calculate the unit cell of [6]Phenacene co-deposited with potassium or rubidium. Both results are similar to the pristine thin film and are showing slight changes in the b and β unit cell parameters indicating a slight reorientation to accommodate the additional potassium and rubidium atoms in the unit cell. The c unit cell parameter showed no measurable change, indicating that the intercalation does not affect the out-of-plane stacking periodicity. Overall, these results indicated that potassium and rubidium alkali atoms intercalate into the [6]Phenacene unit cell which leads to structural changes, therefore XPS measurements were performed to estimate a ratio between alkali atoms and [6]Phenacene molecules. These results were used to calculate the molecular orientation of [6]Phenacene co-deposited with potassium and are shown in Figure 6.18. Unfortunately, it was not possible to perform the same calculation for rubidium doped thin films due to the higher misorientation and lower GIWAXS pattern quality.

Co-deposition of [6]Phenacene with caesium leads to a complete loss of the out-of-plane crystallinity. GIWAXS measurements showed weak Bragg reflections that correspond to the pristine thin film and Debye-Scherrer rings that correspond to caesium powder. This indicates a complete phase segregation of pure caesium domains mixed in between domains of

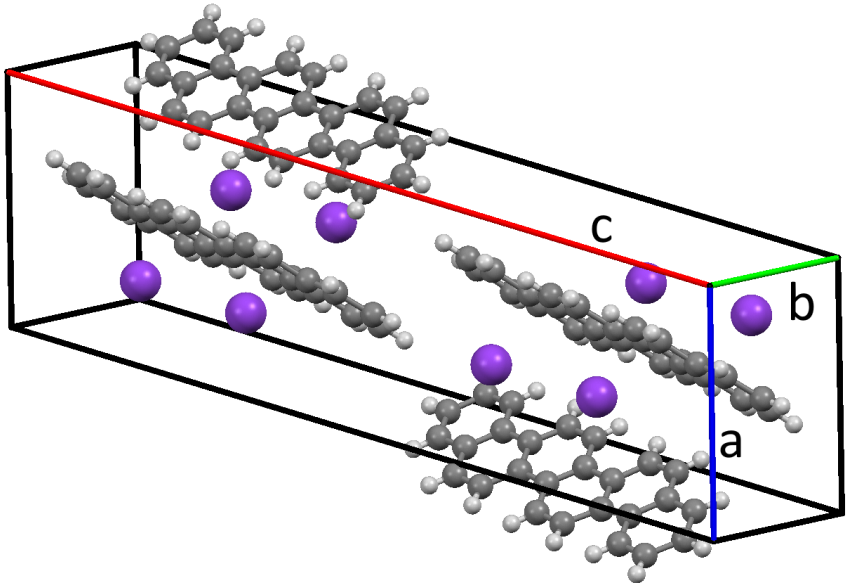

Figure 6.18.: Schematic representation of the molecular orientation of a [6]Phenacene molecule co-deposited with potassium.

pristine [6]Phenacene. A possible explanation why potassium and rubidium intercalated into the [6]Phenacene unit cell and caesium did not, would be the size of each atom. Potassium and rubidium atoms are small enough to intercalate into the [6]Phenacene crystal structure. Due to the increased size of rubidium, a lower degree of order is seen in the thin film, than what was observed for the smaller potassium atoms. Therefore the much larger caesium atoms are not able to admix with [6]Phenacene and thus completely phase-separate. This shows that for proper [6]Phenacene thin film doping also the size of the dopants has to be considered. A homogeneous layer of an organic-inorganic mixture is only obtained when the size of the dopant is not too large. The morphology of co-deposited [6]Phenacene thin films with alkali metals shows the formation of islands with square-like grains and needle-like structures that consists of connected grains scattered over the complete thin film. The grain size and type depended on the used alkali metal. The absorption data for co-deposited thin films of [6]Phenacene together with alkali metals showed changes for potassium and rubidium which is an indication, that the optical properties change due to the changing unit cell parameters. These changes were, however, not observed for caesium co-deposition, where the unit cell structure is not altered. An overview of the results in this chapter is shown in Figure 6.19.

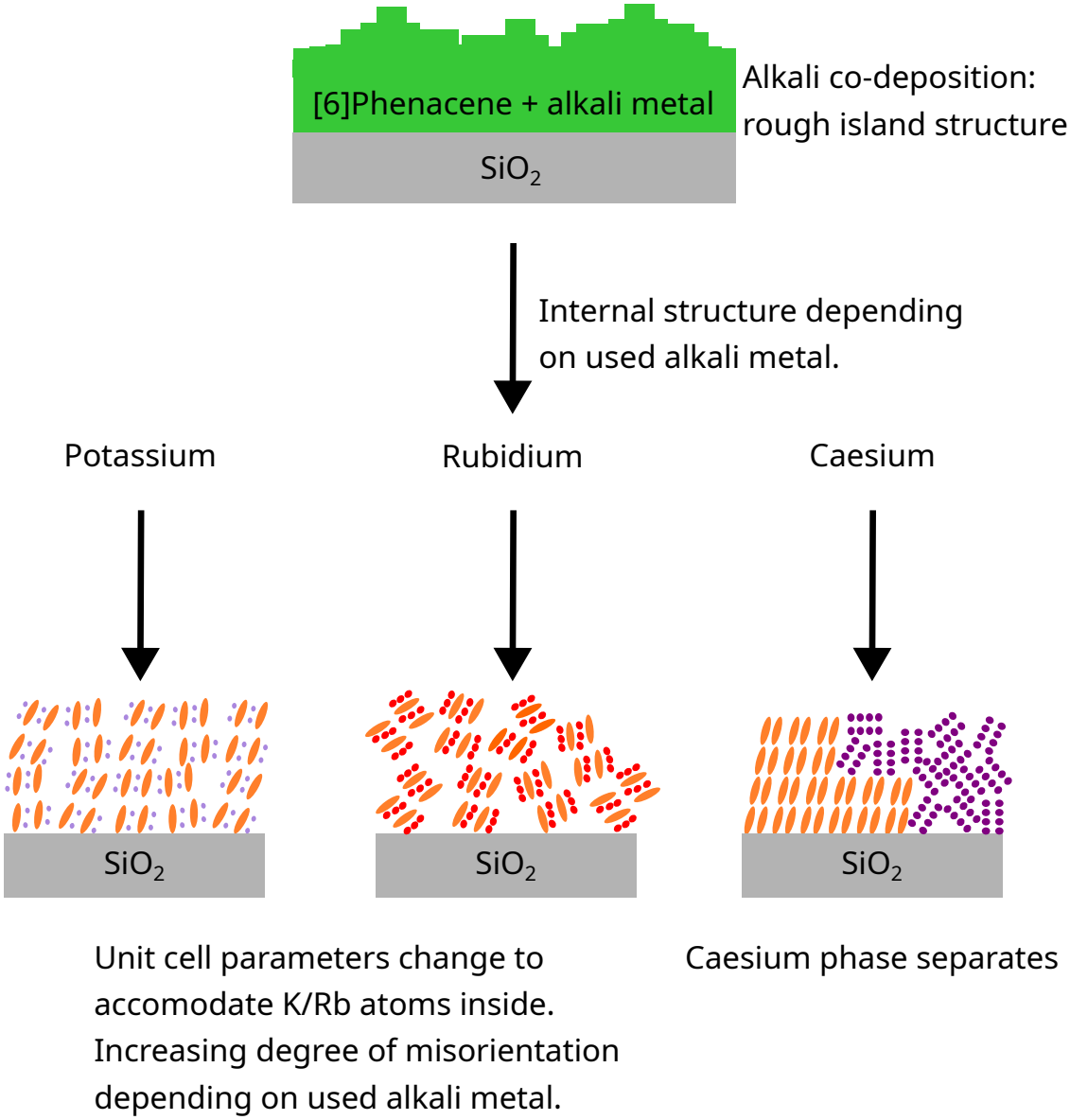

Figure 6.19.: Overview of [6]Phenacene and alkali metal co-deposition. Potassium and rubidium intercalate into the [6]Phenacene unit cell, leading to a slight misorientation. Caesium leads to phase separation.

7. Gold doped [6]Phenacene thin films

Gold is a very important contact material for organic devices and in this section, the impact of gold deposition on the structure and morphology of [6]Phenacene is characterized. Silicon substrates were prepared according to Section 4.3 and pure films of [6]Phenacene were grown. Afterwards, they were taken out of the vacuum chamber and mounted in another chamber that was equipped with a metal evaporation cell and an XPS setup to check the success of gold deposition after the experiment. These preliminary experiments were used to perform subsequent synchrotron experiments. Further experiments were performed at ESRF BM32 that covered the in-situ real-time deposition of [6]Phenacene and gold deposition afterwards while maintaining UHV conditions.

7.1. Crystal structure

The determination of the crystal structure was performed by X-ray scattering and is divided into the out-of-plane and the in-plane structure similar to Section 5.1.

7.1.1. Out-of-plane structure

Figure 7.1 shows XRR data of four 18 nm [6]Phenacene thin films that have been prepared simultaneously. Afterwards, three of them were moved to another chamber for on-top gold deposition with different deposition times at a low growth rate.

The figures indicate a well-defined out-of-plane crystal structure that remains intact even after gold deposition on top. It can be seen that, due to the attenuation of X-rays by the gold layer, the intensity of the [6]Phenacene Bragg peak decreases at longer deposition times while maintaining its position. Further analysis was performed by using the software GenX [113] to determine the surface roughness. The first (002) Bragg peak was fitted with a Gaussian to determine the peak position, FWHM and deduce the lattice parameter using Equation 4.11. The results are shown in Table 7.1.

The calculated roughness in the second of Table 7.1 row shows an increase after initial gold deposition which decreases with increasing gold deposition time. Due to the simple model applied in the GenX fitting routine (one single layer), it was problematic to evaluate the thin films with gold on top correctly. Therefore, additional fits with multiple layers,

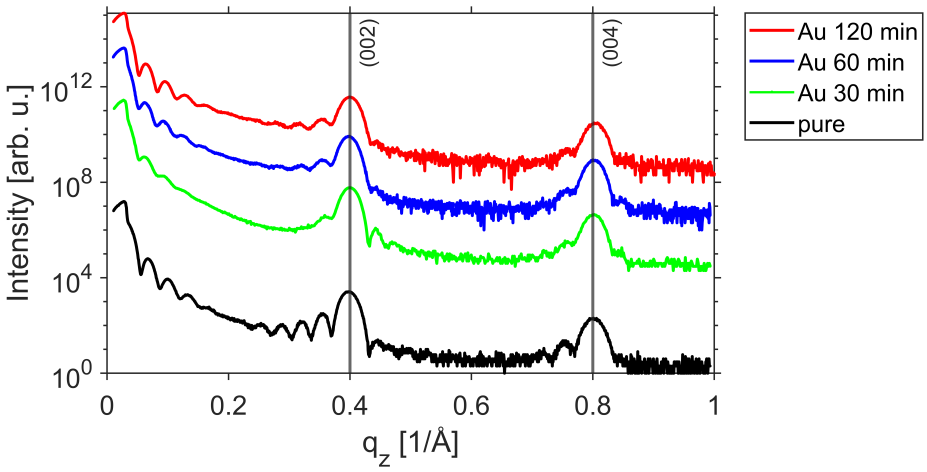

Figure 7.1.: XRR data of [6]Phenacene thin films with gold on top. Different time spans for the gold deposition were used.

Table 7.1.: Film parameters derived from XRR measurements of [6]Phenacene thin films with gold on top. The roughness was calculated with GenX. The other data was calculated with the (002) [6]Phenacene Bragg reflection.

Film	Roughness [nm]	q_{Bragg} [1/Å]	FWHM [1/Å]	Lattice parameter [Å]
Pure	1.85	0.398	0.026	31.58
Au 30 min	2.75	0.400	0.025	31.44
Au 60 min	2.21	0.398	0.025	31.58
Au 120 min	1.63	0.400	0.027	31.44

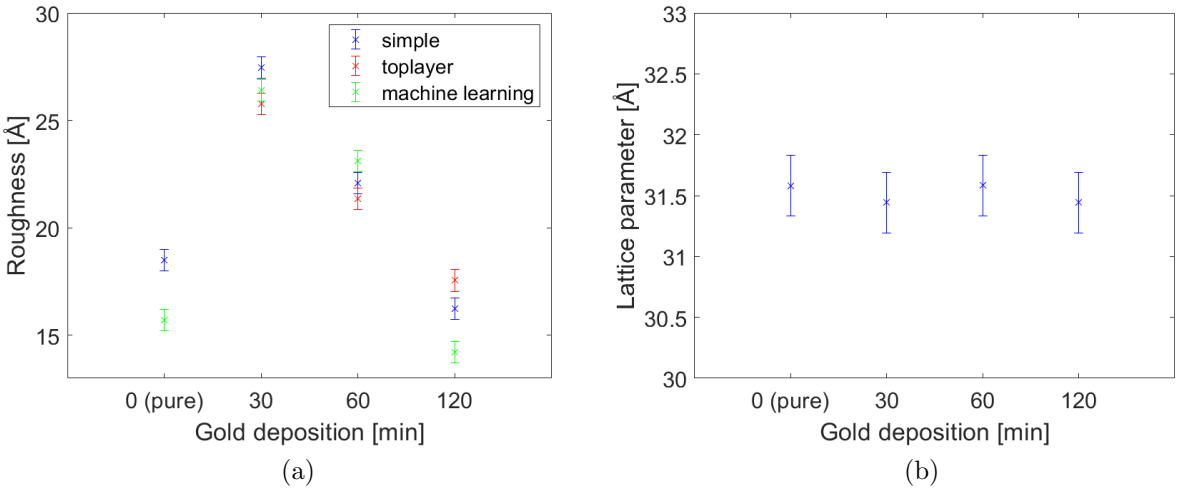

Figure 7.2.: a) Roughness calculated with GenX and b) lattice parameter calculated with the (002) [6]Phenacene Bragg peak.

where only the top layer, as well as machine learning-based fits (see Refs. [115, 116]), were performed. The results show similar roughness behaviour, which is shown in Figure 7.2a. This variation in roughness can be explained by atoms of gold being deposited on top of the [6]Phenacene wedding cake terraces. By increasing the gold deposition duration, further gold atoms stick to the surface and also fill the gaps in the valleys between the wedding cakes, leading to a smoother surface than for the pure film. Significant changes in the FWHM as well as in the lattice parameter cannot be seen (compare with Figure 7.2b). This means that the [6]Phenacene thin film structure stays intact when small amounts of gold are deposited on top of it.

To continue this study with a higher amount of gold, further experiments were conducted at ESRF BM32 by applying in-situ XRR measurements during [6]Phenacene and subsequent gold deposition. Thin films of [6]Phenacene with a thickness between 10 and 20 nm were deposited with a growth rate of 2 Å/min onto native silicon substrates while measuring in-situ XRR. The deposition was performed at room temperature with a measured substrate temperature after gold deposition at 315 K (substrate heating due to the deposition). Afterwards, the deposition of 5 to 20 nm of gold was measured with in-situ XRR. After each deposition post-growth measurements were performed. Figure 7.3 shows an overview of the conducted post-growth measurements after each deposition. Due to the large measurement range, the pictures were split into three parts covering a q_z range up to the second Bragg reflection of [6]Phenacene in Figure 7.3a, a smaller range for a better view of the total reflection edge in Figure 7.3b as well as a high angle view in Figure 7.3c covering the gold (111) Bragg reflection. The shown 40 nm thin film was pre-deposited in our home laboratory and gold deposition was performed at ESRF. For a better overview, Figure 7.3 shows only the data of the first pure film corresponding to the lower gold deposition amount.

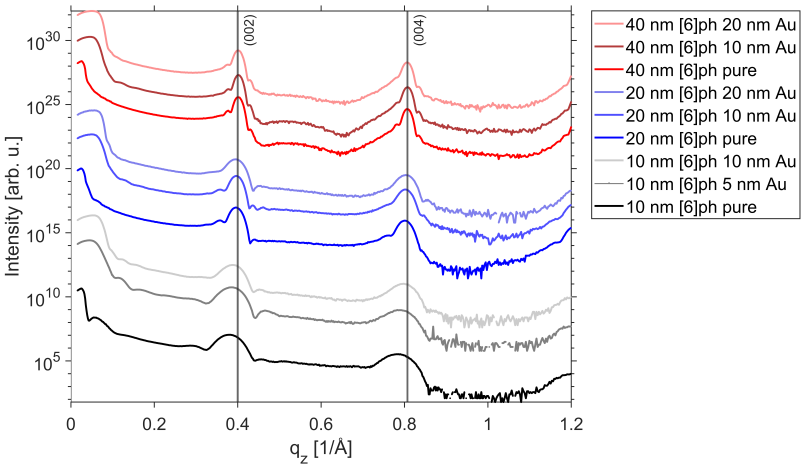

(a)

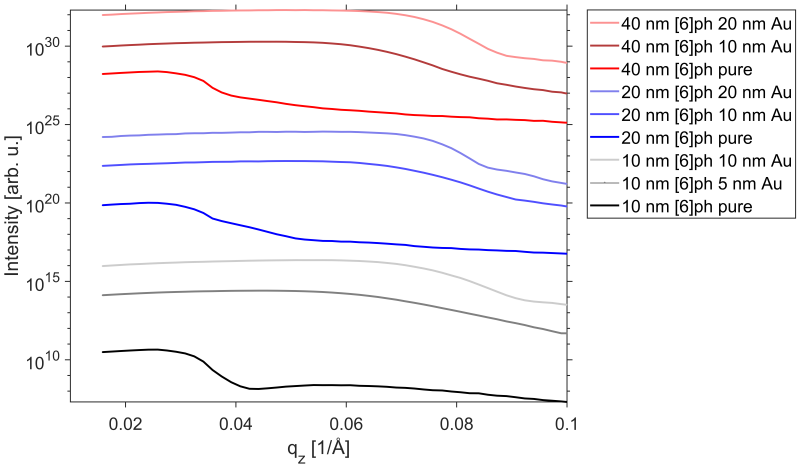

(b)

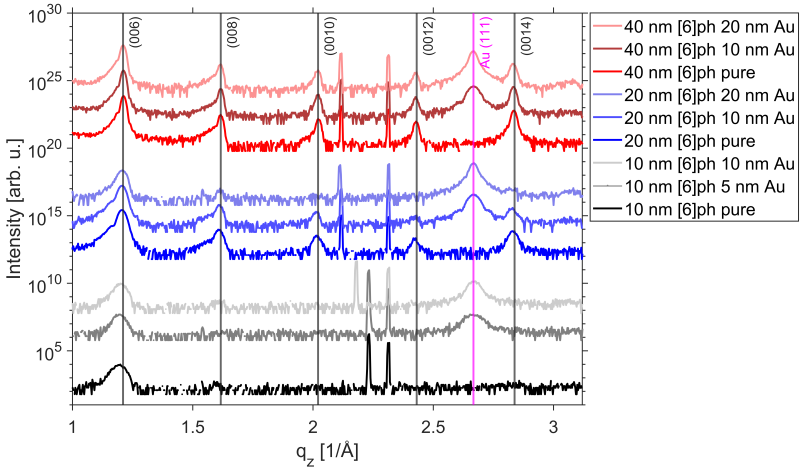

(c)

Figure 7.3.: XRR data of [6]Phenacene thin films with gold on top: a) standard q_z range, b) low q_z range and c) high q_z range.

Further peak fitting was done with the [6]Phenacene (002) Bragg peak to calculate the out-of-plane lattice parameter. Additional roughness calculations were done by using the Parratt formalism with the software GenX [113]. Both results are shown in Table 7.2. The calculated roughness in the second row has to be viewed with caution. Due to the high roughness of the initial thin film, especially at high thicknesses and the gold deposition, the fitting in GenX resulted in some inaccuracies.

Table 7.2.: Film parameters derived from XRR measurements from [6]Phenacene thin films with gold on top from ESRF BM32. The position of the (002) [6]Phenacene Bragg peak was used to calculate the values.

Film	Roughness [nm]	q_{Bragg} [1/Å]	FWHM [1/Å]	Lattice parameter [Å]
10 nm pure	2.15	0.379	0.046	33.14
5 nm Au on top	3.25	0.384	0.046	32.71
10 nm pure	2.95	0.383	0.041	32.73
10 nm Au on top	2.96	0.387	0.039	32.50
20 nm pure	4, 26	0.396	0.022	31.75
10 nm Au on top	5.20	0.396	0.023	31.70
20 nm pure	4.24	0.392	0.028	32.09
20 nm Au on top	5.02	0.394	0.029	31.86
40 nm pure	6.24	0.401	0.017	31.32
10 nm Au on top	5.24	0.402	0.015	31.28
40 nm pure	6.15	0.401	0.016	31.36
20 nm Au on top	5.31	0.401	0.015	31.34

However, Figure 7.3a shows that after the on top gold deposition, the overall crystallinity of the organic thin film stays intact while the films get slightly rougher. At higher angles, the higher-order Bragg peaks attributable to [6]Phenacene get slightly attenuated when gold is deposited on top of the thin film. This effect is more pronounced at low [6]Phenacene and high gold thicknesses (see Figure. 7.3c). The gold (111) Bragg reflection can be seen at $q_z = 2.67$ Å^{-1}. It is getting more pronounced for higher gold thicknesses. By fitting this peak with a Gaussian, it was possible to calculate the crystallite size with the FWHM and Equation 4.12. The results for the corresponding FWHM as well as the crystallite sizes that are increasing with the gold thickness are shown in Table 7.3.

The sharp peaks between q_z values of 2 and 2.4 Å^{-1} are coming from the instrument setup. The change in the total reflection edge can be seen in Figure 7.3b. The results of the lattice parameter will be discussed later in the in-situ part. By approximating the location of the total external reflection edge, it was possible to calculate the electron density with Equation 4.13 for each prepared thin film. The results are shown in Table 7.4. While pure [6]Phenacene shows an electron density of around 0.48 1/Å^3, gold leads to a significant increase of up to 3.36 1/Å^3.

Table 7.3.: Film parameters derived from XRR measurements from [6]Phenacene thin films with gold on top from ESRF BM32. The (111) gold peak was used to determine the values. The first line in each section shows the corresponding base film.

Film	q_{Au} [1/Å]	FWHM [1/Å]	Crystallite size [Å]
10 nm pure	-	-	-
5 nm Au on top	2.67	0.075	84.32
10 nm Au on top	2.67	0.048	130.28
20 nm pure	-	-	-
10 nm Au on top	2.67	0.043	144.87
20 nm Au on top	2.67	0.028	224.56
40 nm pure	-	-	-
10 nm Au on top	2.67	0.033	192.03
20 nm Au on top	2.67	0.026	241.57

Table 7.4.: Electron density calculations of [6]Phenacene thin films with gold on top. Calculated from Figure 7.3b.

Film	Total reflection edge q_c [1/Å]	Electron density ρ [1/Å^3]
10 nm pure	0.026	0.48
5 nm Au on top	0.050	1.76
10 nm Au on top	0.067	3.17
20 nm pure	0.026	0.48
10 nm Au on top	0.064	2.89
20 nm Au on top	0.069	3.36
40 nm pure	0.026	0.48
10 nm Au on top	0.059	2.46
20 nm Au on top	0.067	3.17

Figures 7.4 and 7.5 show an overview of the conducted in-situ measurements of all depositions. The figures are divided by the thickness of the pure [6]Phenacene base film of 10 nm and 20 nm. The left side shows the pure film, while the right side shows the corresponding film after gold deposition. Differences during the growth of pure films with the same thickness can be explained by variations in the substrate temperature as well as different substrate positions.

The growth plots of pure [6]Phenacene show similar behaviour as the ones already discussed in Subsection 5.1.1. The lattice parameters were calculated using the same methods as described above and are shown in Figure 7.6. The graphs are divided by the source film of 10 or 20 nm of [6]Phenacene. The left part of each plot shows the evolution of the lattice parameter during the growth of the pure [6]Phenacene thin film and is divided by a line, while the right part shows the gold deposition that follows afterwards. The used colour in each graph marks the corresponding deposition with the same film. It can be seen in both graphs that 10/20 nm pure depositions slightly differ in the lattice parameter. This

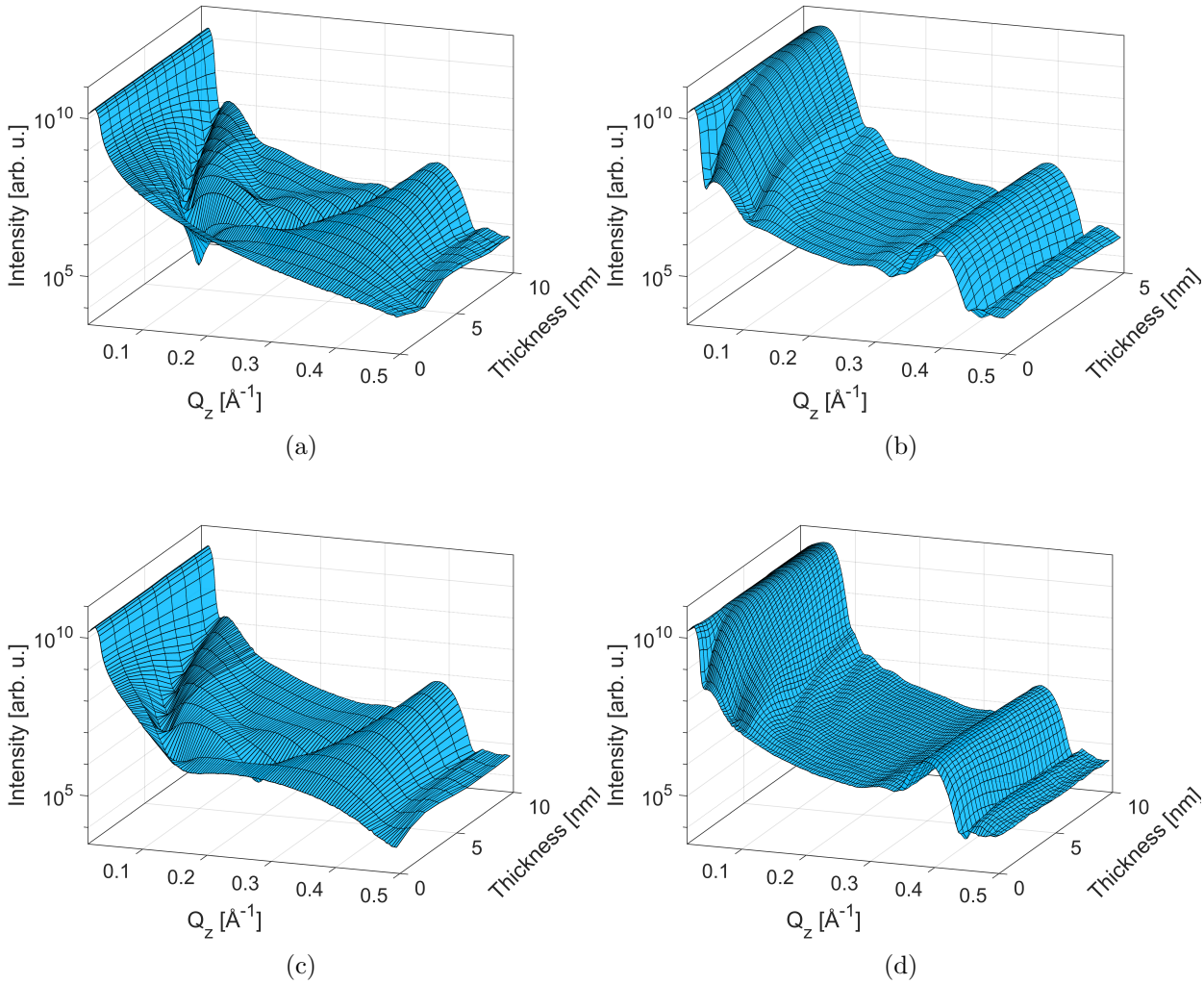

Figure 7.4.: XRR in-situ images of [6]Phenacene films before and after gold deposition on top. The base thickness of the pure film is 10 nm: a) pure, b) 5 nm Au on top, c) pure and d) 10 nm Au on top.

can be mostly explained by different substrate quality, realignment after substrate change as well as fluctuations during thin film deposition leading to small differences in the final structure. However, the overall trend shows a sharp decrease in the lattice parameter during the initial stages of thin film growth as already discovered in Subsection 5.1.1 which can be explained by a strong molecule-substrate interaction in the early growth stages, followed by a dominant molecule-molecule interaction during the later stages of thin film growth. Due to several post-growth measurements after the pure [6]Phenacene deposition as well as the heating up of the gold cell, it took roughly one hour before the deposition with gold was performed. Post-growth changes which could manifest in a shift in the lattice parameter were not observed. However, after a small amount of gold was deposited, a slight decrease of the lattice parameter is observed, which can be explained by the additional gold molecules

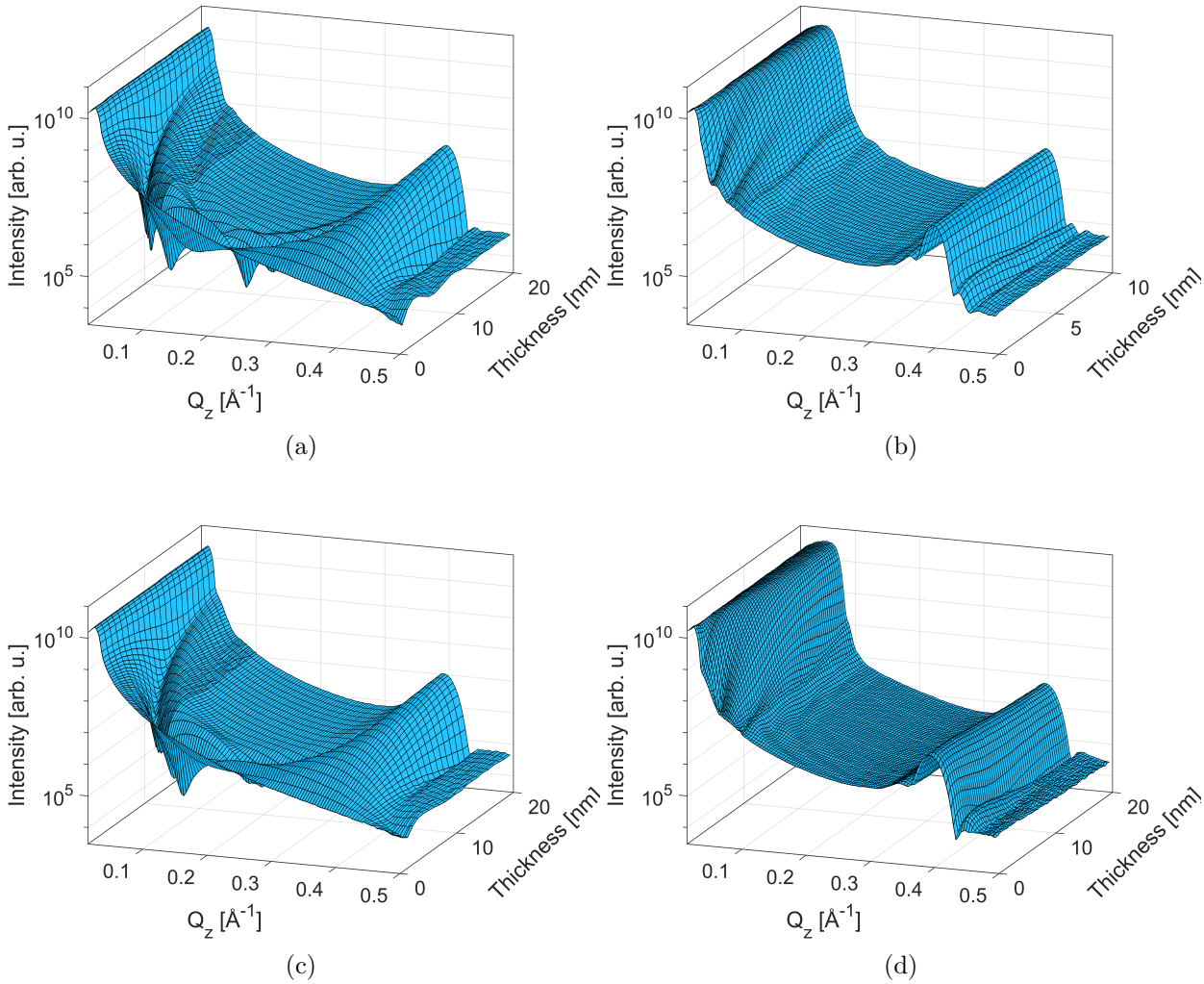

Figure 7.5.: XRR in-situ images of [6]Phenacene films before and after gold deposition on top. The base thickness of the pure film is 20 nm: a) pure, b) 10 nm Au on top, c) pure and d) 10 nm Au on top.

on the thin film surface. The overall trend during gold deposition is a slight increase of the lattice parameter for increasing gold thickness. This can be observed in the 10 nm [6]Phenacene thin films shown in Figure 7.6a. The 20 nm [6]Phenacene thin films in Figure 7.6b show similar behaviour, but after a slight lattice space increase during 10 nm of gold, the lattice parameter seems to decrease again. A possible explanation would be, that there is a strong [6]Phenacene-gold interaction, that influences the molecular packing of the [6]Phenacene thin film closer to the surface of the sample. The change in molecular packing is more pronounced for thinner [6]Phenacene films, as only the upmost part of the film is influenced by a relatively short-ranged interaction with gold.

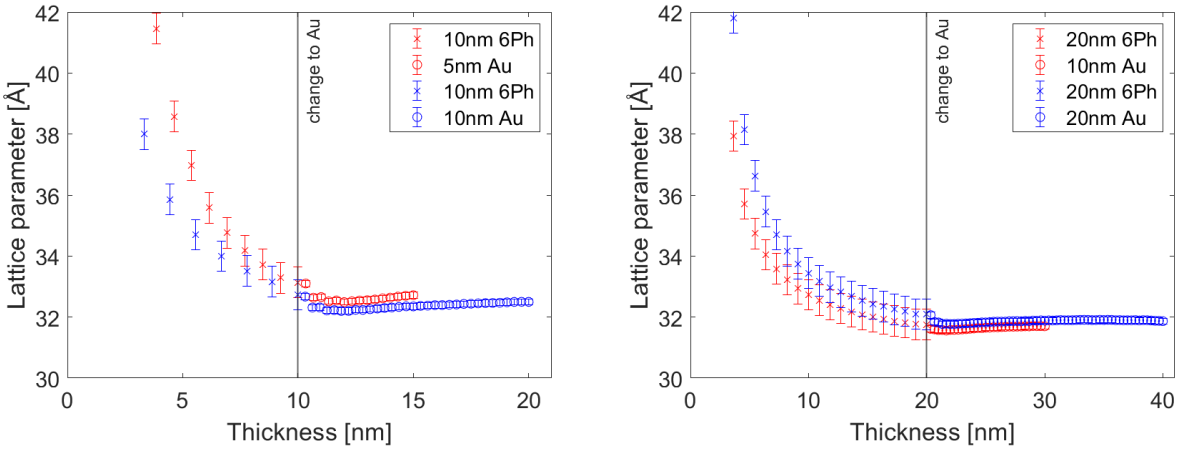

(a) (b)

Figure 7.6.: Lattice parameter calculated from the (002) [6]Phenacene Bragg peak: a) 10 nm films and b) 20 nm films.

Another experiment was performed by depositing [6]Phenacene on top of a thin gold layer. 4 nm of gold was deposited onto a native silicon substrate while measuring in-situ XRR which is shown in Figure 7.7a. The graph shows well-defined Kiessig oscillations over all scans while no Bragg peaks of gold are visible due to the limited measurement range. Afterwards, 10 nm of [6]Phenacene was deposited on top of this film. The measurements are shown in Figure 7.7b showing no changes in the well-defined Kiessig oscillations of the [6]Phenacene thin film.

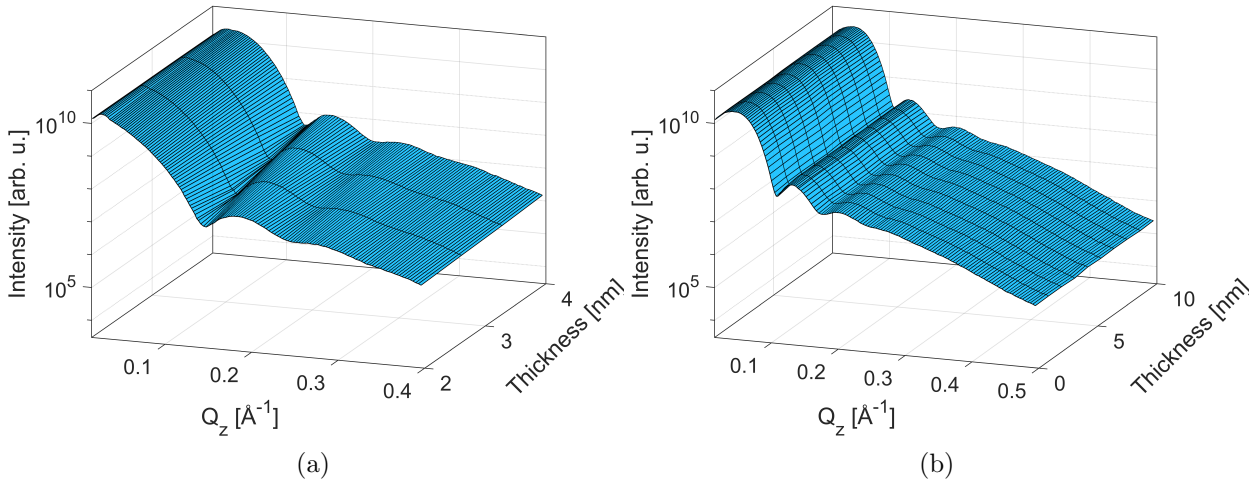

(a) (b)

Figure 7.7.: XRR in-situ images of [6]Phenacene on top of gold: a) base film with Au 4 nm and b) [6]Phenacene 10 nm deposited on top.

An additional measurement was performed after deposition over a wide range of angles as shown in Figure 7.8. There are still no Bragg reflections of [6]Phenacene visible, but a well-defined gold (111) peak is visible at around $q_z = 2.66$ Å^{-1}. Again, this peak was fitted with the same method as described above and a crystallite size of around 160 Å was calculated which is shown in Table 7.5.

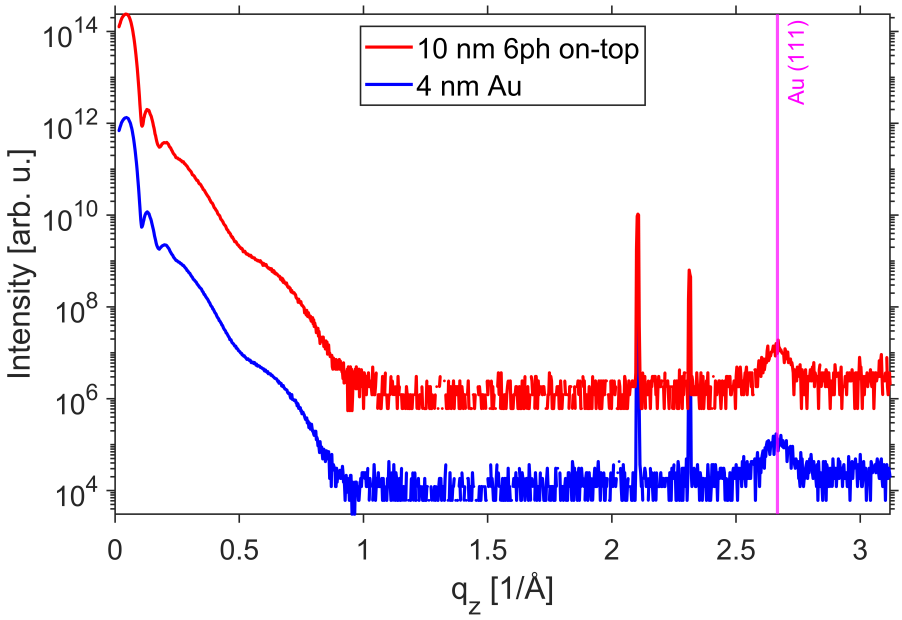

Figure 7.8.: XRR post-growth image of [6]Phenacene on top of gold.

Table 7.5.: Crystallite size derived from the (111) Au peak.

Film	q_{Au} [1/Å]	FWHM [1/Å]	Crystallite size [Å]
4 nm Au	2.66	0.037	169
10 nm 6Ph on top	2.67	0.041	153

7.1.2. In-plane structure

The in-plane structure of the [6]Phenacene thin film with gold deposited on top was investigated using GIWAXS measurements. The previous section showed that there is no change in the thin film structure in the out-of-plane direction. This is consistent with the observations made if the [6]Phenacene thin films were doped by alkali metals for both on-top and co-deposition. The intercalation of dopant atoms only leads to a change in the in-plane direction, as the out-of-plane stacking depends mainly on the length of the [6]Phenacene molecule. Figure 7.9 shows the GIWAXS patterns of [6]Phenacene thin films for which gold atoms were deposited on top for different durations at identical deposition rates. All patterns

show well-defined Bragg reflections. When the Bragg peaks are fitted and subsequently the unit cell parameters calculated, no significant change in the unit cell structure when compared to the pristine [6]Phenacene thin films can be observed. This observation suggests that there is no intercalation of gold atoms into the unit cell of the organic thin film. Instead, the gold layer is formed on top of the surface of [6]Phenacene. This is suggested by a decrease in the intensity of all observed [6]Phenacene peaks due to the attenuation of the signal by a thin layer of gold. As the density of the gold is relatively high, already thin gold layers have a strong impact on the visibility of the Bragg peaks.

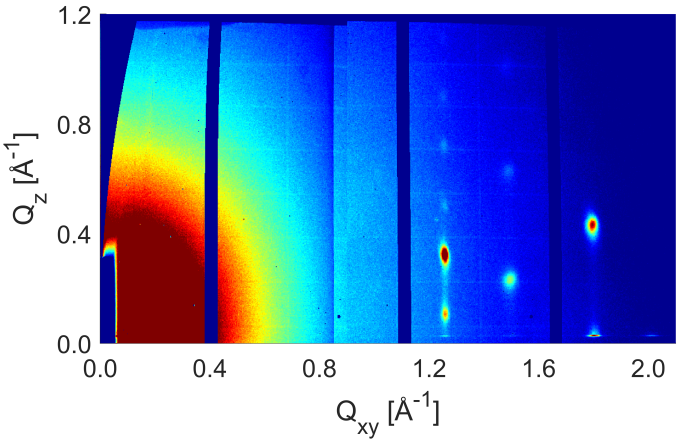

(a)

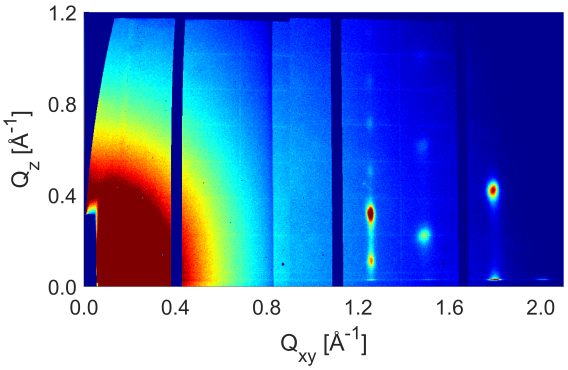

(b)

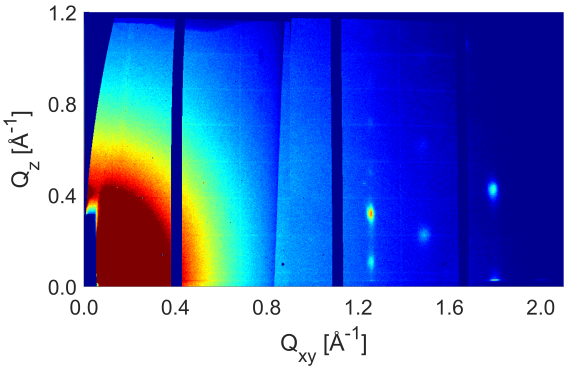

(c)

Figure 7.9.: GIWAXS images of 2 Å/min 20 nm [6]Phenacene films: a) pure film. Gold deposited on top: b) for 60 min and c) 120 min.

To extend the variety of thin films, additional films were grown at the ESRF BM32 beamline while conducting GIWAXS measurements. The overview of the resulting images is shown in Figure 7.10 for a 20 nm base film and Figure 7.11 for a 40 nm base film. These pictures correspond to several thin films discussed in the previous chapter which are shown in Figure 7.3. The results are consistent with the data discussed before. The decrease in intensity due to gold on top of the pure [6]Phenacene thin film can be used as a qualitative measurement of the relative [6]Phenacene and gold content. More [6]Phenacene leads to stronger peaks, while more gold leads to an intensity decrease while the in-plane crystal structure of [6]Phenacene is preserved. Additionally, the Debye-Scherrer ring that corresponds to gold can be seen in the images, which is responsible for the out-of-plane Bragg peak position from the XRR images in the previous chapter. This is a sign of a random orientation of gold on top of the thin film [65, 162, 163].

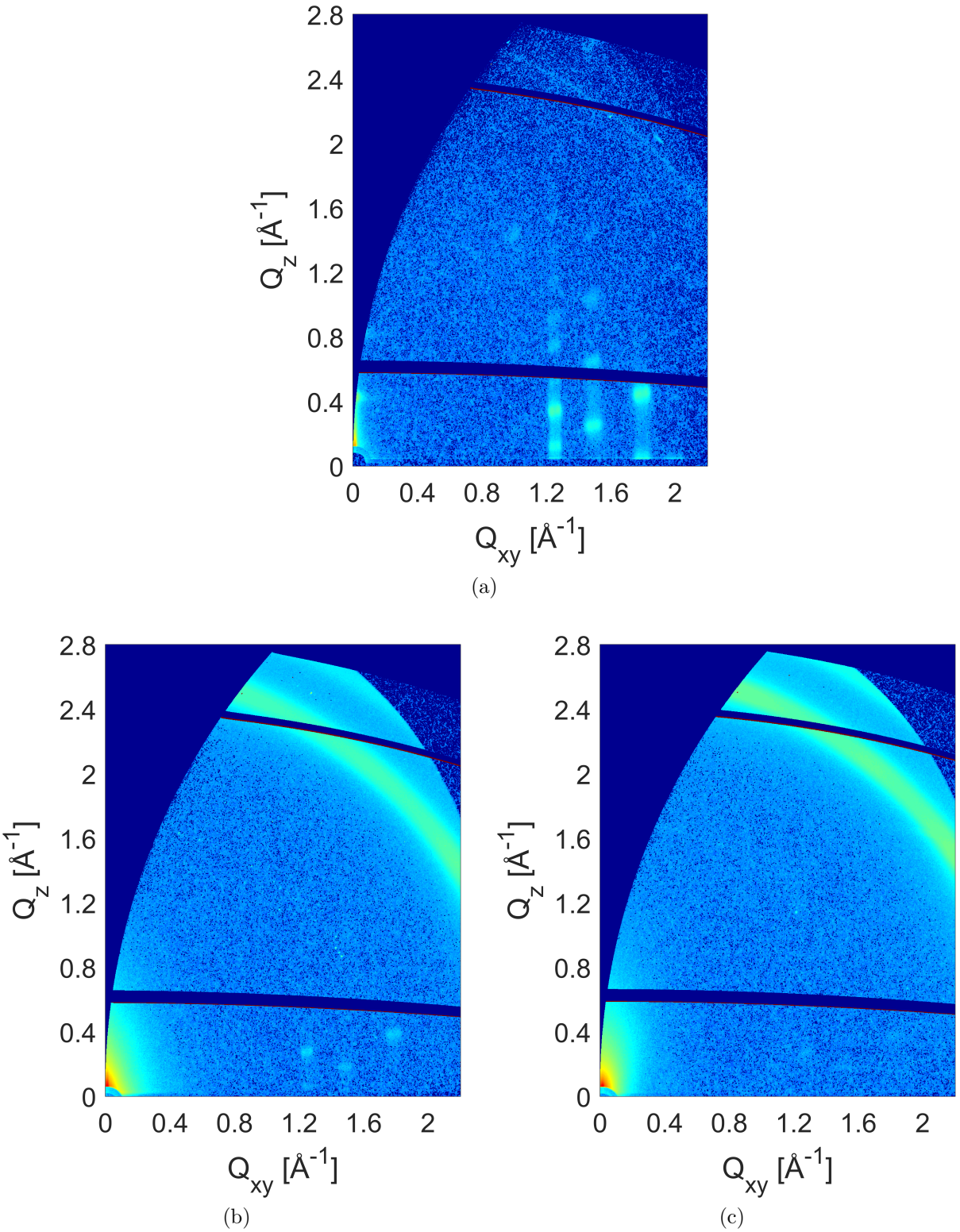

Figure 7.10.: GIWAXS images of 20 nm [6]Phenacene thin films with gold deposition on top: a) pure, b) 10 nm Au on top and c) 20 nm Au on top.

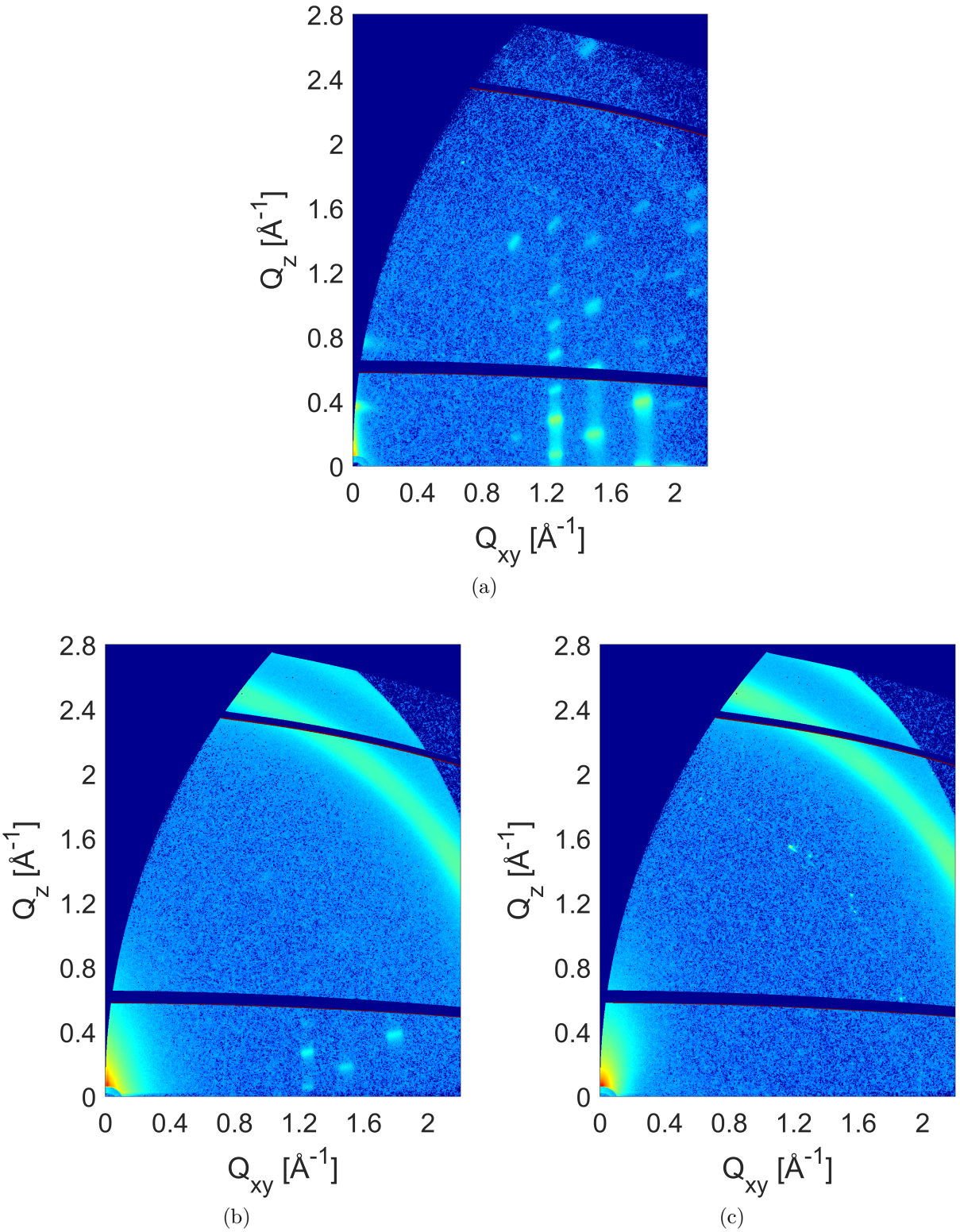

Figure 7.11.: GIWAXS images of 40 nm [6]Phenacene thin films with gold deposition on top: a) pure, b) 10 nm Au on top and c) 20 nm Au on top.

7.2. Morphology

The morphology section will cover the same thin films as discussed in Subsection 7.1.1. Therefore, this section starts with small gold amounts and will then switch to higher gold amounts covering the same films deposited at ESRF BM32. Figure 7.12 shows several 2 Å/min 20 nm [6]Phenacene thin films with various amounts of gold on top. While the pure film shows the already discussed wedding cake morphology, the films with gold on top show small dots on top of those structures. With increasing gold deposition time the wedding cake step edges seem to vanish, indicating that gold atoms are filling the lower levels.

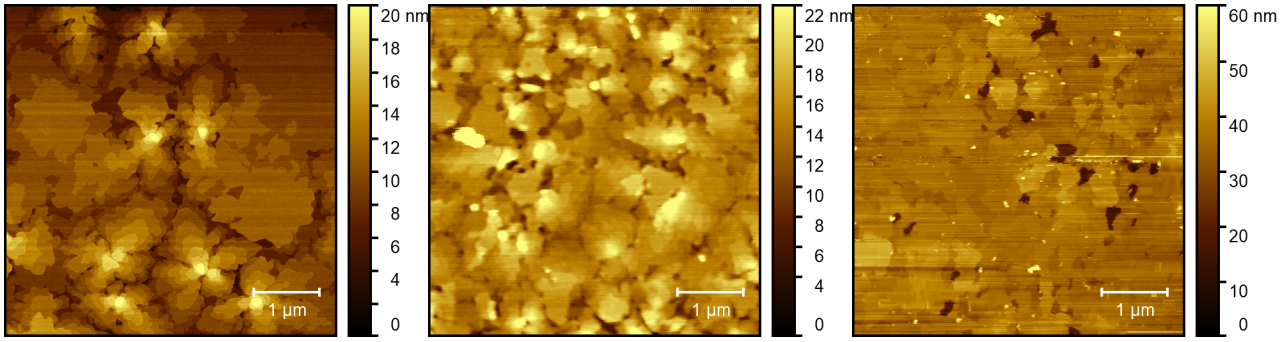

(a) (b) (c)

Figure 7.12.: AFM images (5 × 5 µm) of 2 Å/min 20 nm [6]Phenacene films with gold on top: a) pure, b) Au 30 min and c) Au 60 min.

The RMS roughness was extracted with Gwyddion by using the complete image. The results and comparison with the corresponding XRR images are shown in Figure 7.13 showing a roughness increase from 2.34 nm (pure) to 5.00 nm (60 min) which contradicts the XRR measurements taken in the previous chapter. This can be explained by the time gap between thin film deposition and XRR/AFM measurement. While XRR measurements were taken shortly after deposition, the AFM measurements were taken later, leading to a gap of several days or even weeks which could induce post-growth roughness changes between those two measurements. Another explanation would be artefacts during the AFM measurement. Figure 7.12c looks smoother than the rest but has a higher calculated roughness. This can be caused by calculation errors due to artefacts or the different image scaling that was necessary to get a contrast-rich image.

Experiments with higher amounts of gold deposited were conducted at ESRF BM32. Figure 7.14 shows 10 and 20 nm pure [6]Phenacene thin films with on-top gold deposition of 5 to 20 nm that have been measured several weeks after the experiment. The AFM images look similar to the deposition of pure [6]Phenacene forming islands with a wedding cake structure. However, depending on the gold amount on top, the terraces are not well defined anymore and can only be suspected in the AFM images. Again, the RMS roughness

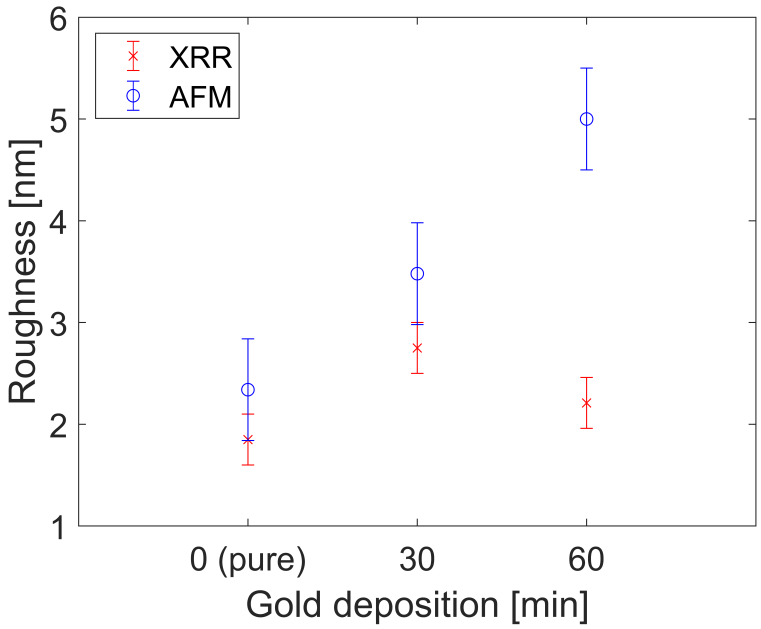

Figure 7.13.: Comparison between roughness values gained from XRR and AFM measurements.

was extracted with Gwyddion by using the complete image and additionally the correlation length was calculated which describes the mean island distance of the thin film. The results together with an XRR comparison are shown in Figure 7.15.

One thing that can be depicted from the roughness calculations (Figure 7.15a) is the thickness dependence of [6]Phenacene with 20 nm thin films showing a higher roughness than 10 nm films as already described in Chapter 5. By depositing gold on top of these films, the 10 nm films show an increase in roughness while 20 nm shows a slight decrease. This effect can be explained by gold atoms covering the surface, leading to a roughening of the original film, as well as gold atoms filling the gaps between the wedding cake islands, leading to a smoother structure. This effect is thickness-dependent. However, the XRR data that has been acquired directly after deposition exhibit a slight smoothing in both cases, indicating both effects seem to occur with gap filling as the more prominent one. It has to be mentioned that the XRR fits had a high error, especially at a higher gold thickness, which was caused by limitations in the used fitting model. Also, post-growth behaviour cannot be fully excluded for the AFM images due to the longer time period between film deposition and measurement. The correlation length is shown in Figure 7.15b indicating that gold deposition leads to a decrease in island distances. This can be explained by gap filling and therefore new island formation on top of the thin film.

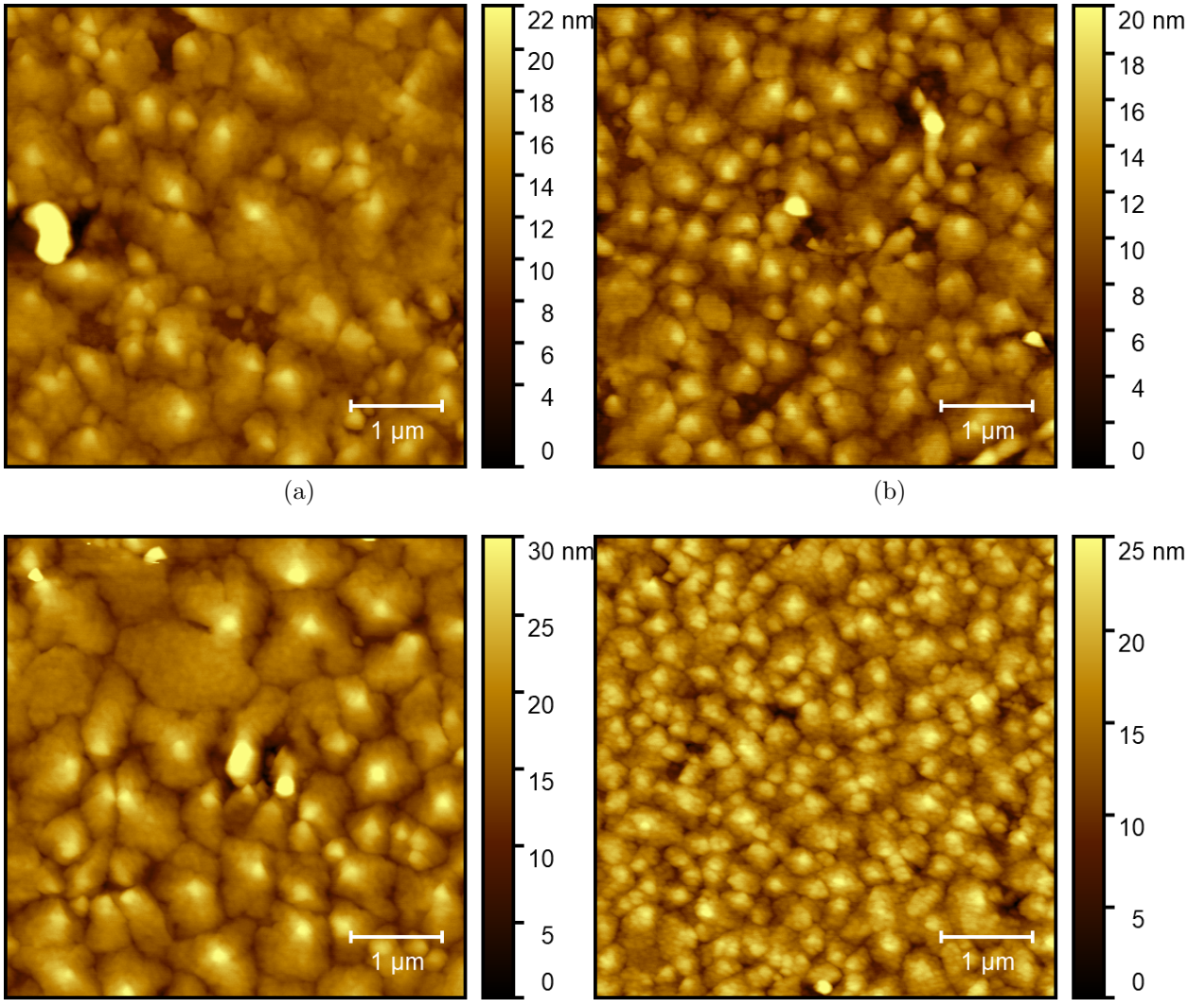

Figure 7.14.: AFM images (5×5 µm) of [6]Phenacene films with gold on top: a) 10 nm [6]Ph 5 nm Au, b) 10 nm [6]Ph 10 nm Au, c) 20 nm [6]Ph 10 nm Au and d) 20 nm [6]Ph 20 nm Au.

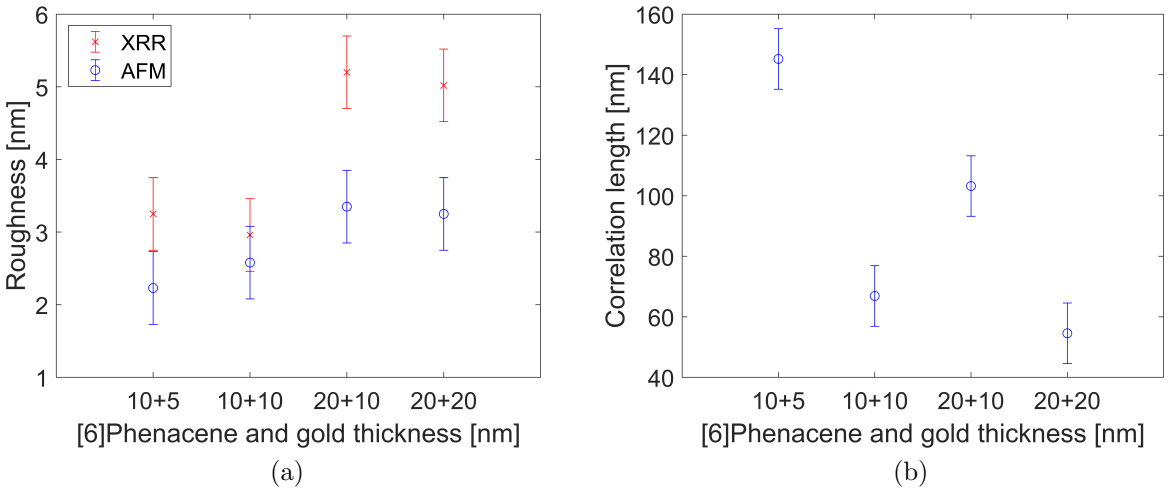

(a) (b)

Figure 7.15.: a) Roughness comparison of XRR/AFM and b) correlation length from AFM.

Another experiment was performed by depositing gold onto a silicon substrate and then [6]Phenacene afterwards on top of it. The resulting AFM image is shown in Figure 7.16. The image shows a smooth layer with elongated grains of different sizes on top of it. By applying the same evaluation methods as above, an RMS roughness of 21.6 nm and a correlation length of 112.6 nm was found.

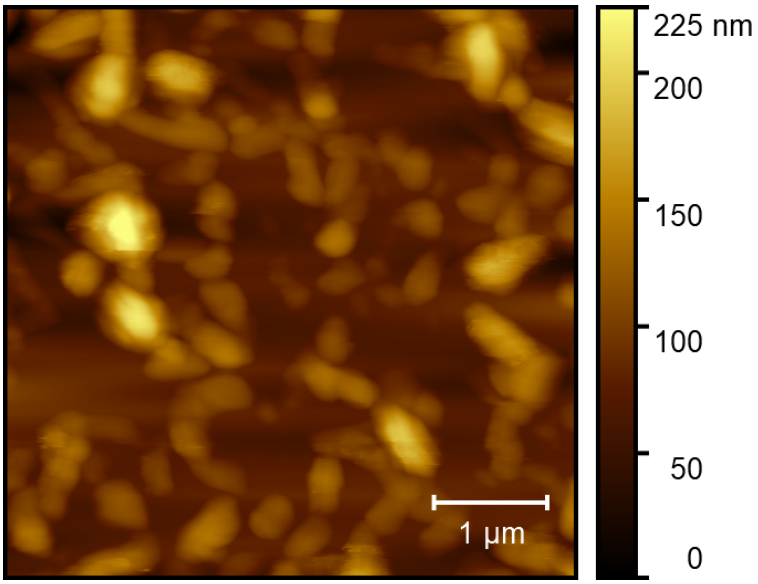

Figure 7.16.: AFM image (5×5 µm) of 10 nm of [6]Phenacene on top of 4 nm of gold.

7.3. XPS

XPS measurements were performed to check the success of gold deposition on top of [6]Phenacene thin films. An overview scan over the energy range from 0 to 1000 eV was performed and is shown in Figure 7.17. The corresponding gold peaks (Au 4p, 4d and 4f) as well as the silicon (Si 2p), oxygen (O 1s) and carbon (C 1s) from the substrate and the organic thin film were marked in the spectra. Additional region scans of those peaks were performed for further evaluation.

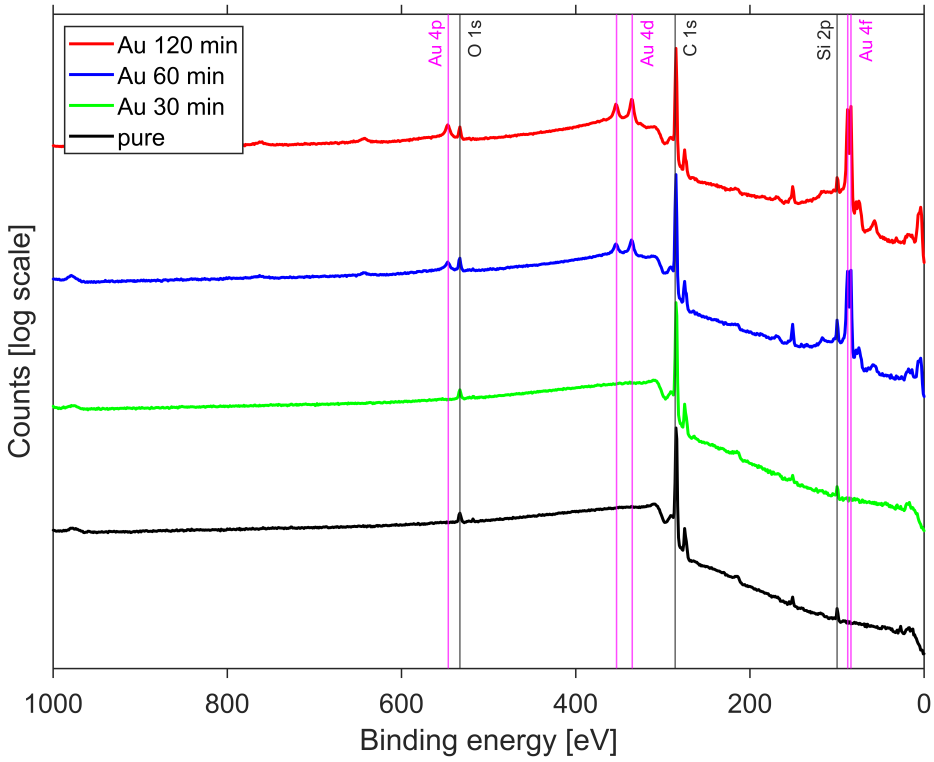

Figure 7.17.: XPS spectra of [6]Phenacene thin films with gold on top.

As expected, gold peaks are visible and increase in intensity with the gold deposition time. The films are also free of other contaminants. Due to the surface sensitivity of XPS, it was possible to check the gold location of one thin film by tilting the sample by 45° and measuring the spectra again. Both spectra are shown in Figure 7.18.

By fitting the corresponding gold and carbon peaks with a Gaussian, the area values were extracted and it was possible to calculate the average ratio between carbon and gold. Table 7.6 shows the results.

While the ratio between 0° to 45° shows differences for the gold peaks, the carbon peak stays nearly constant. This behaviour can be explained by scattered gold clusters on top of the carbon layer which were visible in the previous AFM measurements. Therefore the

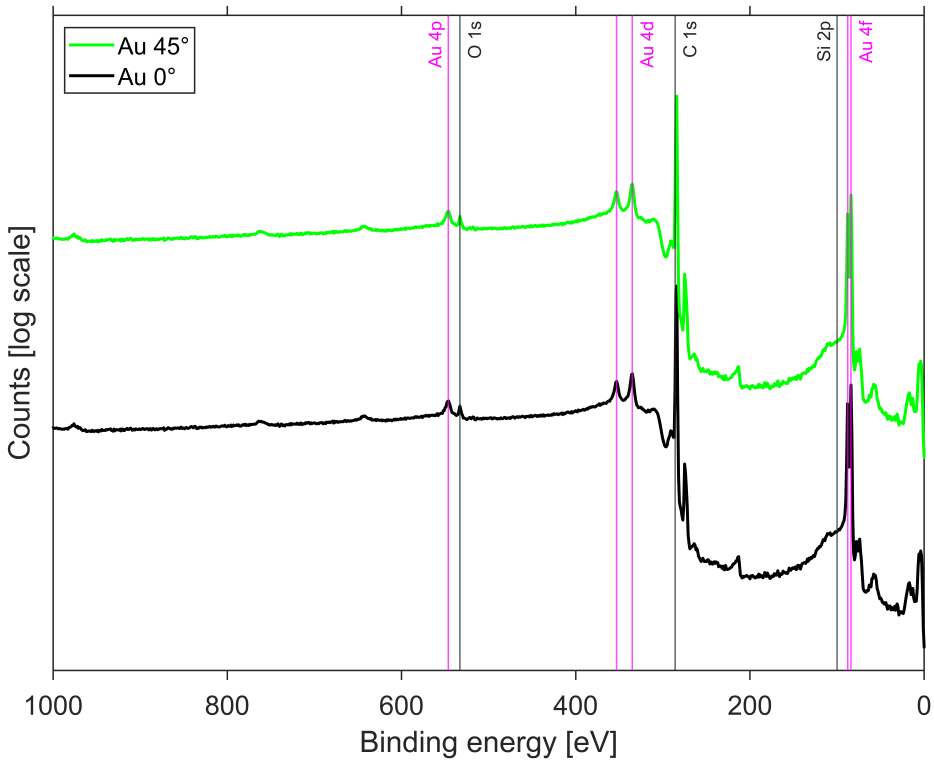

Figure 7.18.: XPS spectra of [6]Phenacene and gold on top. Different measurement angles were used.

Table 7.6.: Calculations of the intensity ratio under different measurement angles.

Au film angle	Au 4d	Au 4f 5/2	Au 4f 7/2	C 1s
0°	48884	36161	57059	375149
45°	81663	52977	82194	362105
Ratio	0.60	0.68	0.69	1.04

attenuation of the carbon signal due to gold stays minimal. For further confirmation, the thickness of the gold layer is needed which is difficult to measure with XRR because the layer is not completely filled. It is possible to approximate the gold thickness by comparing the carbon intensity values with increasing gold deposition time. More gold leads to an increasing attenuation in the carbon peak intensity. It has to be mentioned that this calculation only leads to an effective thickness which cannot fully describe the coverage and morphology of the layer. Therefore differences in thicknesses measured by other methods can occur due to the surface sensitivity of XPS. By using Equation 4.18 with the inelastic mean free path $\lambda_s = 16.2$ Å for the C 1s peak in gold it was possible to approximate the gold thickness which is shown in Table 7.7. The results show very small values from 0.2 up to 3.53 Å which can explain the previously noticed carbon attenuation behaviour.

Table 7.7.: Calculation of the thickness increase by using the area value of the C 1s peak intensity.

Au deposition time	C 1s	Thickness increase [Å]
pure	437777	-
30 min	432296	0.20
60 min	385167	2.07
120 min	351955	3.53

7.4. Discussion

The crystal structure and morphology of the organic-inorganic hybrid system of [6]Phenacene combined with gold, grown on native silicon substrates, were investigated. The gold deposition was performed on top of pure [6]Phenacene thin films. The resulting thin films were investigated using real-time XRR measurements during deposition, supplemented with additional GIWAXS, AFM and XPS post-growth measurements.

When small amounts of gold are deposited on top of a [6]Phenacene layer, its thin film structure stays intact, showing well-defined [6]Phenacene Bragg reflections in the out-of-plane direction. Slight roughness changes with roughening after several minutes of deposition and smoothing at longer deposition times were observed. AFM measurements showed that gold is visible as small grains on top of the [6]Phenacene wedding cake surface. With increasing gold deposition time, the wedding cake step edges seem to vanish, which is an indication that gold atoms are filling the gaps between the terraces. These scattered gold clusters on top of the [6]Phenacene layer were also observed by XPS measurements. The suspected growth behaviour of gold is depicted in Figure 7.19.

Further depositions of gold on top of [6]Phenacene were performed with higher gold amounts while measuring in-situ real-time XRR measurements during deposition. The results showed that the overall crystallinity of the organic thin film stays intact, while the films get slightly rougher. Higher-order [6]Phenacene Bragg peaks get slightly attenuated when gold is deposited on top of the thin film, especially at low [6]Phenacene and high gold thicknesses. The higher gold amount also leads to a visible gold (111) Bragg reflection that is getting more pronounced for higher gold thicknesses. Lattice parameter changes were already observed after a small amount of gold, which can be explained by the additional gold molecules on the thin film surface. A slight lattice parameter decrease was observed after 10 nm of gold on top which can be possibly explained by a strong [6]Phenacene-gold interaction, that influences the molecular packing of the [6]Phenacene thin film closer to the surface of the sample. This effect was more pronounced for thinner [6]Phenacene films, as only the upmost part of the film was influenced by the relatively short-ranged interaction with gold. The GIWAXS measurements showed well-defined Bragg reflections for [6]Phenacene thin

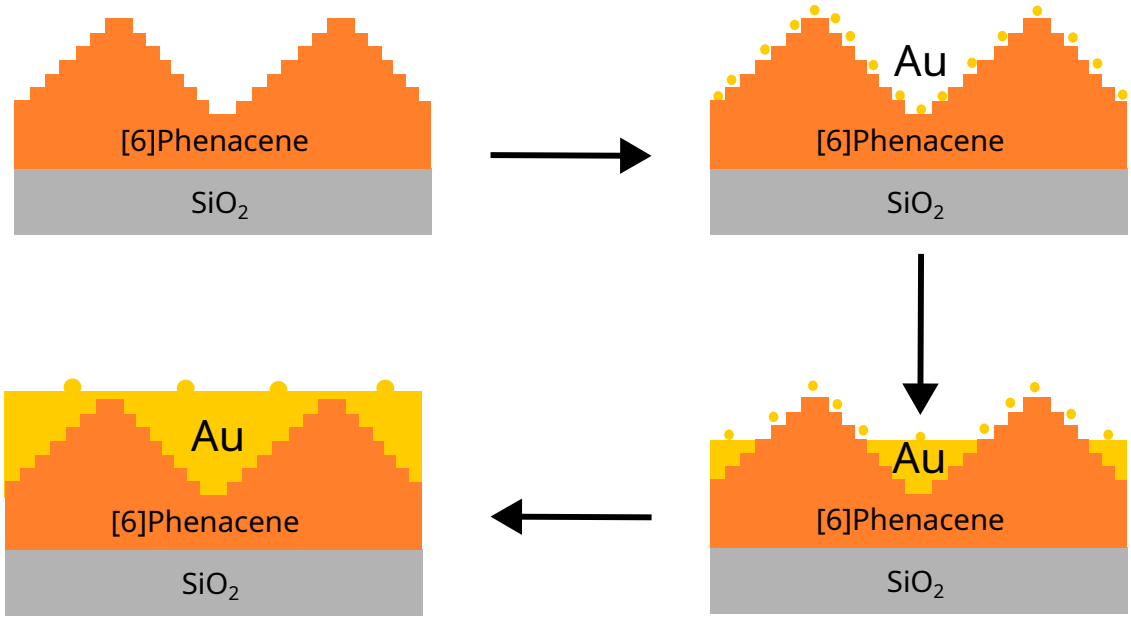

Figure 7.19.: Growth behaviour when gold is deposited on top of [6]Phenacene. Gold leads to a roughness increase due to the additional molecules on top of the surface. With increasing gold thickness, the lower levels of the wedding cake are filled, leading to a smoother film.

films with gold on top. The unit cell parameters were calculated and no significant change in the unit cell structure was found therefore no indication of gold intercalation into the organic unit cell is found. Additionally, a decrease of all observed [6]Phenacene Bragg peaks was found due to the attenuation of the signal by the gold layer. This effect is also present in thin gold layers, due to the high density of gold. A Debye-Scherrer ring that corresponds to gold can be seen in the GIWAXS images, which is also responsible for the out-of-plane Bragg peak position in the XRR images. This is a sign that gold atoms form randomly oriented domains on top of the thin film. AFM measurements showed remains of the pristine [6]Phenacene wedding cake structure, which was not well defined anymore due to the additional gold atoms on top of the thin film. Gold deposition on top of the pristine thin film leads to a gap filling between the wedding cake islands and the new island formation on top, which was already shown in Figure 7.19. The exact gold cluster growth can only be presumed. Metals on top of most oxide and organic surfaces, grow in form of 3D islands rather than in a layer-by-layer growth mode due to their non-wetting behaviour [164], but also deviations for several combinations of oxide surfaces and metals were observed [165]. In this case, the nucleation of small gold clusters was observed, followed by the filling of the wedding cake terraces. A possible explanation would be the nucleation of gold clusters on the [6]Phenacene wedding cake terraces, followed by a slight lateral growth. After a certain thickness, the growth translates into a coarsening stage, followed by a vertical growth stage as observed by Kaune et al. [166]. However additional in-situ GISAXS measurements would

be needed to confirm this behaviour.

The observation that the atoms of gold, when deposited on top of the already present [6]Phenacene layer, are located at the sample surface instead of intercalating into the organic thin film is consistent with experiments done with on-top deposited alkali metals. It is suspected that additional energy is required to disturb the organic thin film to allow atoms to penetrate into the sample. As a reminder, the intercalation of potassium atoms was observed by Roth et al. for both tetracene and pentacene at similar deposition conditions using the same alkali metal dispensers [42]. Additionally, the atoms of gold are relatively large. When compared to the alkali metal caesium it is expected that a phase separation, rather than a proper mixture would be observed even when gold would be co-deposited together with the molecules of [6]Phenacene based on their geometric incompatibility [167].

[6]Phenacene was deposited on top of a thin gold layer that was deposited onto a native silicon substrate. XRR scans showed well-defined Kiessig oscillations over all scans, while no Bragg peaks of [6]Phenacene were visible anymore, indicating that the out-of-plane crystallinity for [6]Phenacene is lost. The gold (111) Bragg reflection is visible. AFM measurements showed a smooth layer with elongated grains. These results show that the choice of growth order is important due to significant structural changes in the thin film.

Part IV.

Summary and outlook

8. Summary and outlook

This thesis investigated the growth and morphology of organic-inorganic interfaces by comparing data from various techniques and different samples. To approach the problem of post-growth changes in thin film structure and morphology, also in-situ real-time methods were used to measure the thin film during the growth process. A high image resolution and image quality were needed, therefore synchrotron X-ray sources with a high photon flux as well as modern 2D area detectors were used to achieve this. The understanding of growth and morphology is an important topic due to their influence on optical and electronic properties, therefore if possible the measurements were concluded with optical measurements. This chapter is divided into three parts, respective to the results chapter, the summary starts with pure [6]Phenacene thin films and will then continue to summarize alkali metal doped followed by gold doped [6]Phenacene thin films. Afterwards, this section is concluded with an outlook where possible further projects and ideas will be discussed.

8.1. Pure [6]Phenacene thin films

A comprehensive understanding of the pure [6]Phenacene thin film growth behaviour was gained by investigating the growth with real-time XRR and GIWAXS measurements during deposition as well as combining these results with AFM and optical measurements. A schematic representation of the pure [6]Phenacene result is shown in Figure 8.1. The unit cell structure and orientation was calculated and compared with other Phenacenes.

- Growth behaviour of [6]Phenacene shows layer-by-layer and then island growth (Stranski-Krastanov). The critical thickness, where the transition from layer-by-layer to island growth occurs is probably two monolayers.

- The overall morphology gained by AFM measurements shows wedding cake islands with a terrace height that corresponds to the length of one [6]Phenacene molecule.

- The roughness behaviour is thickness-dependent (indication for mild rapid roughening) and the film configuration (lattice parameter) shows only slight changes after 15 nm. This thickness-dependent behaviour is caused by a high interaction between molecules

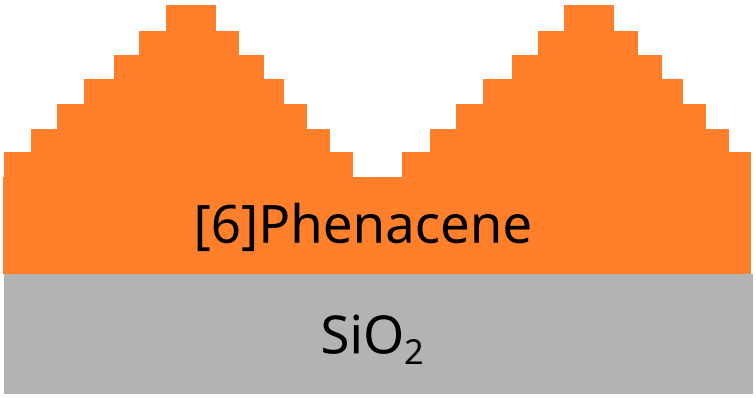

Figure 8.1.: Overview of [6]Phenacene thin film growth. Growth begins with layer-by-layer growth. After a certain thickness, it translates into island growth. This growth mode is called Stranski-Krastanov growth. The resulting islands are called wedding cake islands.

and substrate at the beginning of the growth, which changes to a molecule-molecule interaction after a few monolayers.

- The unit cell structure and orientation of [6]Phenacene was calculated by using four molecules inside a unit cell. Similarities to other Phenacene molecules were found. The molecule stacking seems to depend on the parity of the conjugated core. Therefore [7]Phenacene was also investigated which showed two polymorphs that are similar to [5]Phenacene. The only differences between Phenacenes were found in the unit cell parameters c and β.

- Optical UV/vis/NIR measurements showed a vibronic progression and similar results to the solution spectra of [6]Phenacene. Due to the asymmetric molecular structure (rod-like shape), different optical properties are found based on the direction of incoming light. VASE measurements showed a dominant k_z component which indicated that the transition dipole moment is oriented perpendicular to the substrate surface.

8.2. Alkali metal doped [6]Phenacene thin films

Thin films of [6]Phenacene were deposited together with either potassium, rubidium or caesium alkali metals. The alkali metal deposition was done either after the deposition of the pure film (on-top deposition) or during the deposition of [6]Phenacene (co-deposition). XPS was used to check the success of the alkali metal deposition after deposition as well as checking against contaminations from other alkali metals that were used in the chamber before. The gained XPS spectra were also used to get an estimation of the molecules inside the thin film, which was used for the calculation of the orientation of the molecules inside the unit

cell. The growth of potassium and rubidium together with [6]Phenacene was investigated by using real-time in-situ XRR at ESRF ID10 and DESY P23. All results were combined with additional post-growth XRR, GIWAXS, AFM, SEM and absorption data.

- On-top alkali metal deposition shows a high crystallinity and no change in the unit cell structure. No intercalation into the thin film was observed (see Fig. 8.2). The alkali metal deposition leads to an overall attenuation that dampens the intensity of the observed Bragg reflections and also leads to various roughness changes due to the additional molecules scattered on the surface.

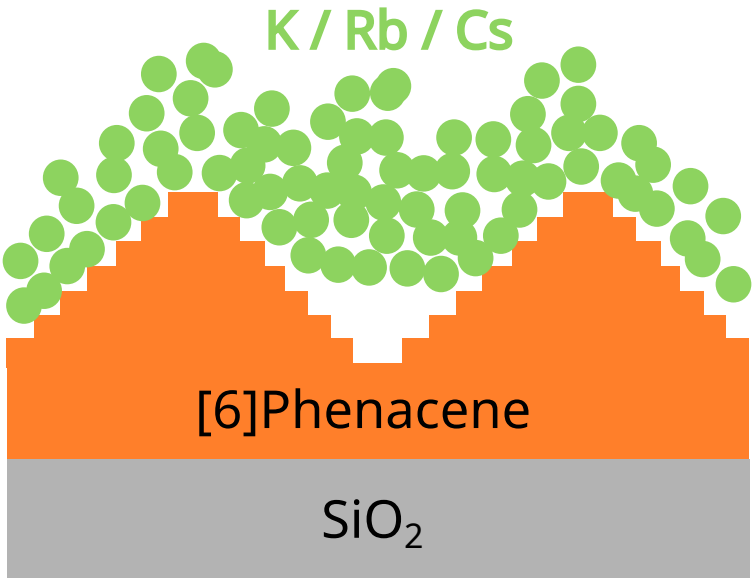

Figure 8.2.: Overview of [6]Phenacene on-top alkali metal deposition. Alkali metals stay on top and no intercalation into the thin film was observed.

- Co-deposition leads to a decreasing or even complete loss of the out-of-plane crystallinity. Caesium leads to phase separation, while potassium and rubidium change the unit cell orientation to accommodate the additional alkali atoms inside the unit cell. The results are shown in Figure 8.3. It was possible to calculate the unit cell of potassium and rubidium co-deposited with [6]Phenacene. The molecular orientation was only calculated for potassium co-deposited with [6]Phenacene.

- The size of the dopant has to be considered, as big dopants like caesium can not intercalate into the unit cell and therefore lead to phase separation. Bigger dopants like rubidium showed a higher misorientation in the [6]Phenacene unit cell structure than potassium.

- The morphology depends mainly on the doping method. On-top deposition leads to a new layer on top of the already existing wedding cake structure that can be assumed underneath, while co-deposition leads to a completely new island structure with island sizes and distances depending on the used alkali metal.

- Optical UV/vis/NIR measurements of the on-top doped thin films showed similar results as the pure [6]Phenacene thin film except for slight intensity changes. However, the co-deposition with potassium and rubidium showed intensity as well as peak changes which means that the optical properties are altered. Caesium co-deposition shows no such changes. This can be explained by potassium and rubidium molecules changing the unit cell which alters the optical properties, while caesium co-deposition only leads to phase separation.

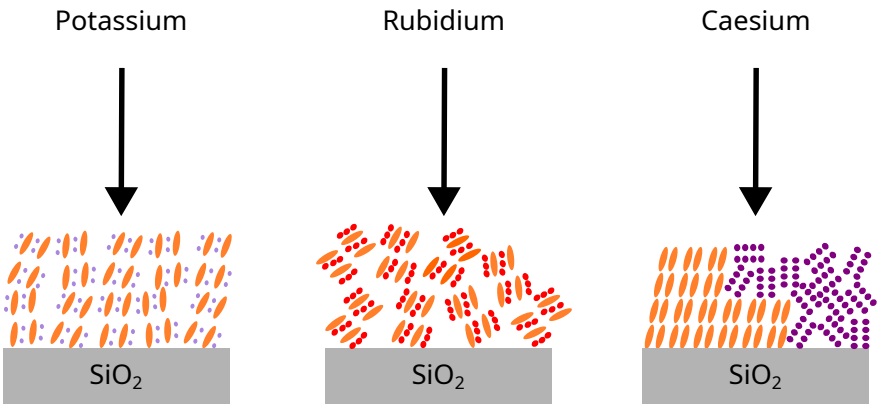

Figure 8.3.: Overview of [6]Phenacene and alkali metal co-deposition. Potassium and rubidium intercalate into the [6]Phenacene unit cell, leading to a slight misorientation. Caesium leads to phase separation.

8.3. Gold doped [6]Phenacene thin films

Thin films of pure [6]Phenacene with gold on top were grown. First depositions and measurements were performed in the home laboratory. XPS was used to check the deposition success, ensure a contaminant-free deposition as well as check the location of the gold, showing that gold is on top of the [6]Phenacene layer. At ESRF BM32 the growth of [6]Phenacene and the subsequent deposition of gold on top was investigated by using real-time in-situ XRR. Additionally, [6]Phenacene was deposited on top of a gold layer. All results were combined with additional post-growth XRR, GIWAXS and AFM data. Figure 8.4 shows an overview image of gold on top of [6]Phenacene.

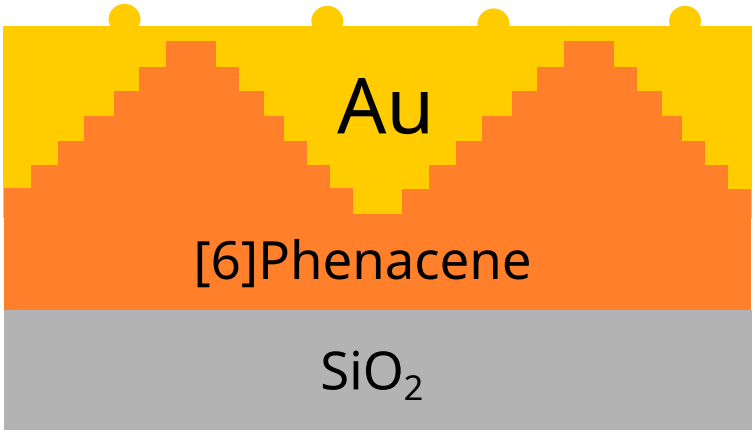

Figure 8.4.: Overview of gold on top of a [6]Phenacene thin film. With increasing gold thickness, the space between the wedding cake islands is filled and additional gold islands are visible on top.

- When gold is deposited on top of [6]Phenacene its crystal structure stays intact. Slight roughness changes are found, starting with roughening at the beginning of the deposition and ending with smooth films depending on the gold thickness. This behaviour can be explained by gold atoms on top of the [6]Phenacene molecule. With increasing thickness, the atoms fill the gaps of the wedding cake islands, which then leads to smoothening.

- Gold is visible as small grains on top of the thin film surface. With increasing gold thicknesses the wedding cake step edges vanish, indicating that gold atoms are filling the lower levels. The morphology of higher thicknesses shows an island structure with a roughness and correlation length depending on the [6]Phenacene and gold amount.

- In-situ real-time experiments showed lattice parameter changes. These changes were more pronounced for thinner [6]Phenacene thin films. A strong [6]Phenacene-gold interaction may be present that influences the molecular packing of the [6]Phenacene thin film closer to the surface of the sample, as only the upmost part of the thin film was influenced by the relatively short-ranged interaction with gold.

- The unit cell parameters of [6]Phenacene with gold on top showed no significant changes, indicating, that no gold intercalation into the organic unit cell happens.

- When [6]Phenacene is deposited on top of gold, the [6]Phenacene Bragg peaks vanish, indicating a lost out-of-plane crystallinity. This is a reminder that the choice of growth order is important due to its significant structural change in the resulting thin film.

8.4. Outlook

The data presented in this thesis has led to a series of conclusions that are helpful for understanding the growth of organic and organic/inorganic thin film interfaces. While the goal of this work was concluded, several new questions arose during the data evaluation and subsequent interpretation which can be further explored in future projects.

- In this work, the deposition of alkali metals on top of [6]Phenacene thin films did not lead to the intercalation of these metals into the unit cell of the organic thin film. This is contrary to already published literature, where the deposition of dopants leads to the mixing of organic-inorganic compounds [42] when using tetracene and pentacene as materials. It would be interesting to explore the reason behind the difference in our observations. One possible direction would be post-deposition annealing to improve the ability of dopant atoms to intercalate into the organic thin film.

- While it is expected, that the difference in the mixing behaviour of alkali metals and [6]Phenacene depends on the size of used alkali atoms, further study is necessary to fully confirm and explain this observation. The substrate temperature may influence the mixing behaviour. The co-deposition of caesium together with [6]Phenacene at higher substrate temperatures may lead to the intercalation of alkali metal atoms into the organic thin film instead of the phase separation that was observed in this thesis.

- Only one specific concentration of alkali metal dopants was used due to the challenging film preparation to increase reproducibility. However, it can be expected that the different ratios of alkali metal atoms per [6]Phenacene molecule can lead to slight differences in the thin film structure and therefore in (opto)electronic properties. The influence of different dopant concentrations and their impact on the thin film structure can be studied to optimize the (opto)electronic properties of [6]Phenacene thin films.

- Additional in-situ real-time GISAXS measurements of gold and [6]Phenacene could offer insight into the time evolution of the gold cluster morphology in the early growth stages.

- This work only deals with the thin film structure changes induced by alkali metal doping and gold deposition. To further explore the impact of this method, charge carrier mobility measurements could be employed to quantify the changes in the organic thin film conductivity.

- Another method to deposit gold on top of thin films is the usage of gold nanoparticles that offer different growth dynamics and can therefore change the resulting thin films drastically.

Part V.

Appendixes

9. Additional data and comments on pure [6]Phenacene thin films

This section covers additional data from the results of Chapter 5. The ellipsometry part was taken from the supplementary part of the publication [89].

9.1. Crystal structure

All thin films in every section were evaluated by using the software GenX [113] which uses the Parratt formalism. A simple box model was used that uses a completely filled layer of [6]Phenacene on top of a silicon substrate with native oxide. This model worked perfectly for pure [6]Phenacene thin films and showed a function of merit (FOM) of 0.016 (the lower the better) which is a measurement method for the deviation between the measured and the simulated XRR graph. Figure 9.1 shows an exemplary GenX fit of 40 nm of [6]Phenacene that was used in Section 5.1.1. However, when used for alkali metal doped or gold on top of [6]Phenacene thin films this model reached its limits which resulted in a higher error.

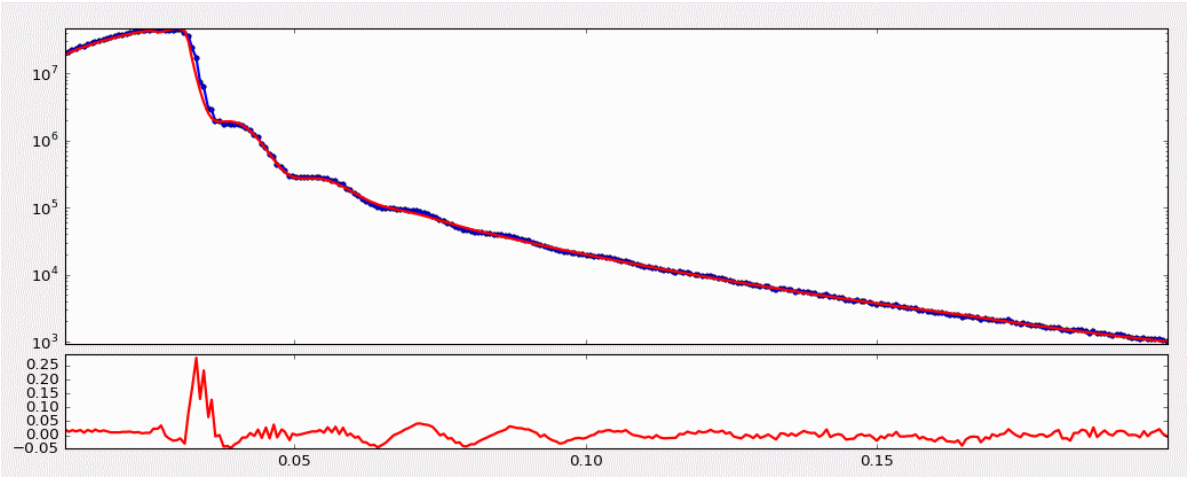

Figure 9.1.: Exemplary GenX fit of 40 nm of [6]Phenacene. A screenshot was taken out of the software. The vertical axis shows the intensity, while the horizontal axis shows the current Q_z in 1/Å. The blue line shows the data whose current fit is shown by the red line. The deviation from the fit is shown in the lower red line.

9.2. Molecular orientation

The results of the molecular orientation calculated in Section 4.4.4.2 were stored in a crystallographic information file (CIF). This file contains all the atomic positions and molecular orientations and can be opened with a text editor or visualised with programs like Mercury [101]. The syntax of a CIF file is described in Chapter 2.2 of the book [168]. In general, the file starts with the unit cell values, followed by the atomic positions for each atom. The contents of the CIF file are parsed below.

```
data_
loop_
_symmetry_equiv_pos_site_id
_symmetry_equiv_pos_as_xyz
1 x,y,z
_cell_length_a 32
_cell_length_b 6.216
_cell_length_c 8.348
_cell_angle_alpha 90
_cell_angle_beta 98
_cell_angle_gamma 90
_cell_volume 1644.3573
loop_
_atom_site_label
_atom_site_type_symbol
_atom_site_fract_x
_atom_site_fract_y
_atom_site_fract_z
C1 C 4.178498e-01 1.274077e-01 4.882558e-03
C2 C 4.399994e-01 2.889610e-01 9.236326e-01
C3 C 4.204333e-01 4.633284e-01 8.411935e-01
C4 C 3.820171e-01 4.756694e-01 8.418462e-01
C5 C 3.585087e-01 3.114860e-01 9.273163e-01
C6 C 3.783413e-01 1.353438e-01 7.856064e-03
C7 C 3.554832e-01 9.659816e-01 9.592320e-02
C8 C 3.174244e-01 9.765734e-01 1.080455e-01
C9 C 2.959158e-01 1.546082e-01 2.988037e-02
C10 C 3.178316e-01 3.202469e-01 9.376844e-01
C11 C 2.967551e-01 4.942280e-01 8.603793e-01
```

```
C12 C 2.584224e-01 5.047023e-01 8.722934e-01
C13 C 2.356970e-01 3.424682e-01 9.646728e-01
C14 C 2.560767e-01 1.658302e-01 4.343254e-02
C15 C 2.332044e-01 9.992827e-01 1.363542e-01
C16 C 1.952309e-01 9.450114e-03 1.476487e-01
C17 C 1.737066e-01 1.866806e-01 7.223921e-02
C18 C 1.950682e-01 3.544885e-01 9.803320e-01
C19 C 1.755007e-01 5.288520e-01 8.978836e-01
C20 C 1.370845e-01 5.411929e-01 8.985364e-01
C21 C 1.135800e-01 3.770115e-01 9.840097e-01
C22 C 1.334111e-01 2.008564e-01 6.454384e-02
C23 C 1.105521e-01 3.151256e-02 1.526220e-01
C24 C 7.249414e-02 4.209284e-02 1.647296e-01
C25 C 5.098456e-02 2.201343e-01 8.658052e-02
C26 C 7.290048e-02 3.857738e-01 9.943854e-01
H1 H 4.299574e-01 6.482174e-03 5.944657e-02
H2 H 4.671166e-01 2.837405e-01 9.239365e-01
H3 H 4.347721e-01 5.756905e-01 7.825217e-01
H4 H 3.702869e-01 5.950351e-01 7.832709e-01
H7 H 3.680420e-01 8.439614e-01 1.463762e-01
H8 H 3.038755e-01 8.626930e-01 1.690999e-01
H11 H 3.103585e-01 6.064646e-01 7.975815e-01
H12 H 2.460050e-01 6.241386e-01 8.169738e-01
H15 H 2.457550e-01 8.796847e-01 1.906904e-01
H16 H 1.817263e-01 8.946770e-01 2.075057e-01
H19 H 1.898422e-01 6.412114e-01 8.392076e-01
H20 H 1.253558e-01 6.605660e-01 8.399698e-01
H23 H 1.231117e-01 9.094808e-01 2.030603e-01
H24 H 5.894665e-02 9.282191e-01 2.257917e-01
H25 H 2.361221e-02 2.278391e-01 9.588996e-02
H26 H 5.842446e-02 5.052757e-01 9.412760e-01
C1 C 4.182964e-01 8.992632e-01 5.142154e-01
C2 C 4.409589e-01 7.433624e-01 4.297391e-01
C3 C 4.227081e-01 5.598367e-01 3.561001e-01
C4 C 3.848595e-01 5.361927e-01 3.649855e-01
C5 C 3.606067e-01 6.975172e-01 4.500772e-01
C6 C 3.793461e-01 8.797525e-01 5.255818e-01
```

```
C7 C 3.556898e-01 4.673512e-02 6.127669e-01
C8 C 3.172587e-01 3.741464e-02 6.178620e-01
C9 C 2.966153e-01 8.562778e-01 5.408538e-01
C10 C 3.198496e-01 6.856816e-01 4.583245e-01
C11 C 2.996999e-01 5.075689e-01 3.834808e-01
C12 C 2.610249e-01 4.979234e-01 3.888664e-01
C13 C 2.368633e-01 6.668156e-01 4.694011e-01
C14 C 2.563069e-01 8.474668e-01 5.457354e-01
C15 C 2.321131e-01 1.884380e-02 6.290052e-01
C16 C 1.938522e-01 8.790009e-03 6.346930e-01
C17 C 1.729842e-01 8.312160e-01 5.570780e-01
C18 C 1.955755e-01 6.597156e-01 4.732234e-01
C19 C 1.773242e-01 4.761802e-01 3.995915e-01
C20 C 1.394757e-01 4.525362e-01 4.084769e-01
C21 C 1.152263e-01 6.138656e-01 4.935641e-01
C22 C 1.339652e-01 7.960993e-01 5.690804e-01
C23 C 1.103064e-01 9.630861e-01 6.562490e-01
C24 C 7.187784e-02 9.537541e-01 6.613576e-01
C25 C 5.123183e-02 7.726325e-01 5.843386e-01
C26 C 7.446619e-02 6.020370e-01 5.018084e-01
H1 H 4.297588e-01 2.278121e-02 5.670406e-01
H2 H 4.674815e-01 7.593854e-01 4.208039e-01
H3 H 4.376207e-01 4.483623e-01 2.987351e-01
H4 H 3.741685e-01 4.088816e-01 3.147155e-01
H7 H 3.679869e-01 1.661724e-01 6.678433e-01
H8 H 3.029629e-01 1.527321e-01 6.748898e-01
H11 H 3.142599e-01 3.909799e-01 3.282616e-01
H12 H 2.493813e-01 3.740371e-01 3.374978e-01
H15 H 2.439774e-01 1.417218e-01 6.808335e-01
H16 H 1.797359e-01 1.231322e-01 6.928012e-01
H19 H 1.922400e-01 3.647032e-01 3.422289e-01
H20 H 1.287851e-01 3.252326e-01 3.581976e-01
H23 H 1.226061e-01 8.251182e-02 7.113389e-01
H24 H 5.758244e-02 6.907832e-02 7.183770e-01
H25 H 2.353738e-02 7.665789e-01 5.876972e-01
H26 H 6.062769e-02 4.796846e-01 4.504051e-01
C1 C 9.148918e-01 6.236976e-01 1.259655e-02
```

```
C2 C 9.370414e-01 7.852509e-01 9.313466e-01
C3 C 9.174753e-01 9.596183e-01 8.489075e-01
C4 C 8.790591e-01 9.719593e-01 8.495602e-01
C5 C 8.555507e-01 8.077759e-01 9.350302e-01
C6 C 8.753833e-01 6.316337e-01 1.557006e-02
C7 C 8.525252e-01 4.622714e-01 1.036372e-01
C8 C 8.144663e-01 4.728633e-01 1.157595e-01
C9 C 7.929578e-01 6.508980e-01 3.759436e-02
C10 C 8.148735e-01 8.165368e-01 9.453984e-01
C11 C 7.937971e-01 9.905179e-01 8.680933e-01
C12 C 7.554643e-01 9.921292e-04 8.800074e-01
C13 C 7.327390e-01 8.387581e-01 9.723868e-01
C14 C 7.531187e-01 6.621201e-01 5.114653e-02
C15 C 7.302464e-01 4.955726e-01 1.440681e-01
C16 C 6.922728e-01 5.057400e-01 1.553627e-01
C17 C 6.707485e-01 6.829705e-01 7.995321e-02
C18 C 6.921101e-01 8.507784e-01 9.880460e-01
C19 C 6.725426e-01 2.514181e-02 9.055976e-01
C20 C 6.341264e-01 3.748279e-02 9.062504e-01
C21 C 6.106220e-01 8.733014e-01 9.917237e-01
C22 C 6.304531e-01 6.971462e-01 7.225784e-02
C23 C 6.075941e-01 5.278024e-01 1.603360e-01
C24 C 5.695361e-01 5.383827e-01 1.724436e-01
C25 C 5.480265e-01 7.164241e-01 9.429452e-02
C26 C 5.699424e-01 8.820637e-01 2.099407e-03
H1 H 9.269994e-01 5.027720e-01 6.716056e-02
H2 H 9.641585e-01 7.800304e-01 9.316505e-01
H3 H 9.318140e-01 7.198040e-02 7.902357e-01
H4 H 8.673288e-01 9.132491e-02 7.909849e-01
H7 H 8.650839e-01 3.402512e-01 1.540902e-01
H8 H 8.009175e-01 3.589828e-01 1.768139e-01
H11 H 8.074005e-01 1.027545e-01 8.052955e-01
H12 H 7.430469e-01 1.204285e-01 8.246878e-01
H15 H 7.427970e-01 3.759746e-01 1.984044e-01
H16 H 6.787682e-01 3.909669e-01 2.152197e-01
H19 H 6.868841e-01 1.375013e-01 8.469216e-01
H20 H 6.223977e-01 1.568559e-01 8.476838e-01
```

```
H23 H 6.201537e-01 4.057706e-01 2.107743e-01
H24 H 5.559886e-01 4.245089e-01 2.335057e-01
H25 H 5.206542e-01 7.241289e-01 1.036040e-01
H26 H 5.554664e-01 1.565591e-03 9.489900e-01
C1 C 9.183925e-01 3.976768e-01 5.000463e-01
C2 C 9.410550e-01 2.417760e-01 4.155701e-01
C3 C 9.228041e-01 5.825035e-02 3.419310e-01
C4 C 8.849556e-01 3.460632e-02 3.508165e-01
C5 C 8.607028e-01 1.959308e-01 4.359081e-01
C6 C 8.794421e-01 3.781661e-01 5.114127e-01
C7 C 8.557858e-01 5.451487e-01 5.985979e-01
C8 C 8.173547e-01 5.358283e-01 6.036929e-01
C9 C 7.967113e-01 3.546914e-01 5.266847e-01
C10 C 8.199456e-01 1.840952e-01 4.441554e-01
C11 C 7.997960e-01 5.982477e-03 3.693118e-01
C12 C 7.611210e-01 9.963370e-01 3.746973e-01
C13 C 7.369594e-01 1.652293e-01 4.552321e-01
C14 C 7.564029e-01 3.458805e-01 5.315664e-01
C15 C 7.322092e-01 5.172574e-01 6.148361e-01
C16 C 6.939482e-01 5.072036e-01 6.205239e-01
C17 C 6.730802e-01 3.296296e-01 5.429089e-01
C18 C 6.956715e-01 1.581292e-01 4.590543e-01
C19 C 6.774203e-01 9.745938e-01 3.854224e-01
C20 C 6.395717e-01 9.509498e-01 3.943079e-01
C21 C 6.153224e-01 1.122792e-01 4.793951e-01
C22 C 6.340613e-01 2.945129e-01 5.549114e-01
C23 C 6.104024e-01 4.614997e-01 6.420800e-01
C24 C 5.719739e-01 4.521677e-01 6.471885e-01
C25 C 5.513279e-01 2.710461e-01 5.701696e-01
C26 C 5.745622e-01 1.004506e-01 4.876393e-01
H1 H 9.298549e-01 5.211948e-01 5.528715e-01
H2 H 9.675776e-01 2.577990e-01 4.066348e-01
H3 H 9.377167e-01 9.467759e-01 2.845661e-01
H4 H 8.742646e-01 9.072952e-01 3.005465e-01
H7 H 8.680830e-01 6.645860e-01 6.536742e-01
H8 H 8.030589e-01 6.511457e-01 6.607208e-01
H11 H 8.143560e-01 8.893936e-01 3.140926e-01
```

```
H12 H 7.494774e-01 8.724508e-01 3.233287e-01
H15 H 7.440734e-01 6.401354e-01 6.666644e-01
H16 H 6.798319e-01 6.215458e-01 6.786321e-01
H19 H 6.923360e-01 8.631168e-01 3.280599e-01
H20 H 6.288812e-01 8.236462e-01 3.440286e-01
H23 H 6.227021e-01 5.809254e-01 6.971699e-01
H24 H 5.576785e-01 5.674919e-01 7.042080e-01
H25 H 5.236334e-01 2.649926e-01 5.735282e-01
H26 H 5.607237e-01 9.780982e-01 4.362360e-01
```

9.3. VASE

Figure 9.2 shows the raw data gained from variable angle spectroscopic ellipsometry (VASE) with the corresponding fit of a 20 nm of [6]Phenacene thin film grown at a deposition rate of 2 Å/min. The film was deposited on native silicon and glass substrates. One glass substrate had a transparent and the other one had a rough backside.

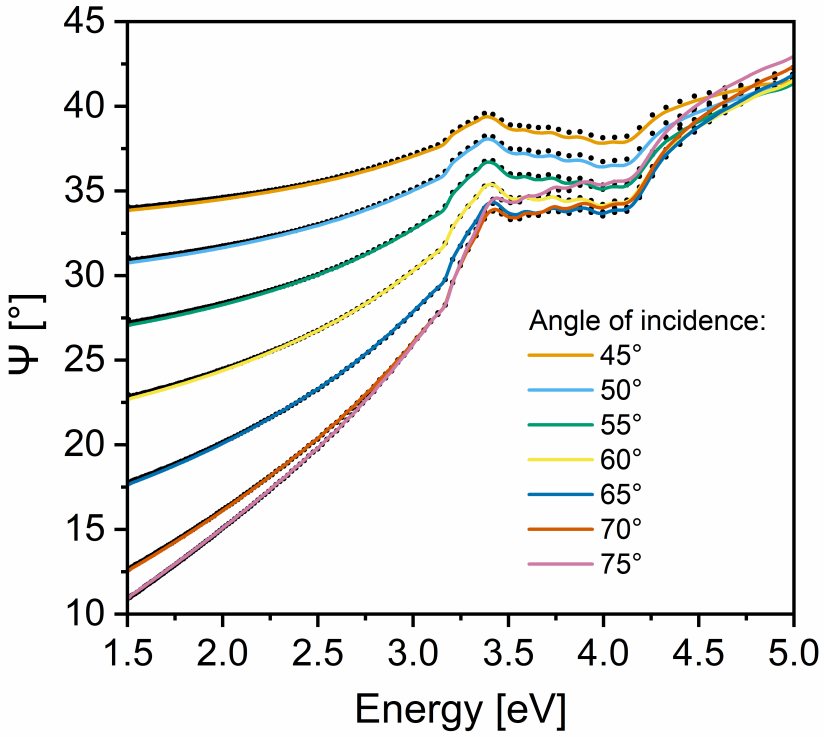

Figure 9.2.: VASE spectra at different angles of incidence with fitted data. Image is taken from Ref. [89].

10. Additional data and comments on alkali metal doped [6]Phenacene thin films

This section covers additional data from the results of Chapter 6.

10.1. Molecular orientation

Similar to Appendix 9.2 the contents of the CIF file for potassium doped [6]Phenacene used in Figure 6.10 are parsed below.

```
data_
loop_
_symmetry_equiv_pos_site_id
_symmetry_equiv_pos_as_xyz
1 x,y,z
_cell_length_a 32
_cell_length_b 6.2
_cell_length_c 8.6
_cell_angle_alpha 90
_cell_angle_beta 96
_cell_angle_gamma 90

loop_
_atom_site_label
_atom_site_type_symbol
_atom_site_fract_x
_atom_site_fract_y
_atom_site_fract_z
C C 0.429022648 0.205279032 0.976365194
C C 0.449052567 0.389912742 0.911729835
```

```
C C 0.427343265 0.566915484 0.846461474
C C 0.388883947 0.560133387 0.847600388
C C 0.367512814 0.371520806 0.916057029
C C 0.389530071 0.193204839 0.979361491
C C 0.368871553 -0.000655484 1.049900236
C C 0.330712776 -0.010903226 1.06191337
C C 0.306978616 0.168069677 1.001020724
C C 0.326789286 0.358459839 0.926204595
C C 0.303544843 0.533482419 0.865814703
C C 0.265116744 0.523017742 0.877615044
C C 0.24444339 0.335575161 0.952872896
C C 0.267026485 0.157332903 1.01443514
C C 0.246272762 -0.034550161 1.089862291
C C 0.20821188 -0.045039032 1.101047402
C C 0.184455018 0.132670323 1.042735054
C C 0.203676559 0.324890968 0.968364855
C C 0.181966029 0.501890484 0.903087258
C C 0.143506714 0.495108548 0.904226288
C C 0.122139423 0.306499194 0.972686203
C C 0.144155465 0.128170645 1.035984118
C C 0.123495629 -0.06567371 1.106534905
C C 0.085338057 -0.07593 1.118533074
C C 0.061602659 0.10304629 1.057656446
C C 0.081413446 0.293437258 0.982841135
H H 0.442641721 0.08224 1.019106778
H H 0.476137985 0.398034839 0.911942746
H H 0.440228002 0.695164516 0.799418068
H H 0.375695183 0.682478226 0.800886227
H H 0.382987575 -0.123874677 1.088611954
H H 0.31862184 -0.140665323 1.11113113
H H 0.315729474 0.661930968 0.814790653
H H 0.251218859 0.644553065 0.834023571
H H 0.26031315 -0.156016613 1.132498298
H H 0.196188263 -0.175465645 1.149043937
H H 0.194853551 0.630139032 0.856039525
H H 0.130319294 0.61746 0.857521013
H H 0.137612856 -0.188901452 1.145231657
```

```
H H 0.073248316 -0.205686129 1.167758901
H H 0.034152727 0.095664194 1.06687076
H H 0.065448396 0.413656613 0.941350706
C C 0.439581512 0.856207581 0.486309104
C C 0.461088147 0.701094677 0.396600929
C C 0.441606038 0.524970806 0.320857159
C C 0.403705277 0.507513387 0.332737356
C C 0.380656538 0.668300968 0.423401816
C C 0.400611154 0.842937581 0.500855651
C C 0.378197068 1.009159194 0.593680318
C C 0.339837256 1.006361935 0.602447297
C C 0.317998123 0.833250806 0.523780305
C C 0.339953826 0.663215484 0.435387241
C C 0.318625968 0.492916613 0.35886923
C C 0.280020142 0.489820484 0.367932718
C C 0.257131392 0.658431774 0.45443414
C C 0.27777307 0.831309516 0.532560964
C C 0.254866505 1.002253387 0.621802163
C C 0.216669189 0.998657258 0.631099607
C C 0.194635755 0.829187258 0.551992529
C C 0.215946612 0.65843871 0.462353453
C C 0.196464066 0.482304839 0.386616348
C C 0.158563304 0.464847258 0.398496546
C C 0.135518062 0.625639355 0.489156446
C C 0.155472157 0.800273871 0.566621739
C C 0.133055599 0.966501129 0.659430738
C C 0.09469823 0.963690968 0.668210111
C C 0.072856608 0.79059629 0.589533531
C C 0.094812382 0.620561613 0.501139649
H H 0.451869232 0.974699032 0.54053827
H H 0.487648451 0.712940323 0.385632236
H H 0.455691252 0.414111613 0.2597965
H H 0.392150608 0.384939516 0.280769298
H H 0.391279275 1.123286774 0.649859117
H H 0.326397519 1.120977258 0.663247928
H H 0.332315112 0.376876129 0.299748383
H H 0.267546045 0.370907419 0.315121787
```

```
H H 0.267551402 1.12009129 0.674999747
H H 0.203398273 1.112201452 0.692893936
H H 0.210552332 0.371442419 0.32555756
H H 0.147009139 0.34228129 0.346519718
H H 0.146140249 1.080615806 0.715621931
H H 0.081258988 1.078313548 0.729002791
H H 0.045219456 0.789262258 0.59557079
H H 0.080164498 0.503575806 0.448585473
C C 0.915225034 0.710279032 0.015328792
C C 0.935254918 0.894912581 -0.049306684
C C 0.913545651 1.071915323 -0.114574928
C C 0.875086332 1.065133387 -0.113436014
C C 0.853715199 0.876520645 -0.044979374
C C 0.875732456 0.698204839 0.018325089
C C 0.855073935 0.504344355 0.088863717
C C 0.816915162 0.494096613 0.100876968
C C 0.793181002 0.673069516 0.039984322
C C 0.812991637 0.863459839 -0.034831924
C C 0.789747228 1.038482258 -0.095221699
C C 0.751319127 1.028017742 -0.083421475
C C 0.730645775 0.840575161 -0.008163506
C C 0.753228871 0.662332742 0.053398738
C C 0.732475144 0.470449839 0.128825772
C C 0.694414235 0.459960806 0.140011
C C 0.670657373 0.637670161 0.081698652
C C 0.689878941 0.829890806 0.007328336
C C 0.668168415 1.006890484 -0.057949144
C C 0.629709097 1.000108387 -0.056810231
C C 0.608341809 0.811499032 0.0116498
C C 0.63035785 0.633170484 0.074947716
C C 0.609698015 0.439326129 0.145498503
C C 0.571540443 0.429069839 0.157496672
C C 0.547805042 0.60804629 0.096619927
C C 0.567615797 0.798437097 0.021804616
H H 0.928844072 0.587239839 0.058070259
H H 0.962340368 0.903034839 -0.049093773
H H 0.926430387 1.200164516 -0.161618334
```

```
H H 0.861897568 1.187478065 -0.160150175
H H 0.869189957 0.381125161 0.127575435
H H 0.804824226 0.364334516 0.150094728
H H 0.801931825 1.166930806 -0.146245866
H H 0.73742121 1.149553065 -0.127012948
H H 0.746515535 0.348983226 0.171461896
H H 0.682390648 0.329534194 0.188007534
H H 0.681055936 1.135138871 -0.104996877
H H 0.616521645 1.122459839 -0.103515506
H H 0.623815238 0.316098387 0.184195138
H H 0.559450702 0.29931371 0.206722499
H H 0.520355112 0.600664032 0.105834358
H H 0.551650747 0.918656452 -0.019685813
C C 0.906093611 0.374467581 0.495587957
C C 0.927600246 0.219354677 0.405879782
C C 0.908118169 0.043230806 0.330136013
C C 0.870217408 0.025773387 0.34201621
C C 0.847168668 0.186560968 0.43268067
C C 0.867123253 0.361197581 0.510134505
C C 0.844709167 0.527419194 0.602959171
C C 0.806349384 0.524621935 0.611726034
C C 0.784510222 0.351510806 0.533059159
C C 0.806465957 0.181475484 0.444666095
C C 0.785138099 0.011176613 0.368148084
C C 0.746532241 0.008080484 0.377211572
C C 0.723643492 0.176691774 0.463712994
C C 0.744285201 0.349569516 0.541839818
C C 0.721378604 0.520513387 0.631081016
C C 0.68318132 0.516917258 0.64037846
C C 0.661147885 0.347447258 0.561271383
C C 0.682458742 0.17669871 0.471632307
C C 0.662976165 0.000564839 0.395895202
C C 0.625075404 -0.016892742 0.407775399
C C 0.602030161 0.143899355 0.4984353
C C 0.621984253 0.318533871 0.575900476
C C 0.599567698 0.484761129 0.668709592
C C 0.56121036 0.481950968 0.677488965
```

```
C C 0.539368738 0.30885629 0.598812385
C C 0.561324513 0.138821613 0.510418503
H H 0.918381362 0.492959032 0.549817123
H H 0.954160582 0.231200323 0.39491109
H H 0.922203382 -0.067628387 0.269075353
H H 0.858662707 -0.096800484 0.290048152
H H 0.857791375 0.641546774 0.659137971
H H 0.79290965 0.639237258 0.672526782
H H 0.798827243 -0.104863871 0.309027237
H H 0.734058175 -0.110832581 0.32440064
H H 0.734063501 0.63835129 0.684278601
H H 0.669910404 0.630461452 0.70217279
H H 0.677064462 -0.110297581 0.334836413
H H 0.613521238 -0.13945871 0.355798572
H H 0.612652379 0.598875806 0.724900785
H H 0.547771087 0.596573548 0.738281645
H H 0.511731556 0.307522258 0.604849644
H H 0.546676628 0.021835806 0.457864327
K K 0.125 1 0.33
K K 0.225 0.33 0.66
K K 0.275 1 0.33
K K 0.375 0.33 0.66
K K 0.725 0.33 0.75
K K 0.625 0.5 0.33
K K 0.875 0.33 0.75
K K 0.775 0.5 0.33
```

10.2. SEM

Figures 10.1 and 10.2 show the raw SEM images for pure and alkali metal doped [6]Phenacene from Section 6.2 without image post-processing.

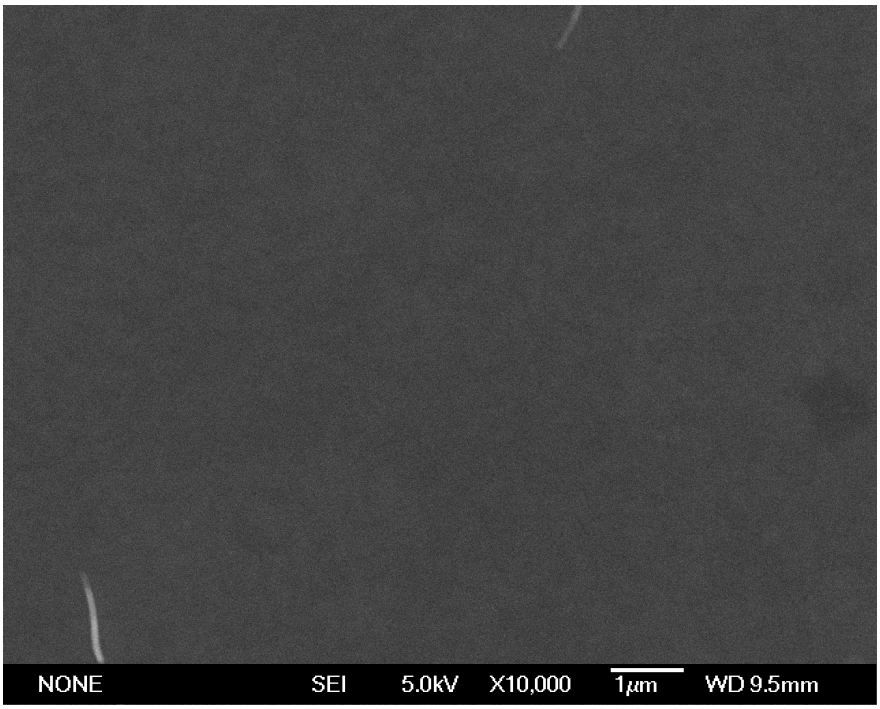

Figure 10.1.: SEM image of a 2 Å/min 20 nm [6]Phenacene thin film.

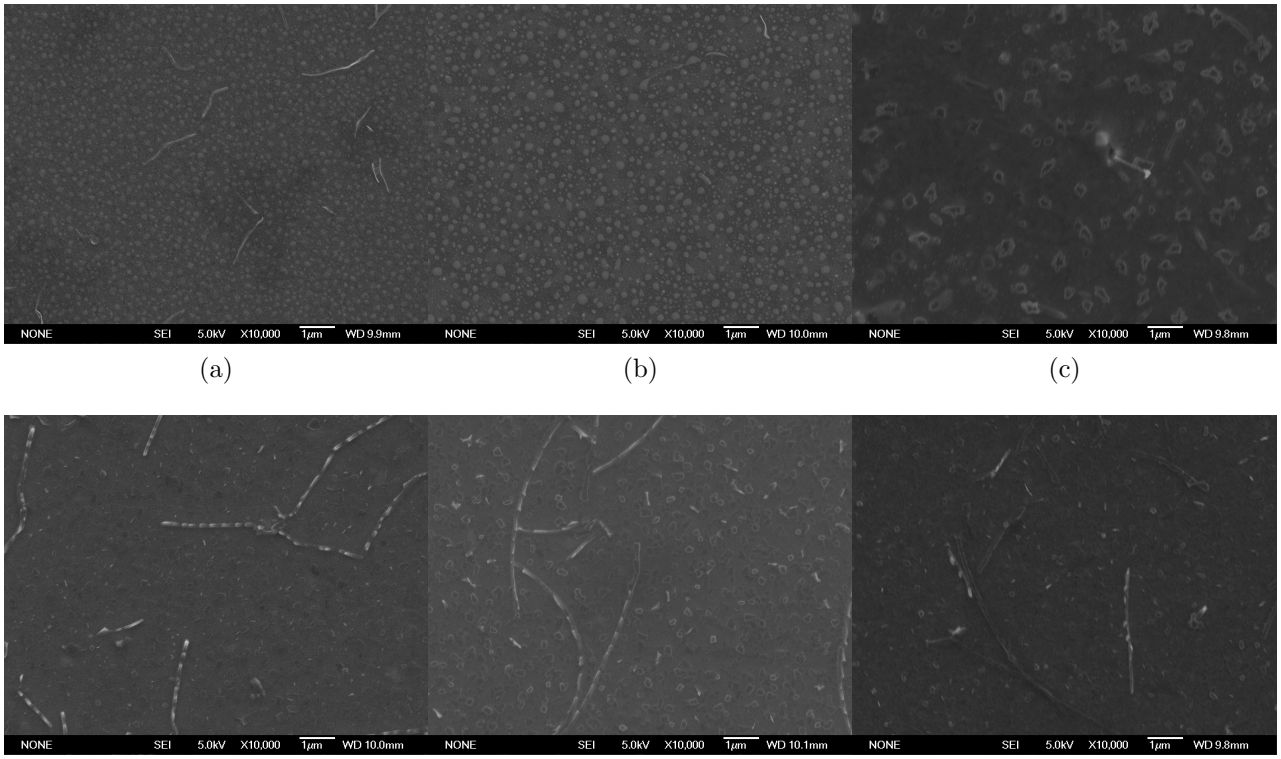

(a) (b) (c)

(d) (e) (f)

Figure 10.2.: SEM images of 2 Å/min 20 nm [6]Phenacene films mixed with various alkali metals: a) K on top, b) Rb on top, c) Cs on top, d) K co-deposition, e) Rb co-deposition and f) Cs co-deposition.

Bibliography

[1] A. Loi, L. Basirico, P. Cosseddu, S. Lai, M. Barbaro, A. Bonfiglio, P. Maiolino, E. Baglini, S. Denei, F. Mastrogiovanni, *et al.*, "Organic bendable and stretchable field effect devices for sensing applications," *IEEE Sensors Journal*, vol. 13, no. 12, pp. 4764–4772, 2013.

[2] S. H. Lee, H. Park, S. Kim, W. Son, I. W. Cheong, and J. H. Kim, "Transparent and flexible organic semiconductor nanofilms with enhanced thermoelectric efficiency," *Journal of Materials Chemistry A: Materials for Energy and Sustainability*, vol. 2, no. 20, pp. 7288–7294, 2014.

[3] S. E. Root, S. Savagatrup, A. D. Printz, D. Rodriquez, and D. J. Lipomi, "Mechanical properties of organic semiconductors for stretchable, highly flexible, and mechanically robust electronics," *Chemical Reviews*, vol. 117, no. 9, pp. 6467–6499, 2017.

[4] Y. Yuan, G. Giri, A. L. Ayzner, A. P. Zoombelt, S. C. B. Mannsfeld, J. Chen, D. Nordlund, M. F. Toney, J. Huang, and Z. Bao, "Ultra-high mobility transparent organic thin film transistors grown by an off-centre spin-coating method," *Nature Communications*, vol. 5, no. 1, 2014.

[5] S. R. Forrest, "The path to ubiquitous and low-cost organic electronic appliances on plastic," *Nature*, vol. 428, pp. 911–918, 2004.

[6] R. Gaudiana and C. Brabec, "Fantastic plastic," *Nature Photonics*, vol. 2, no. 5, pp. 287–289, 2008.

[7] B. Ecker, "Flexibel, leicht und durchsichtig," *Physik in unserer Zeit*, vol. 44, no. 2, pp. 84–91, 2013.

[8] H. Pan, Y. Li, Y. Wu, P. Liu, B. S. Ong, S. Zhu, and G. Xu, "Low-temperature, solution-processed, high-mobility polymer semiconductors for thin-film transistors," *Journal of the American Chemical Society*, vol. 129, no. 14, pp. 4112–4113, 2007.

[9] C. W. Tang, "Two-layer organic photovoltaic cell," *Applied Physics Letters*, vol. 48, no. 2, pp. 183–185, 1986.

[10] B. Kippelen and J.-L. Brédas, "Organic photovoltaics," *Energy & Environmental Science*, vol. 2, no. 3, pp. 251–261, 2009.

[11] S. B. Darling and F. You, "The case for organic photovoltaics," *RSC Advances*, vol. 3, no. 39, pp. 17633–17648, 2013.

[12] K. Leo, "Organic photovoltaics," *Nature Reviews Materials*, vol. 1, no. 8, p. 16056, 2016.

[13] O. Inganäs, "Organic photovoltaics over three decades," *Advanced Materials*, vol. 30, no. 35, p. 1800388, 2018.

[14] C. W. Tang and S. A. VanSlyke, "Organic electroluminescent diodes," *Applied Physics Letters*, vol. 51, no. 12, pp. 913–915, 1987.

[15] S. Reineke, F. Lindner, G. Schwartz, N. Seidler, K. Walzer, B. Lüssem, and K. Leo, "White organic light-emitting diodes with fluorescent tube efficiency," *Nature*, vol. 459, no. 7244, pp. 234–238, 2009.

[16] R. Meerheim, K. Walzer, G. He, M. Pfeiffer, and K. Leo, "Highly efficient organic light emitting diodes (OLED) for diplays and lighting," in *Organic Optoelectronics and Photonics II*, vol. 6192, pp. 100–115, SPIE, 2006.

[17] J. Yoon, H. Kwon, M. Lee, Y. yeol Yu, N. Cheong, S. Min, J. Choi, H. Im, K. Lee, J. Jo, H. Kim, H. Choi, Y. Lee, *et al.*, "World 1stlarge size 18-inch flexible OLED display and the key technologies," *SID Symposium Digest of Technical Papers*, vol. 46, no. 1, pp. 962–965, 2015.

[18] J.-Y. Yan, J.-C. Ho, and J. Chen, "Foldable AMOLED display development: Progress and challenges," *Information Display*, vol. 31, no. 1, pp. 12–16, 2015.

[19] C. I. Park, M. Seong, M. A. Kim, D. Kim, H. Jung, M. Cho, S. H. Lee, H. Lee, S. Min, J. Kim, *et al.*, "Worlds first large size 77-inch transparent flexible OLED display," *Journal of the Society for Information Display*, vol. 26, no. 5, pp. 287–295, 2018.

[20] C. Dimitrakopoulos, I. Kymissis, S. Purushothaman, D. Neumayer, P. Duncombe, and R. Laibowitz, "Low-voltage, high-mobility pentacene transistors with solution-processed high dielectric constant insulators," *Advanced Materials*, vol. 11, pp. 1372–1375, 1999.

[21] G. Horowitz, "Organic field-effect transistors," *Advanced materials*, vol. 10, no. 5, pp. 365–377, 1998.

[22] C. D. Dimitrakopoulos and D. J. Mascaro, "Organic thin-film transistors: A review of recent advances," *IBM Journal of Research and Development*, vol. 45, no. 1, pp. 11–27, 2001.

[23] Y. Sun, Y. Liu, and D. Zhu, "Advances in organic field-effect transistors," *Journal of Materials Chemistry*, vol. 15, no. 1, p. 53, 2005.

[24] C. Zhang, P. Chen, and W. Hu, "Organic field-effect transistor-based gas sensors," *Chemical Society Reviews*, vol. 44, no. 8, pp. 2087–2107, 2015.

[25] M. R. Cavallari, L. M. Pastrana, C. D. F. Sosa, A. M. R. Marquina, J. E. E. Izquierdo, F. J. Fonseca, C. A. d. Amorim, L. G. Paterno, and I. Kymissis, "Organic thin-film transistors as gas sensors: a review," *Materials*, vol. 14, no. 1, p. 3, 2020.

[26] S. R. Forrest, "Ultrathin organic films grown by organic molecular beam deposition and related techniques," *Chemical Reviews*, vol. 97, no. 6, pp. 1793–1896, 1997.

[27] G. Witte and C. Wöll, "Growth of aromatic molecules on solid substrates for applications in organic electronics," *Journal of Materials Research*, vol. 19, no. 7, pp. 1889–1916, 2004.

[28] F. Schreiber, "Organic molecular beam deposition: Growth studies beyond the first monolayer," *phys. stat. sol. (a)*, vol. 201, no. 6, pp. 1037–1054, 2004.

[29] A. Hinderhofer and F. Schreiber, "Organic-organic heterostructures: Concepts and applications," *ChemPhysChem*, vol. 13, no. 3, pp. 628–643, 2012.

[30] S. Wang, Y. Kang, L. Wang, H. Zhang, Y. Wang, and Y. Wang, "Organic/inorganic hybrid sensors: A review," *Sensors and Actuators B: Chemical*, vol. 182, pp. 467–481, 2013.

[31] R. Mitsuhashi, Y. Suzuki, Y. Yamanari, H. Mitamura, T. Kambe, N. Ikeda, H. Okamoto, A. Fujiwara, M. Yamaji, N. Kawasaki, *et al.*, "Superconductivity in alkali-metal-doped picene," *Nature*, vol. 464, no. 7285, pp. 76–79, 2010.

[32] G. A. Artioli, F. Hammerath, M. C. Mozzati, P. Carretta, F. Corana, B. Mannucci, S. Margadonna, and L. Malavasi, "Superconductivity in sm-doped [n]phenacenes (n = 3, 4, 5)," *Chemical Communications*, vol. 51, no. 6, pp. 1092–1095, 2015.

[33] N. Koch, "Organic electronic devices and their functional interfaces," *ChemPhysChem*, vol. 8, no. 10, pp. 1438–1455, 2007.

[34] J. Blochwitz, T. Fritz, M. Pfeiffer, K. Leo, D. Alloway, P. Lee, and N. Armstrong, "Interface electronic structure of organic semiconductors with controlled doping levels," *Organic Electronics*, vol. 2, no. 2, pp. 97–104, 2001.

[35] B. Lüssem, M. Riede, and K. Leo, "Doping of organic semiconductors," *physica status solidi (a)*, vol. 210, no. 1, pp. 9–43, 2012.

[36] F. Deschler, E. D. Como, T. Limmer, R. Tautz, T. Godde, M. Bayer, E. von Hauff, S. Yilmaz, S. Allard, U. Scherf, *et al.*, "Reduced charge transfer exciton recombination in organic semiconductor heterojunctions by molecular doping," *Physical Review Letters*, vol. 107, no. 12, p. 127402, 2011.

[37] H. Kleemann, C. Schuenemann, A. A. Zakhidov, M. Riede, B. Lüssem, and K. Leo, "Structural phase transition in pentacene caused by molecular doping and its effect on charge carrier mobility," *Organic Electronics*, vol. 13, no. 1, pp. 58–65, 2012.

[38] H. Méndez, G. Heimel, A. Opitz, K. Sauer, P. Barkowski, M. Oehzelt, J. Soeda, T. Okamoto, J. Takeya, J.-B. Arlin, *et al.*, "Doping of organic semiconductors: Impact of dopant strength and electronic coupling," *Angewandte Chemie*, vol. 125, no. 30, pp. 7905–7909, 2013.

[39] R. S. Nohr, P. M. Kuznesof, K. J. Wynne, M. E. Kenney, and P. G. Siebenman, "Highly conducting linear stacked polymers: iodine-doped fluoroaluminum and fluorogallium phthalocyanines," *Journal of the American Chemical Society*, vol. 103, no. 15, pp. 4371–4377, 1981.

[40] M. F. Calhoun, J. Sanchez, D. Olaya, M. E. Gershenson, and V. Podzorov, "Electronic functionalization of the surface of organic semiconductors with self-assembled monolayers," *Nature Materials*, vol. 7, no. 1, pp. 84–89, 2007.

[41] G. Parthasarathy, C. Shen, A. Kahn, and S. R. Forrest, "Lithium doping of semiconducting organic charge transport materials," *Journal of Applied Physics*, vol. 89, no. 9, pp. 4986–4992, 2001.

[42] F. Roth and M. Knupfer, "Impact of potassium doping on the electronic structure of tetracene and pentacene: An electron energy-loss study," *The Journal of Chemical Physics*, vol. 143, no. 15, p. 154708, 2015.

[43] J. Lee, C. Park, I. Song, J. Y. Koo, T. Yoon, J. S. Kim, and H. C. Choi, "Highly reproducible alkali metal doping system for organic crystals through enhanced diffusion of alkali metal by secondary thermal activation," *Scientific Reports*, vol. 8, no. 1, 2018.

[44] K. Walzer, B. Maennig, M. Pfeiffer, and K. Leo, "Highly efficient organic devices based on electrically doped transport layers," *Chemical Reviews*, vol. 107, no. 4, pp. 1233–1271, 2007.

[45] I. Salzmann, G. Heimel, M. Oehzelt, S. Winkler, and N. Koch, "Molecular electrical doping of organic semiconductors: Fundamental mechanisms and emerging dopant design rules," *Accounts of Chemical Research*, vol. 49, no. 3, pp. 370–378, 2016.

[46] A. Franco-Cañellas, S. Duhm, A. Gerlach, and F. Schreiber, "Binding and electronic level alignment of pi-conjugated systems on metals," *Reports on Progress in Physics*, vol. 83, no. 6, p. 066501, 2020.

[47] H. Haick and D. Cahen, "Contacting organic molecules by soft methods: Towards molecule-based electronic devices," *Accounts of Chemical Research*, vol. 41, no. 3, pp. 359–366, 2008.

[48] A. C. Dürr, F. Schreiber, M. Kelsch, H. D. Carstanjen, and H. Dosch, "Morphology and thermal stability of metal contacts on crystalline organic thin films," *Advanced Materials*, vol. 14, no. 13-14, pp. 961–963, 2002.

[49] B. Krause, A. Dürr, K. Ritley, F. Schreiber, H. Dosch, and D. Smilgies, "On the coexistence of different polymorphs in organic epitaxy: α and β phase of PTCDA on Ag(111)," *Applied Surface Science*, vol. 175-176, pp. 332–336, 2001.

[50] B. Krause, A. C. Dürr, K. Ritley, F. Schreiber, H. Dosch, and D. Smilgies, "Structure and growth morphology of an archetypal system for organic epitaxy: PTCDA on Ag(111)," *Physical Review B*, vol. 66, no. 23, p. 235404, 2002.

[51] T. Schmitz-Hübsch, T. Fritz, F. Sellam, R. Staub, and K. Leo, "Epitaxial growth of 3,4,9,10-perylene-tetracarboxylic-dianhydride on Au(111): A STM and RHEED study," *Physical Review B*, vol. 55, pp. 7972–7976, 1997.

[52] K. Seki, N. Hayashi, H. Oji, E. Ito, Y. Ouchi, and H. Ishii, "Electronic structure of organic/metal interfaces," *Thin Solid Films*, vol. 393, no. 1-2, pp. 298–303, 2001.

[53] C. B. France, P. G. Schroeder, and B. A. Parkinson, "Direct observation of a widely spaced periodic row structure at the pentacene/Au(111) interface using scanning tunneling microscopy," *Nano Letters*, vol. 2, no. 7, pp. 693–696, 2002.

[54] A. C. Dürr, N. Koch, M. Kelsch, A. Rühm, J. Ghijsen, R. L. Johnson, J.-J. Pireaux, J. Schwartz, F. Schreiber, H. Dosch, *et al.*, "Interplay between morphology, structure, and electronic properties at diindenoperylene-gold interfaces," *Physical Review B*, vol. 68, p. 115428, 2003.

[55] A. Kahn, N. Koch, and W. Gao, "Electronic structure and electrical properties of interfaces between metals and π-conjugated molecular films," *Journal of Polymer Science Part B: Polymer Physics*, vol. 41, no. 21, pp. 2529–2548, 2003.

[56] J. Wagner, M. Gruber, A. Hinderhofer, A. Wilke, B. Bröker, J. Frisch, P. Amsalem, A. Vollmer, A. Opitz, N. Koch, *et al.*, "High fill factor and open circuit voltage in organic photovoltaic cells with diindenoperylene as donor material," *Advanced Functional Materials*, vol. 20, no. 24, pp. 4295–4303, 2010.

[57] A. Opitz, J. Wagner, W. Brütting, I. Salzmann, N. Koch, J. Manara, J. Pflaum, A. Hinderhofer, and F. Schreiber, "Charge separation at molecular donor–acceptor interfaces: Correlation between morphology and solar cell performance," *IEEE Journal of Selected Topics in Quantum Electronics*, vol. 16, no. 6, pp. 1707–1717, 2010.

[58] S. Kowarik, A. Gerlach, S. Sellner, F. Schreiber, L. Cavalcanti, and O. Konovalov, "Real-time observation of structural and orientational transitions during growth of organic thin films," *Physical Review Letters*, vol. 96, no. 12, p. 125504, 2006.

[59] S. Kowarik, A. Gerlach, and F. Schreiber, "Organic molecular beam deposition: fundamentals, growth dynamics, and in situ studies," *Journal of Physics: Condensed Matter*, vol. 20, no. 18, p. 184005, 2008.

[60] S. M. Sze and K. K. Ng, *Physics of Semiconductor Devices*. Wiley-Interscience, 2006.

[61] H. Klauk, *Organic Electronics*. Wiley-VCH, 2006.

[62] M. Schwoerer and H.-C. Wolf, *Organische Molekulare Festkorper*. Wiley-VCH, 2005.

[63] G. Jung and E. Breitmaier, *Organische Chemie Grundlagen, Verbindungsklassen, Reaktionen, Konzepte, Molekulstruktur, Naturstoffe, Syntheseplanung, Nachhaltigkeit*. Wiley & Sons, Limited, John, 2021.

[64] M. Tolan, *X-ray scattering from soft-matter thin films*. Springer, 1999.

[65] J. Als-Nielsen and D. McMorrow, *Elements of modern X-ray physics*. Wiley, 2011.

[66] A. Tkatchenko, L. Romaner, O. T. Hofmann, E. Zojer, C. Ambrosch-Draxl, and M. Scheffler, "Van der waals interactions between organic adsorbates and at organic/inorganic interfaces," *MRS Bulletin*, vol. 35, no. 6, pp. 435–442, 2010.

[67] Y. Zhao, H. T. Ng, E. Hanson, J. Dong, D. S. Corti, and E. I. Franses, "Computation of nonretarded london dispersion coefficients and Hamaker constants of copper phthalocyanine," *Journal of Chemical Theory and Computation*, vol. 6, no. 2, pp. 491–498, 2010.

[68] A. Pimpinelli and J. Villain, *Physics of Crystal Growth*. Cambridge University Press, 1998.

[69] J. A. Venables, G. D. T. Spiller, and M. Hanbucken, "Nucleation and growth of thin films," *Reports on Progress in Physics*, vol. 47, no. 4, pp. 399–459, 1984.

[70] E. Empting, M. Klopotek, A. Hinderhofer, F. Schreiber, and M. Oettel, "Lattice gas study of thin-film growth scenarios and transitions between them: Role of substrate," *Physical Review E*, vol. 103, no. 2, p. 023302, 2021.

[71] S. Kowarik, *Real-time studies of thin film growth of organic semiconductors*. PhD thesis, Wadham College, Oxford, 2006.

[72] A. I. Kitaigorodskii, *Mixed crystals*. New York Springer-Verlag, 1984.

[73] A. Farahzadi, M. Beigmohamadi, P. Niyamakom, S. Kremers, N. Meyer, M. Heuken, and M. Wuttig, "Characterization of amorphous organic thin films, determination of precise model for spectroscopic ellipsometry measurements," *Applied Surface Science*, vol. 256, no. 22, pp. 6612–6617, 2010.

[74] B. N. Dutta, "Lattice constants and thermal expansion of silicon up to 900 °C by x-ray method," *physica status solidi (b)*, vol. 2, no. 8, pp. 984–987, 1962.

[75] R. Rieger and K. Müllen, "Forever young: polycyclic aromatic hydrocarbons as model cases for structural and optical studies," *Journal of Physical Organic Chemistry*, vol. 23, no. 4, pp. 315–325, 2010.

[76] H. Okamoto, N. Kawasaki, Y. Kaji, Y. Kubozono, A. Fujiwara, and M. Yamaji, "Air-assisted high-performance field-effect transistor with thin films of picene," *Journal of the American Chemical Society*, vol. 130, no. 32, pp. 10470–10471, 2008.

[77] N. Kawasaki, Y. Kubozono, H. Okamoto, A. Fujiwara, and M. Yamaji, "Trap states and transport characteristics in picene thin film field-effect transistor," *Applied Physics Letters*, vol. 94, no. 4, p. 043310, 2009.

[78] X. He, R. Eguchi, H. Goto, E. Uesugi, S. Hamao, Y. Takabayashi, and Y. Kubozono, "Fabrication of single crystal field-effect transistors with phenacene-type molecules and their excellent transistor characteristics," *Organic Electronics*, vol. 14, no. 6, pp. 1673–1682, 2013.

[79] Y. Sugawara, Y. Kaji, K. Ogawa, R. Eguchi, S. Oikawa, H. Gohda, A. Fujiwara, and Y. Kubozono, "Characteristics of field-effect transistors using the one-dimensional

extended hydrocarbon [7]phenacene," *Applied Physics Letters*, vol. 98, no. 1, p. 013303, 2011.

[80] Y. Kubozono, X. He, S. Hamao, K. Teranishi, H. Goto, R. Eguchi, T. Kambe, S. Gohda, and Y. Nishihara, "Transistor application of phenacene molecules and their characteristics," *European Journal of Inorganic Chemistry*, vol. 2014, no. 24, pp. 3806–3819, 2014.

[81] H. Okamoto, R. Eguchi, S. Hamao, H. Goto, K. Gotoh, Y. Sakai, M. Izumi, Y. Takaguchi, S. Gohda, and Y. Kubozono, "An extended phenacene-type molecule, [8]phenacene: Synthesis and transistor application," *Scientific Reports*, vol. 4, no. 1, p. 5330, 2014.

[82] N. Komura, H. Goto, X. He, H. Mitamura, R. Eguchi, Y. Kaji, H. Okamoto, Y. Sugawara, S. Gohda, K. Sato, *et al.*, "Characteristics of [6]phenacene thin film field-effect transistor," *Applied Physics Letters*, vol. 101, no. 8, p. 083301, 2012.

[83] R. Eguchi, X. He, S. Hamao, H. Goto, H. Okamoto, S. Gohda, K. Sato, and Y. Kubozono, "Fabrication of high performance/highly functional field-effect transistor devices based on [6]phenacene thin films," *Physical Chemistry Chemical Physics*, vol. 15, pp. 20611–20617, 2013.

[84] H. Okamoto, S. Hamao, R. Eguchi, H. Goto, Y. Takabayashi, P. Y.-H. Yen, L. U. Liang, C.-W. Chou, G. Hoffmann, S. Gohda, *et al.*, "Synthesis of the extended phenacene molecules, [10]phenacene and [11]phenacene, and their performance in a field-effect transistor," *Scientific Reports*, vol. 9, no. 1, 2019.

[85] T. Kosugi, T. Miyake, S. Ishibashi, R. Arita, and H. Aoki, "First-principles electronic structure of solid picene," *Journal of the Physical Society of Japan*, vol. 78, no. 11, p. 113704, 2009.

[86] M.-H. Li, S.-Y. Zhang, H.-Y. Lv, W.-J. Li, Z. Lu, C. Yang, and G.-H. Zhong, "[n]phenacenes: Promising organic anodes for potassium-ion batteries," *The Journal of Physical Chemistry C*, vol. 124, no. 13, pp. 6964–6970, 2020.

[87] T. Krygowski, A. Ciesielski, B. Swirska, and P. Leszczynski, "Variation of molecular geometry and aromatic character of chrysene and perylene in their eda complexes. refinement of x-ray crystal and molecular structure of chrysene and perylene," *Polish Journal of Chemistry*, vol. 68, no. 10, pp. 2097–2107, 1994.

[88] A. De, R. Ghosh, S. Roychowdhury, and P. Roychowdhury, "Structural analysis of picene, $C_{22}H_{14}$," *Acta Crystallographica Section C Crystal Structure Communications*, vol. 41, no. 6, pp. 907–909, 1985.

[89] M. Zwadlo, J. Hagara, G. Duva, J. Hagenlocher, A. Gerlach, I. Zaluzhnyy, M. Hodas, A. Hinderhofer, P. Siffalovic, and F. Schreiber, "Structure of thin films of [6] and [7]phenacene and impact of potassium deposition," *Advanced Optical Materials*, vol. 9, no. 14, p. 2002193, 2021.

[90] T. Hosokai, A. Hinderhofer, F. Bussolotti, K. Yonezawa, C. Lorch, A. Vorobiev, Y. Hasegawa, Y. Yamada, Y. Kubozoro, A. Gerlach, *et al.*, "Thickness and substrate dependent thin film growth of picene and impact on the electronic structure," *The Journal of Physical Chemistry C*, vol. 119, no. 52, pp. 29027–29037, 2015.

[91] J. Hagenlocher, K. Broch, M. Zwadlo, D. Lepple, J. Rawle, F. Carla, S. Kera, F. Schreiber, and A. Hinderhofer, "Thickness-dependent energy-level alignment at the organic–organic interface induced by templated gap states," *Advanced Materials Interfaces*, vol. 9, no. 3, p. 2101382, 2021.

[92] M. Das, "Computational investigation on tunable optical band gap in armchair polyacenes," *The Journal of Chemical Physics*, vol. 143, no. 6, p. 064704, 2015.

[93] L. Váňa, M. Jakubec, J. Sýkora, I. Císařová, J. Storch, and V. Církva, "Synthesis of aza[n]phenacenes (n = 4–6) via photocyclodehydrochlorination of 2-chloro-n-aryl-1-naphthamides," *The Journal of Organic Chemistry*, vol. 86, no. 19, pp. 13252–13264, 2021.

[94] F. B. Mallory, K. E. Butler, A. C. Evans, E. J. Brondyke, C. W. Mallory, C. Yang, and A. Ellenstein, "Phenacenes: A family of graphite ribbons. 2. syntheses of some [7]phenacenes and an [11]phenacene by stilbene-like photocyclizations," *Journal of the American Chemical Society*, vol. 119, no. 9, pp. 2119–2124, 1997.

[95] Lin-gun Liu, "Compression and polymorphism of potassium to 400 kbar," *Journal of Physics and Chemistry of Solids*, vol. 47, no. 11, pp. 1067–1072, 1986.

[96] C. S. Barrett, "X-ray study of the alkali metals at low temperatures," *Acta Crystallographica*, vol. 9, no. 8, pp. 671–677, 1956.

[97] C. E. Weir, G. J. Piermarini, and S. Block, "On the crystal structures of Cs II and Ga II," *The Journal of Chemical Physics*, vol. 54, no. 6, pp. 2768–2770, 1971.

[98] "Saes getters alkali metal dispenser brochure." https://www.saesgetters.com/sites/default/files/AMD 20Brochure_0.pdf Accessed Online: 02.03.2022.

[99] P. della Porta, C. Emili, and S. J. Hellier, "Alkali metal generation and gas evolution from alkali metal dispensers." https://www.saesgetters.com/sites/default/files/AMD Generation and Gas Evolution_0.pdf Accessed Online: 25.02.2022.

[100] B. Kindl, "Gettering processes," *Vacuum*, vol. 16, no. 4, pp. 165–173, 1966.

[101] C. F. Macrae, I. Sovago, S. J. Cottrell, P. T. A. Galek, P. McCabe, E. Pidcock, M. Platings, G. P. Shields, J. S. Stevens, M. Towler, *et al.*, "Mercury 4.0: from visualization to analysis, design and prediction," *Journal of Applied Crystallography*, vol. 53, no. 1, pp. 226–235, 2020.

[102] E. R. Jette and F. Foote, "Precision determination of lattice constants," *The Journal of Chemical Physics*, vol. 3, no. 10, pp. 605–616, 1935.

[103] D. W. Umrath, *Fundamentals of Vacuum Technology*. Leybold Vacuum, 1998. Products and Reference Book 2003/2004.

[104] K. Jousten, *Handbuch Vakuumtechnik*. Wiesbaden: Springer Fachmedien Wiesbaden, 2018.

[105] O'Hanlon, *A User's Guide to Vacuum Technology*. John Wiley & Sons, 2003.

[106] H. Lüth, *Solid Surfaces, Interfaces and Thin Films*. Springer International Publishing, 2014.

[107] K. D. Carlson, P. W. Gilles, and R. J. Thorn, "Molecular and hydrodynamical effusion of mercury vapor from Knudsen cells," *The Journal of Chemical Physics*, vol. 38, no. 11, pp. 2725–2735, 1963.

[108] E. Benes, "Improved quartz crystal microbalance technique," *Journal of Applied Physics*, vol. 56, no. 3, pp. 608–626, 1984.

[109] K. A. Ritley, B. Krause, F. Schreiber, and H. Dosch, "A portable ultrahigh vacuum organic molecular beam deposition system for in situ x-ray diffraction measurements," *Review of Scientific Instruments*, vol. 72, no. 2, p. 1453, 2001.

[110] R. Bujila, A. Omar, and G. Poludniowski, "A validation of SpekPy: A software toolkit for modelling x-ray tube spectra," *Physica Medica*, vol. 75, pp. 44–54, 2020.

[111] M. R. Stevens, Q. Chen, U. Weierstall, and J. C. Spence, "Transmission electron diffraction at 200 eV and damage thresholds below the carbon K edge," *Microscopy and Microanalysis*, vol. 6, no. 4, pp. 368–379, 2000.

[112] P. Li and R. Egerton, "Radiation damage in coronene, rubrene and p-terphenyl, measured for incident electrons of kinetic energy between 100 and 200keV," *Ultramicroscopy*, vol. 101, no. 2-4, pp. 161–172, 2004.

[113] M. Björck and G. Andersson, "GenX: an extensible x-ray reflectivity refinement program utilizing differential evolution," *Journal of Applied Crystallography*, vol. 40, no. 6, pp. 1174–1178, 2007.

[114] L. G. Parratt, "Surface studies of solids by total reflection of x-rays," *Physical Review*, vol. 95, pp. 359–369, 1954.

[115] A. Greco, V. Starostin, C. Karapanagiotis, A. Hinderhofer, A. Gerlach, L. Pithan, S. Liehr, F. Schreiber, and S. Kowarik, "Fast fitting of reflectivity data of growing thin films using neural networks," *Journal of Applied Crystallography*, vol. 52, no. 6, pp. 1342–1347, 2019.

[116] A. Greco, V. Starostin, A. Hinderhofer, A. Gerlach, M. W. A. Skoda, S. Kowarik, and F. Schreiber, "Neural network analysis of neutron and x-ray reflectivity data: pathological cases, performance and perspectives," *Machine Learning: Science and Technology*, vol. 2, no. 4, p. 045003, 2021.

[117] A. Greco, V. Starostin, E. Edel, V. Munteanu, N. Rußegger, I. Dax, C. Shen, F. Bertram, A. Hinderhofer, A. Gerlach, *et al.*, "Neural network analysis of neutron and x-ray reflectivity data: automated analysis using mlreflect, experimental errors and feature engineering," *Journal of Applied Crystallography*, vol. 55, no. 2, pp. 362–369, 2022.

[118] A. Hinderhofer, A. Greco, V. Starostin, V. Munteanu, L. Pithan, A. Gerlach, and F. Schreiber, "Machine learning for scattering data: strategies, perspectives and applications to surface scattering," *Journal of Applied Crystallography*, vol. 56, no. 1, pp. 3–11, 2023.

[119] A. Mahmood and J.-L. Wang, "A review of grazing incidence small- and wide-angle x-ray scattering techniques for exploring the film morphology of organic solar cells," *Solar RRL*, vol. 4, no. 10, p. 2000337, 2020.

[120] D. M. DeLongchamp, R. J. Kline, D. A. Fischer, L. J. Richter, and M. F. Toney, "Molecular characterization of organic electronic films," *Advanced Materials*, vol. 23, no. 3, pp. 319–337, 2010.

[121] Z. Jiang, "Gixsgui a MATLAB toolbox for grazing-incidence x-ray scattering data visualization and reduction, and indexing of buried three-dimensional periodic nanostructured films," *Journal of Applied Crystallography*, vol. 48, no. 3, pp. 917–926, 2015.

[122] D. P. Woodruff, *Modern Techniques of Surface Science*. Cambridge University Press, 2016.

[123] D. R. Penn, "Quantitative chemical analysis by ESCA," *Journal of Electron Spectroscopy and Related Phenomena*, vol. 9, no. 1, pp. 29–40, 1976.

[124] C. S. Fadley, "Angle-resolved x-ray photoelectron spectroscopy," *Progress in Surface Science*, vol. 16, no. 3, pp. 275–388, 1984.

[125] C. Papp and H.-P. Steinrück, "In situ high-resolution x-ray photoelectron spectroscopy – fundamental insights in surface reactions," *Surface Science Reports*, vol. 68, no. 3-4, pp. 446–487, 2013.

[126] J. Cazaux, "Secondary electron emission and fundamentals of charging mechanisms in XPS," *Journal of Electron Spectroscopy and Related Phenomena*, vol. 178-179, pp. 357–372, 2010.

[127] H. Sezen and S. Suzer, "XPS for chemical- and charge-sensitive analyses," *Thin Solid Films*, vol. 534, pp. 1–11, 2013.

[128] P. S. Bagus, E. S. Ilton, and C. J. Nelin, "The interpretation of XPS spectra: Insights into materials properties," *Surface Science Reports*, vol. 68, no. 2, pp. 273–304, 2013.

[129] C. Bürker, *Adsorption geometry of π-conjugated organic molecules on metal surfaces studied with the X-ray standing wave technique*. PhD thesis, Universitätsbibliothek Tübingen, 2014.

[130] "Scienta Omicron." www.scientaomicron.com.

[131] "Casa Software Ltd, Bay House, 5 Grosvenor Terrace, Teigmnmouth, Devon, TQ148NE, UK (2017)."

[132] *NanoWizard AFM Handbook Version 1.3*. JPK Instruments, 2005.

[133] T. Meier, H. Bässler, and A. Köhler, "The impact of grain boundaries on charge transport in polycrystalline organic field-effect transistors," *Advanced Optical Materials*, vol. 9, no. 14, p. 2100115, 2021.

[134] "Bruker." www.brukerafmprobes.com.

[135] D. Nečas and P. Klapetek, "Gwyddion: an open-source software for SPM data analysis," *Open Physics*, vol. 10, no. 1, 2012.

[136] J. Goldstein, D. E. Newbury, D. C. Joy, J. R. Michael, and N. W. M. Ritchie, *Scanning Electron Microscopy and X-Ray Microanalysis*. Springer-Verlag GmbH, Dec. 2017.

[137] A. Ul-Hamid, *A Beginners' Guide to Scanning Electron Microscopy*. Springer International Publishing, 2019.

[138] *Guide to Using WVASE*. J. A. Woollam Co., Inc., 2012.

[139] A. Hinderhofer, A. Gerlach, K. Broch, T. Hosokai, K. Yonezawa, K. Kato, S. Kera, N. Ueno, and F. Schreiber, "Geometric and electronic structure of templated C60 on diindenoperylene thin films," *The Journal of Physical Chemistry C*, vol. 117, no. 2, pp. 1053–1058, 2013.

[140] J. Krug, "Origins of scale invariance in growth processes," *Advances in Physics*, vol. 46, no. 2, pp. 139–282, 1997.

[141] A. Dürr, F. Schreiber, K. Ritley, V. Kruppa, J. Krug, H. Dosch, and B. Struth, "Rapid roughening in thin film growth of an organic semiconductor (diindenoperylene)," *Physical Review Letters*, vol. 90, no. 1, p. 016104, 2003.

[142] G. Schweicher, V. Lemaur, C. Niebel, C. Ruzié, Y. Diao, O. Goto, W.-Y. Lee, Y. Kim, J.-B. Arlin, J. Karpinska, *et al.*, "Bulky end-capped [1]benzothieno[3,2-b]benzothiophenes: Reaching high-mobility organic semiconductors by fine tuning of the crystalline solid-state order," *Advanced Materials*, vol. 27, no. 19, pp. 3066–3072, 2015.

[143] R. Hayakawa, X. Zhang, H. Dosch, N. Hiroshiba, T. Chikyow, and Y. Wakayama, "Stress release drives growth transition of quaterrylene thin films on SiO_2 surfaces," *Journal of Physical Chemistry C*, vol. 113, no. 6, pp. 2197–2199, 2009.

[144] S. Y. Son, Y. Kim, J. Lee, G.-Y. Lee, W.-T. Park, Y.-Y. Noh, C. E. Park, and T. Park, "High-field-effect mobility of low-crystallinity conjugated polymers with localized aggregates," *Journal of the American Chemical Society*, vol. 138, no. 26, pp. 8096–8103, 2016.

[145] H. Yang, T. Shin, L. Yang, K. Cho, C. Y. Ryu, and Z. Bao, "Effect of mesoscale crystalline structure on the field-effect mobility of regioregular poly(3-hexyl thiophene) in thin-film transistors," *Advanced Functional Materials*, vol. 15, no. 4, pp. 671–676, 2005.

[146] D. T. Scholes, P. Y. Yee, J. R. Lindemuth, H. Kang, J. Onorato, R. Ghosh, C. K. Luscombe, F. C. Spano, S. H. Tolbert, and B. J. Schwartz, "The effects of crystallinity on charge transport and the structure of sequentially processed F4TCNQ-doped conjugated polymer films," *Advanced Functional Materials*, vol. 27, no. 44, p. 1702654, 2017.

[147] G. Duva, A. Mann, L. Pithan, P. Beyer, J. Hagenlocher, A. Gerlach, A. Hinderhofer, and F. Schreiber, "Template-free orientation selection of rod-like molecular semiconductors in polycrystalline films," *Journal of Physical Chemistry Letters*, vol. 10, no. 5, pp. 1031–1036, 2019.

[148] H. Okamoto, M. Yamaji, S. Gohda, K. Sato, H. Sugino, and K. Satake, "Photochemical synthesis and electronic spectra of fulminene ([6]phenacene)," *Research on Chemical Intermediates*, vol. 39, no. 1, pp. 147–159, 2012.

[149] A. Hinderhofer, U. Heinemeyer, A. Gerlach, S. Kowarik, R. M. J. Jacobs, Y. Sakamoto, T. Suzuki, and F. Schreiber, "Optical properties of pentacene and perfluoropentacene thin films," *The Journal of Chemical Physics*, vol. 127, no. 19, p. 194705, 2007.

[150] A. A. Bakulin, R. Lovrincic, X. Yu, O. Selig, H. J. Bakker, Y. L. A. Rezus, P. K. Nayak, A. Fonari, V. Coropceanu, J.-L. Brédas, *et al.*, "Mode-selective vibrational modulation of charge transport in organic electronic devices," *Nature Communications*, vol. 6, no. 1, 2015.

[151] N. J. Hestand and F. C. Spano, "Expanded theory of H- and J-molecular aggregates: The effects of vibronic coupling and intermolecular charge transfer," *Chemical Reviews*, vol. 118, no. 15, pp. 7069–7163, 2018.

[152] T. Storzer, A. Hinderhofer, C. Zeiser, J. Novák, Z. Fišer, V. Belova, B. Reisz, S. Maiti, G. Duva, R. K. Hallani, *et al.*, "Growth, structure, and anisotropic optical properties of difluoro-anthradithiophene thin films," *The Journal of Physical Chemistry C*, vol. 121, no. 38, pp. 21011–21017, 2017.

[153] J. Krug, P. Politi, and T. Michely, "Island nucleation in the presence of step-edge barriers: Theory and applications," *Physical Review B*, vol. 61, no. 20, pp. 14037–14046, 2000.

[154] X. Yin, J. Shi, X. Niu, H. Huang, and X. Wang, "Wedding cake growth mechanism in one-dimensional and two-dimensional nanostructure evolution," *Nano Letters*, vol. 15, no. 11, pp. 7766–7772, 2015.

[155] H. Kang, W. Lee, J. Oh, T. Kim, C. Lee, and B. J. Kim, "From fullerene–polymer to all-polymer solar cells: The importance of molecular packing, orientation, and morphology control," *Accounts of Chemical Research*, vol. 49, no. 11, pp. 2424–2434, 2016.

[156] E. Pompei, C. Turchetti, S. Hamao, A. Miura, H. Goto, H. Okamoto, A. Fujiwara, R. Eguchi, and Y. Kubozono, "Fabrication of flexible high-performance organic field-effect transistors using phenacene molecules and their application toward flexible CMOS inverters," *Journal of Materials Chemistry C*, vol. 7, no. 20, pp. 6022–6033, 2019.

[157] D. Wynands, M. Erber, R. Rentenberger, M. Levichkova, K. Walzer, K.-J. Eichhorn, and M. Stamm, "Spectroscopic ellipsometry characterization of vacuum-deposited organic films for the application in organic solar cells," *Organic Electronics*, vol. 13, no. 5, pp. 885–893, 2012.

[158] M. Levichkova, D. Wynands, A. A. Levin, K. Walzer, D. Hildebrandt, M. Pfeiffer, V. Janonis, M. Pranaitis, V. Kažukauskas, K. Leo, *et al.*, "Dicyanovinyl sexithiophene as donor material in organic planar heterojunction solar cells: Morphological, optical, and electrical properties," *Organic Electronics*, vol. 12, no. 12, pp. 2243–2252, 2011.

[159] S. Kowarik, A. Gerlach, S. Sellner, F. Schreiber, J. Pflaum, L. Cavalcanti, and O. Konovalov, "Anomalous roughness evolution of rubrene thin films observed in real time during growth," *Physical Chemistry Chemical Physics*, vol. 8, no. 15, p. 1834, 2006.

[160] R. W. Solomon, "Free and open source software for the manipulation of digital images," *American Journal of Roentgenology*, vol. 192, no. 6, pp. W330–W334, 2009. PMID: 19457798.

[161] C. Lorch, K. Broch, V. Belova, G. Duva, A. Hinderhofer, A. Gerlach, M. Jankowski, and F. Schreiber, "Growth and annealing kinetics of α-sexithiophene and fullerene C60 mixed films," *Journal of Applied Crystallography*, vol. 49, no. 4, pp. 1266–1275, 2016.

[162] G. Duva, L. Pithan, C. Zeiser, B. Reisz, J. Dieterle, B. Hofferberth, P. Beyer, L. Bogula, A. Opitz, S. Kowarik, *et al.*, "Thin-film texture and optical properties of donor/acceptor complexes. diindenoperylene/F6TCNNQ vs alpha-sexithiophene/F6TCNNQ," *The Journal of Physical Chemistry C*, vol. 122, no. 32, pp. 18705–18714, 2018.

[163] G. Duva, P. Beyer, R. Scholz, V. Belova, A. Opitz, A. Hinderhofer, A. Gerlach, and F. Schreiber, "Ground-state charge-transfer interactions in donor:acceptor pairs of organic semiconductors – a spectroscopic study of two representative systems," *Physical Chemistry Chemical Physics*, vol. 21, no. 31, pp. 17190–17199, 2019.

[164] C. T. Campbell, "Ultrathin metal films and particles on oxide surfaces: structural, electronic and chemisorptive properties," *Surface Science Reports*, vol. 27, no. 1-3, pp. 1–111, 1997.

[165] K. H. Ernst, A. Ludviksson, R. Zhang, J. Yoshihara, and C. T. Campbell, "Growth model for metal films on oxide surfaces: Cu on ZnO(0001)-O," *Phys. Rev. B*, vol. 47, pp. 13782–13796, 1993.

[166] G. Kaune, M. A. Ruderer, E. Metwalli, W. Wang, S. Couet, K. Schlage, R. Röhlsberger, S. V. Roth, and P. Müller-Buschbaum, "In situ GISAXS study of gold film growth on conducting polymer films," *ACS Applied Materials Interfaces*, vol. 1, pp. 353–360, dec 2008.

[167] M. K. Corpinot and D.-K. Bučar, "A practical guide to the design of molecular crystals," *Crystal Growth and Design*, vol. 19, no. 2, pp. 1426–1453, 2018.

[168] S. R. Hall and B. McMahon, *International tables for crystallography, definition and exchange of crystallographic data*, vol. 8. Springer Science & Business Media, 2005.

List of abbreviations

Materials:

6Ph	[6]Phenacene
Au	Gold
C_6 H_6	Benzene
C_{26} H_{16}	[6]Phenacene
Chrysene	[4]Phenacene
Cs	Caesium
Fulminene	[6]Phenacene
Picene	[5]Phenacene
K	Potassium
N	Nitrogen
O	Oxygen
PEN	Pentacene
Rb	Rubidium
SiO_2	Silicon oxide

Methods:

AFM	Atomic force microscopy
BM	Bending magnet
BSE	Backscattered electrons
BW	Bandwidth
CAE	Constant analyser energy
CCD	Charge-coupled device
DESY	Deutsches Elektronen Synchrotron
ESRF	European synchrotron radiation facility
FOM	Function of merit
GA	Genetic algorithm

GISAXS	Grazing incidence small-angle X-ray scattering
GIWAXS	Grazing incidence wide-angle X-ray scattering
GIXD	Grazing incidence X-ray diffraction
HV	High vacuum
MV	Medium vacuum
OMBD	Organic molecular beam deposition
PES	Photoelectron spectroscopy
PETRA	Positron-Elektron-Tandem-Ring-Anlage
QCM	Quartz crystal microbalance
RV	Rough vacuum
SE	Secondary electrons
SEM	Scanning electron microscopy
UHV	Ultra-high vacuum
UPS	Ultraviolet photoelectron spectroscopy
UV/vis/NIR	Ultraviolet/visible/near-infrared
VASE	Variable angle spectroscopic ellipsometry
VL	Vacuum level
XRR	X-ray reflectivity
XPS	X-ray photoelectron spectroscopy

Other:

BHJ	Bulk heterojunction
CIF	Crystallographic information file
FET	Field-effect transistor
HOMO	Highest occupied molecular orbital
LED	Light-emitting diode
LUMO	Lowest unoccupied molecular orbital
OFET	Organic field-effect transistor
OLED	Organic light-emitting diode
OPV	Organic photovoltaics
OSC	Organic semiconductor
PAH	Polycyclic aromatic hydrocarbons
PHJ	Planar heterojunction
SK	Stranski-Krastanov (Layer plus island growth)
T_{Sub}	Substrate temperature
VW	Vollmer-Weber (Island growth)

List of publications

- Zwadlo, M., Hagara, J., Duva, G., Hagenlocher, J., Gerlach, A., Zaluzhnyy, I., Hodas, M., Hinderhofer, A., Siffalovic, P., Schreiber, F., Structure of Thin Films of [6] and [7]Phenacene and Impact of Potassium Deposition. Adv. Optical Mater. (2021), 9, 2002193

- Rußegger, N., Valencia, A. M., Merten L., Zwadlo, M., Duva, G., Pithan, L., Gerlach, A., Hinderhofer, A., Cocchi, C., and Schreiber, F., Molecular Charge Transfer Effects on Perylene Diimide Acceptor and Dinaphthothienothiophene Donor Systems, The Journal of Physical Chemistry C (2022) 126 (8), 4188-4198

- Hagenlocher, J., Broch, K., Zwadlo, M., Lepple, D., Rawle, J., Carla, F., Kera, S., Schreiber, F., Hinderhofer, A., Thickness-Dependent Energy-Level Alignment at the Organic–Organic Interface Induced by Templated Gap States. Adv. Mater. Interfaces (2022), 9, 2101382

- Reisz, B., Empting, E., Zwadlo, M., Hodas, M., Duva, G., Belova, V., Zeiser, C., Hagenlocher, J., Maiti, S., Hinderhofer, A., Gerlach, A., Oettel, M. and Schreiber, F., Thin film growth of phase-separating phthalocyanine-fullerene blends: A combined experimental and computational study, Phys. Rev. Materials (2021), 5, 045601

- Hagara, J., Mrkyvkova, N., Feriancová, L. Putala, M.,Nádaždy, P., Hodas, M. and Shaji, A., Nádaždy, V.,Huss-Hansen, M. K., Knaapila, M., Hagenlocher, J., Russegger, N., Zwadlo, M., Merten, L., Sojková, M., Hulman, M., Vlad, A., Pandit, P., Roth, S., Jergel, M., Majková, E., Hinderhofer, A., Siffalovic, P. and Schreiber, F., Novel highly substituted thiophene-based n-type organic semiconductor: structural study, optical anisotropy and molecular control, CrystEngComm (2020), 22(42), 7095-7103

Acknowledgements

At the very end of this thesis, I would like to express my sincere gratitude to everyone who supported me during the years of my Ph.D. thesis. First of all, I would like to thank my supervisor Prof. Dr. Dr. h.c. Frank Schreiber for the opportunity to work in his group and for all his scientific guidance and advice during this time. I would also like to thank Dr. Alexander Gerlach for his supervision and tireless support during my whole Ph.D. study and for all the scientific discussions, his motivation and his knowledge regarding the work in experimental physics. Additionally, I would also like to thank Dr. Alexander Hinderhofer for his scientific support. Both of them answered patiently every question I had in the last years. Furthermore, I thank Bernd Hofferberth and Ralf Zenke for providing technical support in our home laboratories, as well as Aleksandra Rötschke, Susanne Kern and Birgit Engler for their work regarding all organisational tasks in the group. I gratefully acknowledge the financial support by the German Research Foundation (Deutsche Forschungsgemeinschaft, DFG-GZ, HI 1927/1-1). I am very grateful to Dr. Jakub Hagara for providing me with his support in the evaluation of my GIWAXS data and for his collegiality as my office partner.

I thank also several synchrotrons for providing the facilities and the opportunity to perform my real-time experiments there. My gratitude goes to the European Synchrotron Radiation Facility (ESRF, France) for providing excellent facilities at ID10 and BM32 together with the beamline scientists Maciej Jankowski and Lucio Martinelli. Further gratitude goes to the Deutsches Elektronen Synchrotron (DESY, Germany) for providing excellent facilities at P03 and P23 with excellent support by the beamline scientists Pallavi Pandit and Dimitri Novikov. The experimental measurements at these facilities would not be possible without the support during the preparation and measurement period in particular from Dr. Martin Hodas, Dr. Alexander Gerlach, Nadine Russegger, Dr. Jakub Hagara, Anton Pylypenko, Dr. Ivan Zaluzhnyy and Dr. Valentina Belova.

Further acknowledgement goes to Prof. Dr. Monika Fleischer, Dr. Ronny Löffler and Eva Lohmann for providing me with the opportunity to conduct scanning electron microscopy (SEM) measurements with their equipment. I would also like to thank the bachelor students I worked together who performed and assisted with several measurements: Vivek Sehra, Damián Baláž, Maximilian Grimmer and Roody Nasro. I wish to express my thanks to Nadine Russegger, Dr. Jakub Hagara, Dr. Alexander Gerlach, Dr. Berthold Reisz, Ingrid Dax, Frederik Unger, Lena Merten and Dr. Ivan Zaluzhnyy for proofreading parts of this thesis and for their continuous support and encouragement in this group.

In the end, I want to thank my parents and all my friends for their patience and support during the last years that made all this work possible.